

Phase-switchable preparation of solution-processable WS₂ mono- or bilayers

Received: 22 March 2024

Accepted: 10 October 2024

Published online: 15 November 2024

 Check for updates

Liang Mei ^{1,13}, Zhan Gao^{2,13}, Ruijie Yang ^{1,13}, Zhen Zhang^{1,13}, Mingzi Sun ³, Xiongyi Liang ¹, Yuefeng Zhang¹, Ting Ying¹, Honglu Hu¹, Dengfeng Li ², Qinghua Zhang ⁴, M. Danny Gu ⁵ ✉, Lin Gu ⁶, Jiang Zhou ⁷, Bolong Huang ³, Damien Voiry ⁸, Xiao Cheng Zeng ¹, Yang Chai ⁹, Ju Li ¹⁰ ✉, Xinge Yu ^{2,11} ✉ & Zhiyuan Zeng ^{1,12} ✉

Crystal phase plays a crucial role in determining the properties of two-dimensional (2D) transition metal dichalcogenides. Here we achieve phase-switchable preparation of 2D transition metal dichalcogenides using an electrochemical lithium-ion intercalation-based exfoliation strategy by controlling the discharge current density and cutoff voltage. We discover that a small discharge current density (0.005 A g⁻¹, with a 0.9 V cutoff voltage) produces pure semiconducting 2H phase WS₂ bilayers. In contrast, a large discharge current density (0.02 A g⁻¹, with a 0.7 V cutoff voltage) leads to the dominant semimetallic 1T' phase WS₂ monolayers. The phase-switching mechanism was clarified through cryo-electron microscopy, annular dark-field scanning transmission electron microscopy, Raman, X-ray photoelectron spectroscopy, etc. The device (humidity sensor) application of produced 2D WS₂ was then demonstrated, showing phase-dependent humidity-sensing performances confirming the potential of our produced 2D WS₂ with switchable phase in device applications.

The crystal phase is a pivotal parameter when determining the properties and applications of two-dimensional (2D) transition metal dichalcogenides (TMDs)^{1–3}. Group-VI TMDs, such as MoS₂ and WS₂, can exist in diverse phases (2H, 1T or 1T'), depending on the coordination geometries of the transition metal atom (Supplementary Fig. 1). The 1T (octahedral coordination) and 1T' (distorted octahedral coordination) group-VI TMDs exhibit metallic and semimetallic properties, respectively, rendering them promising candidates for applications in energy storage^{4–6}, energy conversion^{7–10} and superconductivity¹¹. In contrast, the 2H (trigonal prismatic coordination) group-VI TMDs are typically semiconductors with a bandgap of 1–2 eV (ref. 12), making them exceptionally well suited for applications in nanoelectronics and optoelectronics^{13–15}.

The preparation of 2D group-VI TMDs (solution-processable TMDs in particular) with a designated phase tailored to intended applications is therefore important, as solution-processable 2D TMDs are compatible with solution-based deposition techniques (such as inkjet printing,

industrial roll-to-roll coating, drop-casting and spin-coating), facilitating the easy and scalable manufacture of customizable devices^{16,17}. Although such printable 2D group-VI TMD solutions could be prepared via direct liquid exfoliation in solvents¹⁸ and foreign species (for example, tetraalkylammonium ions^{19,20}, sulfate ions²¹ and small molecules²²) intercalation-based liquid exfoliation, the phase of the final 2D products is not adjustable, remaining the same phase as their initial bulk counterparts.

Previous studies suggest that 2H-to-1T/1T' phase transition occurs in group-VI TMDs during lithium-ion (Li⁺) intercalation-based exfoliation, resulting in 2D nanosheets (NSs) with a mixed phase of 2H and 1T/1T'^{9,23,24}. In theory, this is because the Li⁺ intercalation involves the electron injection from the *s* orbitals of guest lithium to the *d* orbitals of the host transition metal atoms to maintain overall charge neutrality²⁵. When the electron injection is beyond a certain threshold (in terms of MoS₂, this threshold is 0.29 electrons per formula unit¹⁹), the stability of the 2H phase group-VI TMDs will be lower than that of the 1T or

1T' phase, causing the corresponding phase transition. The occurrence of phase transition implies that Li⁺ intercalation-based exfoliation can theoretically become a plausible way for the preparation of solution-processable group-VI 2D TMDs with on-demand phases. Still, this has not yet been truly achieved experimentally, as the switch (on-off) for the phase transition is still unknown²⁴.

Here, we discover the electric switch of phase transition during the electrochemical Li⁺ intercalation-based exfoliation, achieving phase-switchable exfoliation of solution-processable WS₂ mono- or bilayers from their bulk counterparts (Supplementary Fig. 2). Specifically, we found that Li⁺ intercalation under a small discharge current density (0.005 A g⁻¹, with a 0.9 V cutoff voltage) will cause the formation of dense solid electrolyte interface (SEI) film at the edge of WS₂, which limits the insertion of Li⁺ below the phase transition threshold, resulting in semiconducting 2H-WS₂ bilayers. Conversely, a large discharge current density (0.02 A g⁻¹, with a 0.7 V cutoff voltage) will lead to 2H-to-1T/1T' phase transition and thereby produces semimetallic 1T'-WS₂ monolayers. In this case, no obvious SEI film is formed. Thus, Li⁺ can be fully intercalated in WS₂, resulting in a phase transition. Our findings give new vitality to the electrochemical Li⁺ intercalation-based exfoliation strategy, making it a feasible method for large-scale production of solution-processable group-VI 2D TMDs with designated phases.

Phase-switchable preparation and characterization

Figure 1a illustrates the overall phase-switchable preparation of 2H- and 1T'-WS₂ NSs using our electrochemical Li⁺ intercalation-based exfoliation strategy with controllable discharge current density and cutoff voltage (small current density: 0.005 A g⁻¹, 0.9 V; large current density: 0.02 A g⁻¹, 0.7 V), (see Methods for details). These parameters were determined through a serial of control experiments with different discharge current densities and cutoff voltages. Detailed results are presented in Supplementary Fig. 3, which shows that the threshold discharge current density required to initiate the formation of 2H-phase WS₂ NSs is 0.005 A g⁻¹. Raman (Fig. 1d and Supplementary Fig. 4) and X-ray photoelectron spectroscopy (XPS; Fig. 1e and Supplementary Fig. 5) analyses confirmed this conclusion.

The small current density-driven Li⁺ intercalation-based exfoliated WS₂ NS dispersion exhibits a light-green colour (Fig. 1b, inset and Supplementary Figs. 6 and 7), signifying partial absorption in the visible range, as verified via the ultraviolet–visible absorption spectrum (Fig. 1b), which confirm the formation of semiconducting 2H phase WS₂ NSs under a small discharging current density¹⁹. Conversely, the large current density exfoliated WS₂ NS dispersion shows a black colour (Fig. 1b, inset and Supplementary Figs. 6 and 7), indicating the complete and featureless absorption in the visible range (Fig. 1b), marking the emergence of phase transition and the formation of metallic 1T/1T' phase WS₂ NSs under a large discharging current density. Photoluminescence (PL), Raman spectroscopy and XPS further confirm the above phase analysis. Prominent PL appears in small current density exfoliated WS₂ NSs (Fig. 1c), signifying its semiconducting nature (2H phase). Only two dominant peaks (the in-plane phonon E_{12g}¹ at 350.3 cm⁻¹ and the out-of-plane phonon A_{1g} modes at 419.2 cm⁻¹, corresponding to 2H WS₂ (ref. 11)) appear in the Raman spectroscopy of small current density exfoliated WS₂ NSs (Fig. 1d), indicating their 2H phase. By contrast, the J₁, J₂ and J₃ peaks located at low-frequency regions are observed for

large current density exfoliated WS₂ NSs (Fig. 1d), indicative of the 1T' phase⁹. The yields of 2H-WS₂ (under small current density) and 1T'-WS₂ (under large current density) NSs are ~100% and ~67%, respectively, as confirmed by the deconvolution of the W 4f regions of exfoliated WS₂ in the XPS spectrum (Fig. 1e).

The phases of exfoliated WS₂ NSs are further confirmed by aberration-corrected annular dark-field scanning transmission electron microscopy (ADF-STEM). The ADF-STEM image of the small current density exfoliated WS₂ NSs shows a hexagonal lattice structure of individual W and S atoms (Fig. 1f), confirming the 2H phase²⁰, whereas the one-dimensional zigzag chains of W atoms dominate the entire image of the large current density exfoliated WS₂ NSs (Fig. 1g), indicative of the 1T' phase²⁶. Notably, a small area of 2H phase is also observed in the top-right corner of the image (Fig. 1g), suggesting the co-existence of 1T' and 2H phases in large current density exfoliated WS₂ NSs, and 1T' phase is dominant. Figure 1f,g in the bottom part show line intensity profiles scan along the white-boxed atoms. The intensity of S atoms is much more pronounced in 2H WS₂ owing to the enhanced signal resulting from the overlap of two S atoms along the direction of the electron beam²⁷. In contrast, for the 1T'-WS₂ structures, the intensity ratio of S atoms between the two W sites is much lower. This is attributed to the S atoms in the upper and lower layers being staggered, creating a triangular lattice.

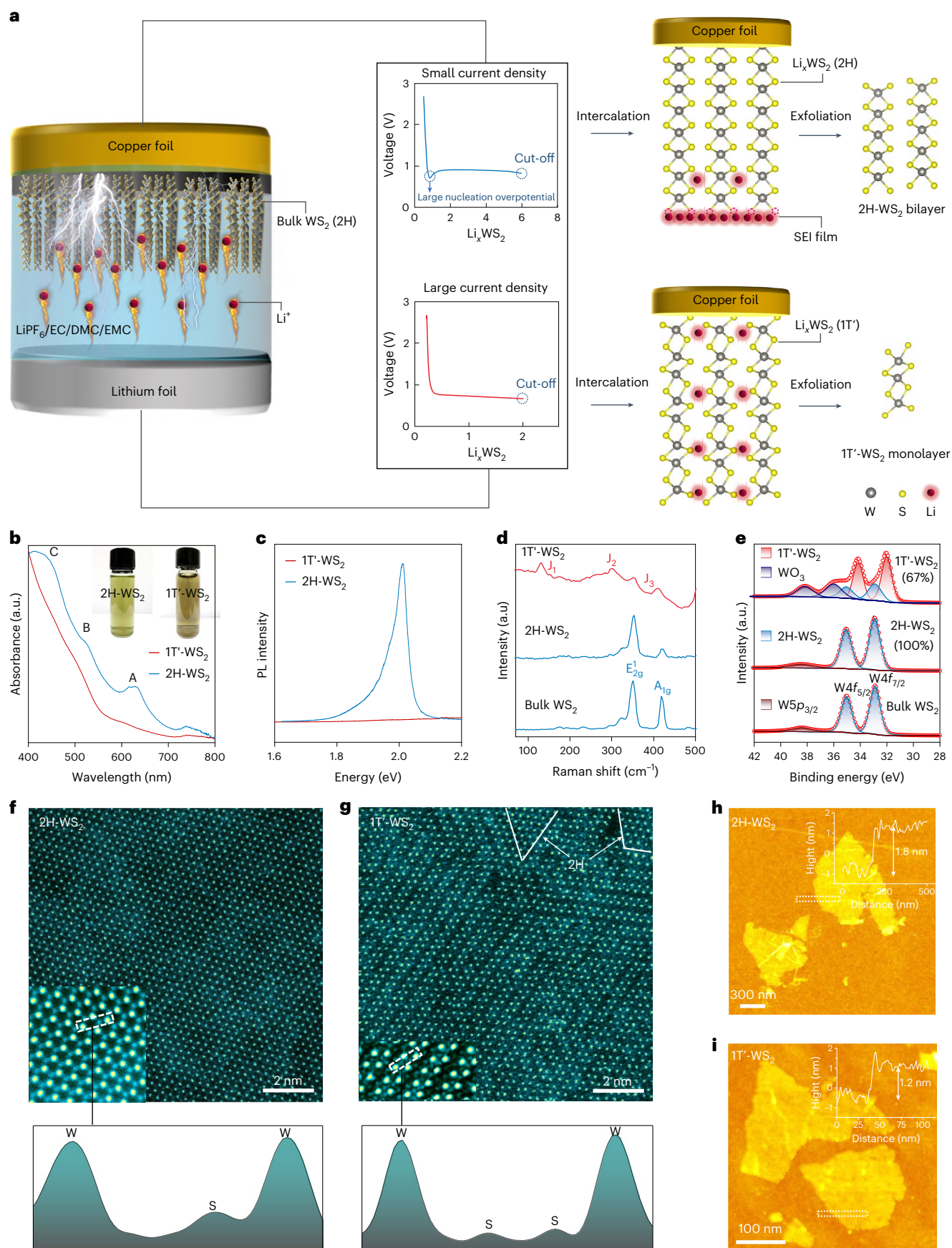
Sulfur vacancies are clearly observed in the ADF-STEM images of the prepared 2H- and 1T'-WS₂ NSs (Supplementary Figs. 8 and 9), and the electron paramagnetic resonance (EPR) results indicate that the sulfur vacancies in 2H-WS₂ NSs are more abundant than those in 1T'-WS₂ NSs (Supplementary Fig. 10). Transmission electron microscopy (TEM) reveals that the exfoliated 2H- and 1T'-WS₂ NSs have a lateral size ranging from 300 to 600 nm and 100 to 200 nm, respectively (Supplementary Fig. 11). Large quantities of 2H- and 1T'-WS₂ NSs were successfully prepared as confirmed by scanning electron microscope images (SEM; Supplementary Fig. 12). Atomic force microscopy (AFM) images show that the thickness of the 2H- and 1T'-WS₂ NSs is 1.8 nm and 1.2 nm (Fig. 1h,i; thickness distribution histograms are shown in Supplementary Fig. 13), respectively, indicating the formation of bilayer 2H- and monolayer 1T'-WS₂ NSs. Besides WS₂, phase-switchable preparation of WSe₂ was also successfully achieved and characterized (see detailed information in Supplementary Figs. 14–16). However, this method is not suitable for MoS₂; only 1T'-MoS₂ NSs can be prepared (Supplementary Figs. 17 and 18). This discrepancy might be due to the varying interaction energies between Li⁺ and different TMDs.

Phase-switching mechanism

To investigate the phase-switching mechanism, cryo-TEM is employed due to the sensitivity of lithium discharged samples to electron beams²⁸. When Li⁺ intercalation is driven by a small discharge current density, a dense compact and amorphous SEI film and Li₂S at the edge of WS₂ are observed (Fig. 2a–c). The ADF-STEM and electron energy loss spectroscopy (EELS) analyses (Fig. 2f and Supplementary Fig. 19) indicate that lithium predominantly localizes within the SEI. There is a minimal presence of Li⁺ intercalation occurring at the edge of WS₂ (ref. 29). This minimal Li⁺ edge intercalation is revealed by a small increase in interlayer spacing from 6.19 Å to 6.26 Å (Supplementary Fig. 20). The hexagonal symmetry structure (Fig. 2b), A–B–A stacking mode (Fig. 2d) and greenish colour (Fig. 2e) of the intercalated WS₂ confirm the 2H polytype.

Fig. 1 | Preparation and characterization of 2H- and 1T'-WS₂ NSs. **a**, A schematic of the phase-switchable synthesis of 2H- and 1T'-WS₂ NSs through a controllable electrochemical lithium intercalation-based exfoliation method. **b**, Visible–near-infrared absorption spectra of exfoliated 2H- and 1T'-WS₂ NS solution. A, B and C indicate the three absorption peaks in the spectrum of exfoliated 2H-WS₂. The insets show the photographs of exfoliated 2H- and 1T'-WS₂ NS solution. **c**, PL spectra of exfoliated 2H- and 1T'-WS₂. **d**, Raman spectra of bulk WS₂ and exfoliated 2H- and 1T'-WS₂. **e**, XPS W 4f spectra of bulk WS₂ and exfoliated 2H- and

1T'-WS₂. **f**, ADF-STEM image of 2H-WS₂. The enlarged atomic-resolution image is presented in the left corner. Line intensity profile scans along the white-boxed atoms in the enlarged image are shown below. **g**, An ADF-STEM image of 1T'-WS₂. The enlarged atomic-resolution image is presented in the left corner. Line intensity profile scans along the white-boxed atoms in the enlarged image are displayed below. A small area of 2H-WS₂ was found in the top right corner. **h**, **i**, AFM images of 2H- (**h**) and 1T'-WS₂ (**i**) NSs. The inset height profiles reveal the thickness of selected NSs.



In contrast, when a large discharge current density is applied, no significant SEI film is observed at the edge of WS₂, but exfoliated WS₂ appears (Fig. 2g–i). The ADF-STEM image and high-resolution EELS mapping confirm that Li⁺ indeed intercalates into the interior structure of WS₂ (Fig. 2l and Supplementary Fig. 21). The distorted A–B–C stacking mode (Fig. 2j) and the black colour (Fig. 2k) of the intercalated WS₂ reveals the 1T' phase. The XPS (Supplementary Figs. 22–24) and X-ray diffraction (Supplementary Fig. 20) characterizations further confirmed the 2H phase of small current density intercalated WS₂ and the 1T' phase of large current density intercalated WS₂.

Bringing together the findings from the analyses mentioned above, it becomes evident that a small discharge current density results in the creation of a dense SEI films at the edge of WS₂, which acts as a barrier preventing Li⁺ intercalation into the interlayer of WS₂ and thereby limits the electron injection (from the *s* orbitals of lithium to the *d* orbitals of the W atom) below the phase transition threshold (0.3 electrons per WS₂ formula unit, as confirmed by density functional theory (DFT) calculation; Supplementary Figs. 25–27 and Supplementary Table 1). This, in turn, results in the phase of the final product being consistent with the starting bulk materials (both being 2H phase) without a phase transition. Furthermore, the SEI caused irreversibility during the intercalation process, which is revealed through the charge–discharge curves (Supplementary Fig. 28) and corresponding EPR results (Supplementary Fig. 29). Conversely, a large discharge current density does not allow for the establishment of a well-defined SEI film; therefore, Li⁺ can be fully intercalated into the interlayer of WS₂. This process causes a charge density wave and a transition from the 2H phase to the 1T' phase, which, in turn, results in the dominance of 1T' phase in the final product.

To explain how the discharge current density influences SEI formation and ultimately affects WS₂ phase transition, we conducted theoretical simulations. The large and small discharge current densities were simulated as the high and low concentrations of Li⁺ near WS₂. We also introduced different external electric fields along the WS₂ layers as the reaction potentials. It is observed that, under different potential conditions, smaller potentials promote the Li⁺ diffusions into the WS₂ interlayers (Supplementary Fig. 30a,b). This proves that a higher discharge current density with lower reaction potential benefits the thorough diffusions of Li⁺ into the WS₂ interlayers. For the smaller discharge current density with lower Li⁺ concentration, the single Li⁺ diffusion into the WS₂ interlayer is challenging due to the increasing energy barriers, indicating that the lower-concentration Li⁺ are prone to be limited near the edge of WS₂ (Supplementary Fig. 30c).

During the molecular dynamics (MD) simulations of high-concentration Li⁺, the intercalation of Li⁺ into the WS₂ layers is clearly observed, which results in the exfoliations of WS₂ layers (Supplementary Fig. 30d–f). In addition, the WS₂ layers experience the formation of superstructure rather than the amorphizations, which initiates the phase change to 1T' structures under the high discharge current density. In contrast, when the WS₂ layers are interacting with a small concentration of Li⁺ under a low discharge current density, we notice that the strong interactions with the WS₂ layer are limited only near the edge by strong adsorptions, which induces the evident amorphization of WS₂ towards the SEI formation (Supplementary Fig. 30g–i).

In addition, the interlayer spaces are blocked by Li–S bonding and the amorphous structures, which further hinder the diffusions of the Li⁺ into the WS₂ interlayers and maintain the original 1H structures. These observations are supportive of experimental results and confirm that the diffusion behaviours of Li⁺ are strongly related to the discharge condition, supplying important insights into the understanding of SEI formation and WS₂ phase change.

Device applications

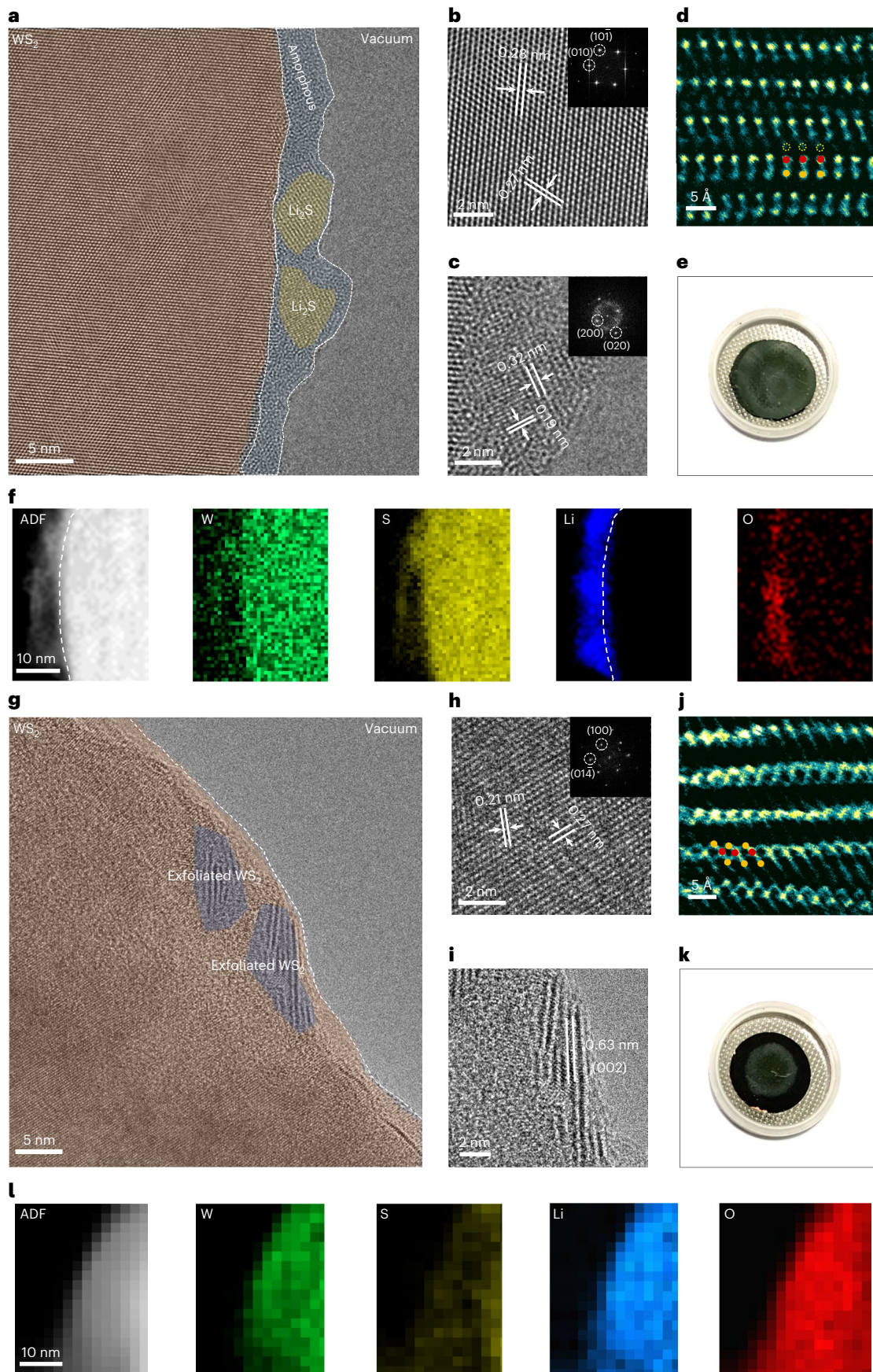
Since the prepared 1T'-WS₂ monolayers and 2H-WS₂ bilayers possess high surface areas and exposed sulfur atoms, they are ideal platforms for humidity sensors. In addition, different phases of WS₂ interact with H₂O molecules in distinct ways. The solution-prepared 2H- and 1T'-WS₂ NSs are therefore examined for humidity sensor applications. Drop-casting is used to deposit the WS₂ NSs onto a polyethylene terephthalate (PET) substrate. After drying, Au electrodes are sputtered onto WS₂ NSs for wiring purposes (Fig. 3a and Supplementary Fig. 31). The basic humidity-sensing properties are investigated using a home-made humidity sensor test system (Supplementary Fig. 32).

The significant variations in device current under different relative humidity (RH) conditions indicate a wide humidity response range of our fabricated 2H-WS₂ humidity sensor (Fig. 3b,c). As the RH varies from 15% to 90%, the current of the devices at a bias of 10 V increases by nearly two orders of magnitude, suggesting excellent humidity-sensing capabilities of our device. Notably, the 2H-WS₂ humidity sensor exhibits a stronger response when the applied RH exceeds 65%, signifying that such a humidity sensor is well suited for applications requiring detection in high-humidity environments, such as breath rate monitoring and non-touch positioning interfaces. This behaviour can be explained by the presence of two distinct conduction mechanisms corresponding to different humidity ranges (refer to Supplementary Figs. 33 and 34)³⁰. The dynamic humidity response and recovery measurements of the WS₂ humidity sensors are shown in Fig. 3d, demonstrating excellent selectivity and repeatability when responding to different levels of RH. Response and recovery times are crucial parameters that determine the sensitivity of humidity sensors. Figure 3e shows the repeatable dynamic humidity response of the 2H-WS₂ humidity sensors from RH 60% to RH 75%, demonstrating ultrafast response and recovery times below 1 s. An enlarged *I*–*T* (*I*, current; *T*, time) curve (Fig. 3f) reveals that the response and recovery times for 2H-WS₂ humidity sensor are 0.48 s and 0.32 s, respectively. In comparison, these values are 0.30 s and 1.20 s for the 1T'-WS₂ humidity sensor tested under the same conditions (Fig. 3g,h). Compared with the 2H-WS₂ humidity sensor, the 1T'-WS₂ humidity sensor exhibits a faster response but a slower recovery time. This difference can be attributed to the fact that 1T'-WS₂ has more negative adsorption energy towards water molecules than 2H-WS₂ (Supplementary Figs. 35 and 36, –0.73 eV versus –0.18 eV), implying that water molecules are more easily adsorbed on 1T'-WS₂. Conversely, water molecules are more challenging to desorb from the surface of 1T'-WS₂, resulting in a longer recovery time.

When comparing the response and recovery times with other reported humidity sensors, both our fabricated 2H- and 1T'-WS₂ sensors demonstrate the fastest recovery and response times (Fig. 3i and

Fig. 2 | Characterization of intercalated WS₂. **a**, A cryo-TEM image of a small current density intercalated WS₂ electrode, showing the amorphous SEI and Li₂S on the surface of WS₂. **b,c**, High-resolution (HR)TEM images of WS₂ (**b**) and Li₂S (**c**) shown in **a**. The insets in **b** and **c** are the corresponding diffraction patterns. The lattice distances of 0.28 and 0.27 nm are attributed to the (010) and (101) planes of WS₂ (**b**). For Li₂S (**c**), the lattice distances of 0.32 and 0.19 nm correspond to the (200) and (020) planes, respectively. **d**, A cross-sectional ADF-STEM image of small current density intercalated WS₂. The red and yellow circles denote the W and S atoms, respectively. **e**, An optical image of small current density intercalated WS₂ electrodes after the discharging process. **f**, An ADF-STEM image and EELS elemental mapping of small current density intercalated WS₂.

g, A cryo-TEM image of a large current density intercalated electrode showing exfoliated WS₂ on the surface. **h,i**, HRTEM images of WS₂ (**h**) and surface exfoliated WS₂ (**i**) shown in **g**. The insets in **h** and **i** are the corresponding diffraction patterns. The lattice distances of 0.27 and 0.21 nm are attributed to the (100) and (014) planes of WS₂ (**h**). The lattice distance of 0.63 nm corresponds to the (002) plane of WS₂ (**i**). **j**, A cross-sectional ADF-STEM image of large current density intercalated WS₂. The red and yellow circles denote the W and S atoms. **k**, An optical image of large current density intercalated WS₂ electrodes after the discharging process. **l**, An ADF-STEM image and EELS elemental mapping of large current density intercalated WS₂.



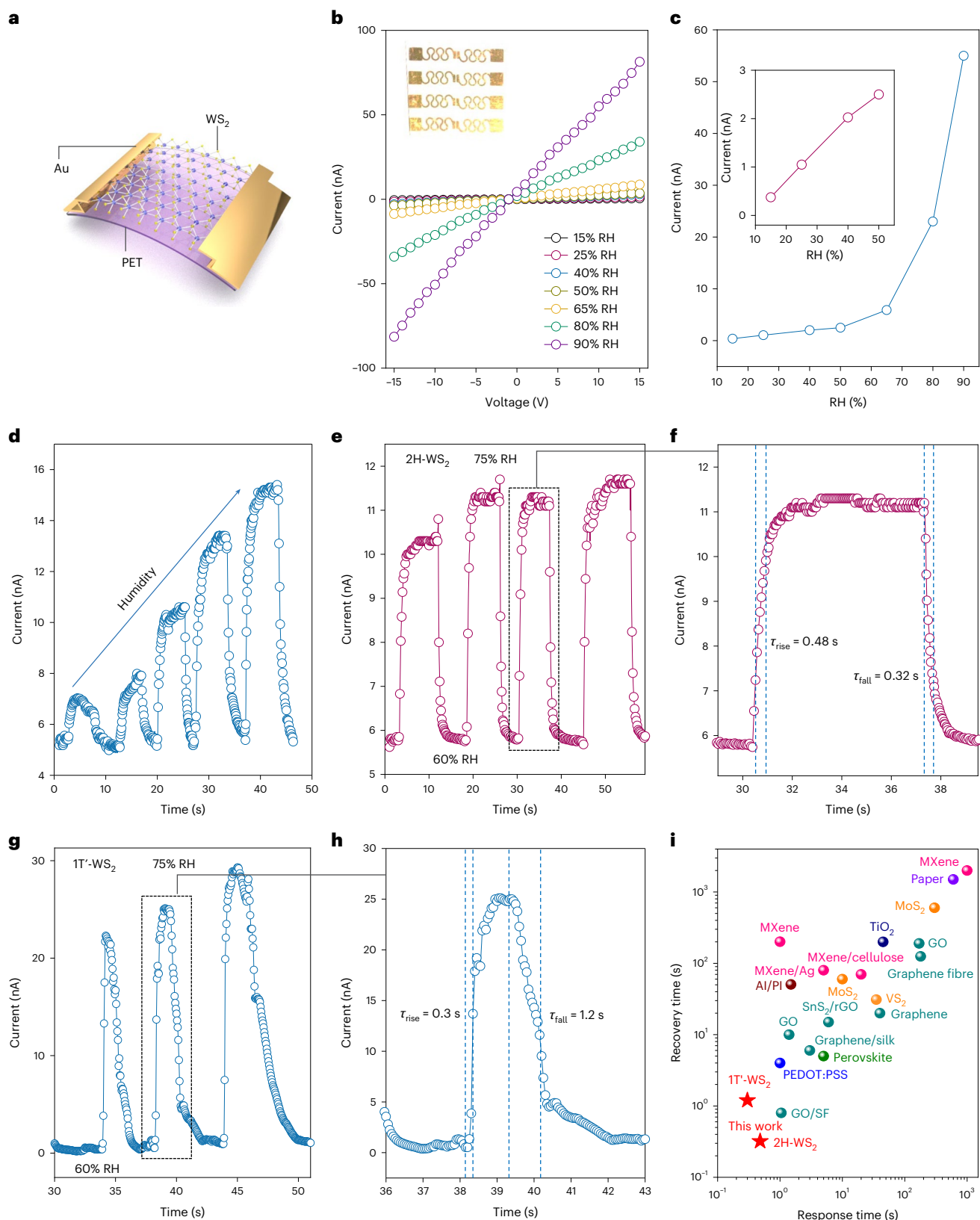


Fig. 3 | Humidity-sensing performance. **a**, A schematic illustration of the WS₂-based humidity sensor. **b**, *I*-*V* measurement of 2H-WS₂ humidity sensor under different levels of RH. *I*, current; *V*, voltage. **c**, *I*-RH curves. The inset is the enlarged curve of low RH levels between 15% and 50%. **d**, The dynamic humidity response and recovery measurement under different levels of RH. **e**, The response and recovery curve of 2H-WS₂ from 60% RH to 75% RH. **f**, The amplified response and recovery curve from **e**. τ_{rise} and τ_{fall} represent response

and recover times. **g**, The response and recovery curve of 1T'-WS₂ from 60% RH to 75% RH. **h**, The amplified response and recovery curve from **g**. **i**, A comparison of the humidity-sensing performance of fabricated 2H- and 1T'-WS₂ NSs with other reported humidity sensors in literatures. MXene represents transition metal carbides, nitrides and carbonitrides. GO/SF denotes graphene oxide and silk fibroin, and PEDOT refers to poly(3,4-ethylenedioxythiophene) polystyrene sulfonate. The details can be found in Supplementary Table 2.

Supplementary Table 2). The origin of short recovery and response time in Fig. 3i is due to the ultrathin structure of the exfoliated WS₂ NSs and the presence of abundant S defects. Specifically, the prepared 1T'-WS₂ and 2H-WS₂ NSs, being monolayer and bilayer, respectively, are significantly thinner than other humidity sensor materials, as shown in Fig. 3i. The prepared 1T'-WS₂ and 2H-WS₂ materials possess an exceptionally high surface-to-volume ratio, which results in a greater number of atoms being exposed on the surface, enhancing the interaction with water molecules. This high surface area facilitates increased adsorption of water molecules, leading to substantially increased changes in electrical properties (Supplementary Fig. 33) and, consequently, higher sensitivity to humidity variations³¹. Hence, the minimal thickness of these 2D materials enables rapid adsorption and desorption of water molecules, contributing to faster response and recovery times. Furthermore, the prepared 1T'-WS₂ and 2H-WS₂ NSs possess abundant sulfur defects (as confirmed by the EPR spectra in Supplementary Fig. 10), which enhance conductivity (as confirmed by DFT calculations in Supplementary Fig. 37)³² and subsequently shorten the response time and improve the recovery speed. These factors sufficiently explain the short response and recovery times observed in our prepared 1T'-WS₂ and 2H-WS₂ NSs, as illustrated in Fig. 3i. Based on the relatively faster response and recovery speed, 2H-WS₂ NSs were selected for the following humidity-sensing demonstration.

The mechanical properties of the 2H-WS₂ humidity sensor are examined by analysing its response current under RH 65% after subjecting it to different cycles of bending. The WS₂ humidity sensor demonstrates exceptional flexibility, with the response current remaining nearly unchanged even after 1,300 cycles of bending (Fig. 4a). This resilience can be attributed to the use of exfoliated WS₂ NSs, which are intrinsically flexible ultrathin 2D materials with a high fracture strain of approximately 25–30% (refs. 33–35). These properties significantly contribute to the stability of the fabricated devices. Leveraging the highly sensitive and ultrafast response and recovery properties, we demonstrate the application of our WS₂ humidity sensor for breath monitoring, a critical aspect of diagnosing and treating slowly progressing diseases with few early indicators (for example cancer, diabetes and sleep apnoea–hypopnoea syndrome)³⁶. The WS₂ humidity sensor is easily attached under the human nose to demonstrate nasal breath monitoring. As shown in Fig. 4b, the device's current value simultaneously varies in response to changes in breath rate. During the 3–7 s of measurement, the tested subject took a deep breath and exhaled a high RH level flow, resulting in a significant rise and fall in current. Subsequently, the subject breathes at a quick and uneven rate within 8 s, leading to low-amplitude and high-frequency fluctuations in the device's current. These results demonstrate that the ultrafast response and recovery properties of the WS₂ humidity sensor can effectively support precise real-time breath monitoring. In addition, the WS₂ humidity sensor can be employed to test the protective performance of various types of mask (Supplementary Fig. 38), which holds significant importance, such as during the coronavirus disease 2019 epidemic.

A prototype speech recognition device has also been developed. When a person speaks, the pronunciation of different words leads to variations in the concentration of exhaled water vapour. As shown in Supplementary Fig. 39, the ultrafast response and recovery of the WS₂-based humidity sensor allow it to detect real-time changes in breath humidity associated with spoken words. Consequently, this generates characteristic current curves corresponding to each word. Supplementary Figs. 40–43 shows the characteristic current curves recorded by the device for various spoken words, including 'Hi', 'people', 'thank you', 'you are welcome', 'question', 'unbelievable' and 'beautiful'. These current response curves exhibit unique and distinct characteristic peaks with high repeatability, highlighting the device's significant potential for voice recognition applications.

The long-range manipulation of devices offers promising potential for future electronics, particularly in applications like non-touch switches and touchless localization interfaces. Moisture detection can serve as a compelling stimulus signal to enable these innovative applications^{37–39}. The high sensitivity and rapid responsiveness of the fabricated WS₂ humidity sensor are more than capable of meeting the requirements for real-time touchless localization interfaces. As illustrated in Fig. 4c (inset), the human finger serves as the moisture source. Quantitative measurements under a bias of 10 V in Fig. 4c demonstrate an exponential relationship between finger distance and the response current of a single WS₂ humidity sensor. The sensor begins to show a slight response at a vertical height of 6 mm that gradually increases as the finger approaches. Figure 4d reveals the dynamic current of the device in response to an approaching finger in an indoor environment. Benefitting from the ultrafast response and recovery time, the device's current increases as the finger approaches without any hysteresis. Furthermore, the superior stability of the WS₂ humidity sensor is confirmed by exposing it to the indoor environment (65% RH, room temperature) for 96 h (Supplementary Fig. 44).

Prompted by the excellent response capabilities, a touchless localization interface can be realized using the WS₂ humidity sensor array. Figure 4e shows a 5 × 5 WS₂ humidity sensor array on a PET substrate. The as-fabricated touchless localization interface retains its flexibility as demonstrated in Supplementary Fig. 45. Even under bending conditions, the response and recovery properties remain nearly unchanged compared with the flat condition. The successful distinction of the relative position and depth of two fingers using the WS₂-based localization interface is showcased in Fig. 4e,f. To enhance the image quality, we use the interpolation function in origin software to obtain a higher-density and clearer current distribution map (the original array density is 5 × 5, and the initial current distribution of the array is summarized in Supplementary Fig. 46). The current distribution map in Fig. 4f reveals the location of the two fingers, with colours indicating the vertical distance between the fingers and the sensor array. By incorporating the information of the location and depth of the fingers in a three-dimensional (3D) cuboid, a reconstructed 3D model that closely resembles the actual positions of the two fingers can be achieved (Fig. 4f). These results suggest that the WS₂-based localization interface can be employed to reconstruct the spatial distribution of subjects on the basis of moisture stimulus signals. Furthermore, due to its fast response and recovery properties, real-time location monitoring can be realized using our touchless localization interface. As shown in Fig. 4g,h, the contour map of the current distribution can reveal the areas covered by fingers as a single finger sweeps past our touchless localization interface at a very low height. To highlight the reconfigurability and advantages of the humidity sensor array, we showcase its potential application in monitoring baby diaper wetness. The detailed results and analysis are shown in Supplementary Fig. 47.

Conclusions

This study demonstrates the successful realization of a phase-switchable synthesis for solution-processable 2H- and 1T'-WS₂ NSs. An electrochemical Li⁺ intercalation-based exfoliation strategy with precise control over Li⁺ intercalation electrochemistry was developed. We found that a small discharge current density results in the production of pure semiconducting 2H phase WS₂ bilayers, while a large discharge current density leads to the prevalence of semimetallic 1T' phase WS₂ monolayers. The phase-switching mechanism is clarified through cryo-electron microscopy, ADF-STEM, Raman, XPS, etc. The device application potential of the produced solution-processable 2D WS₂ is demonstrated. Together, our work presents a phase engineering method for the exfoliation of solution-processable 2D TMDs with implications in future electronics.

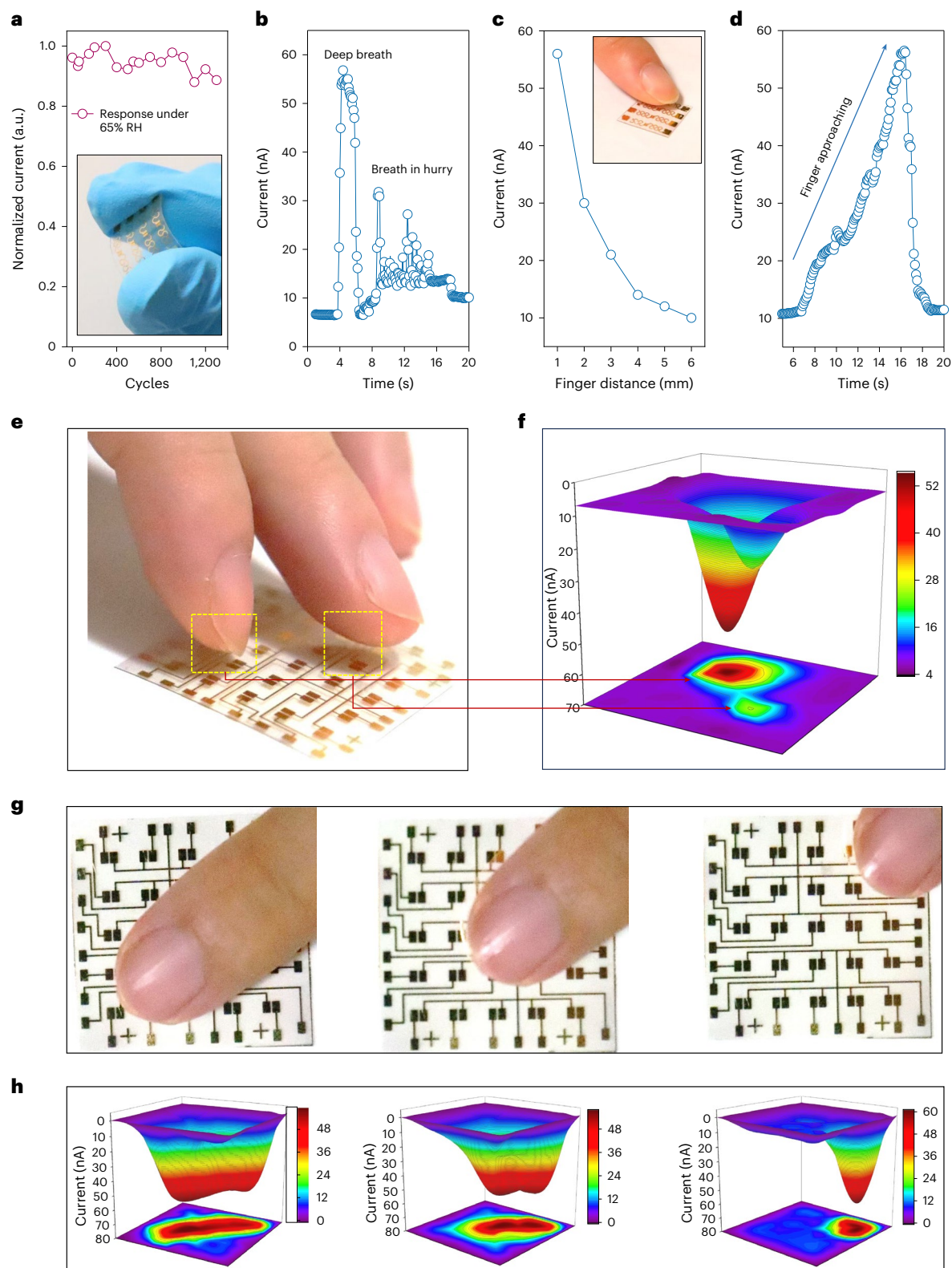


Fig. 4 | Sensor array for touchless localization interfaces. **a**, Mechanical property measurement of the WS₂ humidity sensor. The inset shows the flexibility of the device. **b**, Nasal breath monitoring curve. **c**, Quantitative measurement between finger distance and device current under a bias of 10 V. The inset shows the finger approaching the device. **d**, The dynamic current curve of the WS₂ humidity sensor as the finger approaches. **e**, An optical image

of the relative localization of two approaching fingers above the 5 × 5 arrays. **f**, The corresponding 3D mapping of the approaching of two fingertips. **g**, Optical images of the finger sweeping above the touchless localization interfaces based on the WS₂ humidity sensor array. The corresponding 3D mapping of current distribution is shown in **h**.

Methods

Chemicals

Tungsten disulfide (WS_2 , 99.9%, Macklin), carbon black (Bay Carbon), polyvinylidene difluoride (Sigma-Aldrich), 1-methyl-2-pyrrolidinone (99%, J&K Scientific), copper foil (Shenzhen Kejing Star Technology Company), lithium foil (DoDoChem), polypropylene film (Celgard 2300), Li^+ battery electrolyte (1.0 M $LiPF_6$ in ethylene carbonate (EC):dimethyl carbonate (DMC):ethyl methyl carbonate (EMC) = 1:1:1 vol%, DoDoChem), 3-aminopropyltriethoxysilane (99%, Aladdin), acetone (American Chemical Society grade, Anaqua Global International), ethanol (American Chemical Society reagent, $\geq 99.5\%$, Macklin). The deionized water was purified using Milli-Q System (Millipore).

Synthesis of 2H- and 1T'- WS_2 NSs

The 2H- and 1T'- WS_2 NSs were synthesized through a precise electrochemical Li^+ intercalation-based exfoliation process. This method was carried out within a coin cell setup, utilizing a copper foil-coated bulk WS_2 cathode (weighing 5 mg), lithium foil as the anode and an electrolyte solution comprising lithium hexafluorophosphate ($LiPF_6$) dissolved in a mixture of EC, DMC and EMC in a 1:1:1 volume ratio. A galvanostatic discharge was applied to initiate the Li^+ intercalation of the bulk WS_2 . Upon completion of the intercalation process, the resulting lithium-intercalated WS_2 (Li_xWS_2) was carefully extracted from the coin cell and subjected to sonication in appropriate solvents to achieve exfoliation. The key differences in the synthesis of 2H- and 1T'- WS_2 NSs are associated with the specific discharge current density and cutoff voltage settings during the galvanostatic discharge. For the production of 2H- WS_2 NSs, these critical parameters were established at 0.005 A g^{-1} and 0.9 V, whereas for 1T'- WS_2 NSs, the parameters were fine-tuned to 0.02 A g^{-1} and 0.7 V (the galvanostatic discharge curves are shown in Supplementary Fig. 3). In addition, 2H- WS_2 NSs were prepared by sonication in ethanol, whereas 1T'- WS_2 NSs were fabricated through sonication in deionized water. Following the sonication step, both the 2H- and 1T'- WS_2 suspensions underwent centrifugation and multiple washing steps before being ultimately redispersed in a solvent for further characterization and device fabrication.

Characterizations

The following instruments were used in our experiments: ADF-STEM (JEOL ARM200F spherical aberration-corrected transmission electron microscope operated at 200 kV), TEM (FEI talosf200s), cryo-TEM (Titan Krios G3i, operating at 300 kV and equipped with a Ceta-D camera, Falcon 3 direct electron detector, and Gatan K3 direct electron detector camera), SEM (JSM-7600), XPS (Thermo Scientific K-Alpha Nexsa), AFM (Dimension 3100), Raman spectroscopy (WITec alpha 300 confocal Raman microscope, 532 nm), X-ray diffraction (D2 PHASER XE-T, Cu $K\alpha$ radiation source, 30 kV voltage and 10 mA current), ultraviolet-visible spectrophotometry (UH 4150 UV, Hitachi), EPR (Bruker A300) and zeta potential analysis (Malvern Zetasizer Nano series). Lithiated WS_2 (small discharge current density Li^+ -intercalated WS_2 (S- Li_xWS_2), large discharge current density Li^+ -intercalated WS_2 (L- Li_xWS_2)) were injected via glove box to prevent oxidation.

Fabrication of WS_2 -based device

The PET substrate ($1.5 \times 1.5\text{ cm}^2$) underwent a thorough cleaning process in an ultrasonic bath. It was sequentially cleaned with detergent water, acetone, deionized water and isopropyl alcohol, with each cleaning step lasting for 15 min. After this cleaning procedure, an ethanol dispersion of exfoliated WS_2 NSs (32 mg l^{-1}) was drop-cast onto the PET substrate and allowed to dry at room temperature. Finally, 200-nm-thick Au electrodes were sputtered onto the PET substrate using a QUORUM #Q150TS Dual target sputtering system, employing a designed metal mask.

In the fabrication of the WS_2 -based sensor array, the PET substrates underwent the previously described cleaning process. Following this,

a circuit design based on Au was meticulously created using the QUORUM #Q150TS Dual target sputtering system, with the aid of a precisely designed metal mask. Subsequently, a custom metal mask with a rectangular array pattern was accurately affixed onto the as-fabricated circuit. This attachment was made using specific counterpoints to ensure accuracy. An ethanol dispersion of WS_2 NSs (32 mg l^{-1}) was then drop-cast onto the substrate. Afterwards, the mask was carefully removed once the solution had completely dried, leaving the WS_2 NSs in the desired pattern on the substrate.

Humidity-sensing tests

The humidity-sensing performance was evaluated within a custom-made sealed container, as depicted in Supplementary Fig. 32. Various humidity levels were precisely controlled by adjusting the mass flow of dry and moistened argon gas that was introduced into the container. The chip carrier was connected to external measurement equipment (Keysight B1500A Semiconductor Analyze) for conducting the tests. For the breathing test, a humidity sensor was placed under the nose or on masks to monitor exhaled gas humidity at different breathing rates. In the humidity sensing of the finger approach experiment, the sensor was positioned horizontally, and a finger was gradually brought closer from above. For touchless localization, the finger was held at a fixed height above the sensor array, and the current of each sensor was measured. In the voice recognition test, the sensor was placed 5 cm in front of the subject's mouth, and current changes were recorded as they pronounced English words with different lengths. All sensor currents were recorded in real time using a Keysight B1500A Semiconductor Analyzer.

Cryo-transfer procedure and sample preparation

In ambient air at room temperature, the highly reactive SEI components present on the surface of WS_2 can be susceptible to damage and crystalline amorphization when subjected to electron beam irradiation under TEM mode. To overcome these challenges, we employed super-low-dose and cryogenic-TEM techniques. Following the completion of the discharge process, the coin cells were carefully disassembled within an argon-filled glovebox (with H_2O and O_2 levels maintained below 0.01 ppm). The lithiated WS_2 electrodes, discharged at different current densities, were briefly rinsed with dimethyl carbonate for 30 s to eliminate excess lithium salts from their surfaces. Subsequently, the electrodes were allowed to dry inside the glovebox. After drying, the electrodes were gently scraped into a powder form using a blade and then dispersed onto a copper TEM grid. This copper grid was securely placed within a four-hole sample holder, sealed tightly and then immersed directly into a liquid nitrogen bath to prevent any contact with oxygen and moisture. The sealed cryo-electron microscopy sample holder was transferred to the cryo-electron microscopy auto-sampler system using liquid nitrogen. All data in this study were acquired using the low-dose cryo-electron microscopy platform. Throughout the entire experimental process, the sample temperature was meticulously maintained at 80 K. The high-resolution TEM images had a resolution of $4,096 \times 4,096$ pixels, with exposure times varying from 10 to 20 s and an electron dose rate of $10\text{--}15\text{ e} \text{ \AA}^{-2} \text{ s}^{-1}$. Cryo-STEM EELS mapping data were collected using the Gatan K3 direct electron detector camera with a probe current of 50 pA.

Theoretical calculations

To investigate the interactions between WS_2 and Li^+ ions under different discharge current density conditions, we applied the Forcite package to perform MD simulations and to compute diffusion barriers of Li^+ ions. Three layers of 2H- WS_2 were constructed in an 8×8 supercell. Forty-eight Li^+ ions with random distributions were introduced near the WS_2 structure as the high discharge current density conditions. In comparison, we reduced the number of Li^+ ions to 12 as the low discharge current density. Meanwhile, the external electric field was also introduced

along the y axis to align with the WS_2 layers. The MD simulations were under NVT mode at 298 K for 1 ns with 1 fs step size, and the Anderson strategy was used to control the temperature during MD simulations.

The calculations for H_2O adsorption energy and partial density of states in WS_2 were conducted using spin-polarized within the Vienna Ab-initio Simulation Package code⁴⁰. The Perdew–Burke–Ernzerhof version of the generalized gradient approximation⁴¹ was employed to describe the exchange–correlation density functional. The cutoff energy for the plane-wave basis was set to 420 eV, and k -point meshes were generated according to the Monkhorst–Pack scheme. The projected augmented wave potentials were utilized to solve the electronic structure self-consistently using a k -point mesh of $8 \times 8 \times 1$ and $3 \times 3 \times 1$ for unit cell and supercell of size $3 \times 3 \times 1$, respectively. The electronic relaxation was performed within an energy tolerance of 10^{-6} eV for self-consistency, while ionic optimizations continued until all the residual forces were smaller than $0.02 \text{ eV } \text{\AA}^{-1}$. $W d^4 s^2$ and $S s^2 p^4$ electrons were treated as valence electrons. A vacuum region of 15 \AA was set to avoid the interaction along the z direction between adjacent images.

For calculations of phase formation energy for different intercalated Li amounts in Li_xWS_2 , the ion–electron interaction was described using the projector augmented-wave method with a kinetic energy cutoff of 600 eV. Van der Waals interactions were considered using Grimme's DFT-D3 method⁴². Tighter convergence criteria (10^{-8} eV for energy and $10^{-5} \text{ eV } \text{\AA}^{-1}$ for force) and a denser Monkhorst–Pack grid ($8 \times 8 \times 8$) were applied for unit cell geometric optimization. To investigate interactions between WS_2 and Li atoms, the calculations were conducted until the total energy and force values reached less than 10^{-5} eV per atom and $0.02 \text{ eV } \text{\AA}^{-1}$, respectively. For sampling the Brillouin zone, a Monkhorst–Pack k -point grid of $5 \times 5 \times 5$ was used. To evaluate the thermal stability of Li-intercalated WS_2 , the formation energy (ΔH_f) was calculated and can be expressed by $\Delta H_f = E_{\text{total}} - \sum_i \mu_i x_i$, where ΔE_{total} represents the DFT total energy of the compound, μ_i is the chemical potential of element i and x_i is the quantity of element i in the compound.

Data availability

The data that support the findings of this study are available within the article and its Supplementary Information. Source data are provided with this paper.

References

1. Yang, R. J. et al. Intercalation in 2D materials and in situ studies. *Nat. Rev. Chem.* **8**, 410–432 (2024).
2. Mei, L. et al. Metallic 1T'/1T' phase TMD nanosheets with enhanced chemisorption sites for ultrahigh-efficiency lead removal. *Nat. Commun.* **15**, 7770 (2024).
3. Chhowalla, M. et al. The chemistry of two-dimensional layered transition metal dichalcogenide nanosheets. *Nat. Chem.* **5**, 263–275 (2013).
4. Li, Z. N. et al. Lithiated metallic molybdenum disulfide nanosheets for high-performance lithium-sulfur batteries. *Nat. Energy* **8**, 84–93 (2023).
5. Chen, W. S. et al. Two-dimensional quantum-sheet films with sub-1.2 nm channels for ultrahigh-rate electrochemical capacitance. *Nat. Nanotechnol.* **17**, 153–158 (2022).
6. Acerce, M. et al. Metallic 1T phase MoS_2 nanosheets as supercapacitor electrode materials. *Nat. Nanotechnol.* **10**, 313–318 (2015).
7. Yu, Y. F. et al. High phase-purity 1T'- MoS_2 - and 1T'- MoSe_2 -layered crystals. *Nat. Chem.* **10**, 638–643 (2018).
8. Voiry, D. et al. Conducting MoS_2 nanosheets as catalysts for hydrogen evolution reaction. *Nano Lett.* **13**, 6222–6227 (2013).
9. Voiry, D. et al. Enhanced catalytic activity in strained chemically exfoliated WS_2 nanosheets for hydrogen evolution. *Nat. Mater.* **12**, 850–855 (2013).
10. Shi, Z. Y. et al. Phase-dependent growth of Pt on MoS_2 for highly efficient H_2 evolution. *Nature* **621**, 300–305 (2023).
11. Lai, Z. C. et al. Metastable 1T'-phase group VIB transition metal dichalcogenide crystals. *Nat. Mater.* **20**, 1113–1120 (2021).
12. Yang, R. J. et al. 2D transition metal dichalcogenides for photocatalysis. *Angew. Chem. Int. Ed.* **62**, e202218016 (2023).
13. Wang, Q. H. et al. Electronics and optoelectronics of two-dimensional transition metal dichalcogenides. *Nat. Nanotechnol.* **7**, 699–712 (2012).
14. Sebastian, A. et al. Benchmarking monolayer MoS_2 and WS_2 field-effect transistors. *Nat. Commun.* **12**, 693 (2021).
15. Radisavljevic, B. et al. Single-layer MoS_2 transistors. *Nat. Nanotechnol.* **6**, 147–150 (2011).
16. Yang, R. et al. Synthesis of atomically thin sheets by the intercalation-based exfoliation of layered materials. *Nat. Synth.* **2**, 101–118 (2023).
17. Pinilla, S. et al. Two-dimensional material inks. *Nat. Rev. Mater.* **7**, 717–735 (2022).
18. Coleman, J. N. et al. Two-dimensional nanosheets produced by liquid exfoliation of layered materials. *Science* **331**, 568–571 (2011).
19. Lin, Z. Y. et al. Solution-processable 2D semiconductors for high-performance large-area electronics. *Nature* **562**, 254–258 (2018).
20. Li, J. et al. Printable two-dimensional superconducting monolayers. *Nat. Mater.* **20**, 181–187 (2021).
21. Liu, N. et al. Large-area atomically thin MoS_2 nanosheets prepared using electrochemical exfoliation. *ACS Nano* **8**, 6902–6910 (2014).
22. Jeong, S. et al. Tandem intercalation strategy for single-layer nanosheets as an effective alternative to conventional exfoliation processes. *Nat. Commun.* **6**, 5763 (2015).
23. Eda, G. et al. Photoluminescence from chemically exfoliated MoS_2 . *Nano Lett.* **11**, 5111–5116 (2011).
24. Yang, R. J. et al. High-yield production of mono- or few-layer transition metal dichalcogenide nanosheets by an electrochemical lithium ion intercalation-based exfoliation method. *Nat. Protoc.* **17**, 358–377 (2022).
25. Li, W. et al. Phase transitions in 2D materials. *Nat. Rev. Mater.* **6**, 829–846 (2021).
26. Song, X. Y. et al. Synthesis of an aqueous, air-stable, superconducting 1T'- WS_2 monolayer ink. *Sci. Adv.* **9**, eadd616 (2023).
27. Chou, S. S. et al. Understanding catalysis in a multiphase two-dimensional transition metal dichalcogenide. *Nat. Commun.* **6**, 8311 (2015).
28. Wang, X. F. et al. Cryogenic electron microscopy for characterizing and diagnosing batteries. *Joule* **2**, 2225–2234 (2018).
29. Fan, X. B. et al. Controlled exfoliation of MoS_2 crystals into trilayer nanosheets. *J. Am. Chem. Soc.* **138**, 5143–5149 (2016).
30. Guo, P. et al. An all-printed, fast-response flexible humidity sensor based on Hexagonal- WO_3 nanowires for multifunctional applications. *Adv. Mater.* **35**, 2304420 (2023).
31. Anchini, C. et al. Chemical sensing with 2D materials. *Chem. Soc. Rev.* **47**, 4860–4908 (2018).
32. He, H. N. et al. Anion vacancies regulating endows MoSSe with fast and stable potassium ion storage. *ACS Nano* **13**, 11843–11852 (2019).
33. Lopez-Sanchez, O. et al. Ultrasensitive photodetectors based on monolayer MoS_2 . *Nat. Nanotechnol.* **8**, 497–501 (2013).
34. Akinwande, D. et al. Two-dimensional flexible nanoelectronics. *Nat. Commun.* **5**, 5678 (2014).
35. Chang, H. Y. et al. High-performance, highly bendable MoS_2 transistors with high-K dielectrics for flexible low-power systems. *ACS Nano* **7**, 5446–5452 (2013).

36. Li, S. et al. Humidity-sensitive chemoelectric flexible sensors based on metal-air redox reaction for health management. *Nat. Commun.* **13**, 5416 (2022).
37. Feng, J. et al. Giant moisture responsiveness of VS₂ ultrathin nanosheets for novel touchless positioning interface. *Adv. Mater.* **24**, 1969–1974 (2012).
38. Zhao, J. et al. Highly sensitive MoS₂ humidity sensors array for noncontact sensation. *Adv. Mater.* **29**, 1702076 (2017).
39. Yu, X. G. et al. Skin-integrated wireless haptic interfaces for virtual and augmented reality. *Nature* **575**, 473–479 (2019).
40. Kresse, G. et al. Ab-Initio molecular-dynamics for open-shell transition-metals. *Phys. Rev. B* **48**, 13115–13118 (1993).
41. Perdew, J. P. et al. Generalized gradient approximation made simple. *Phys. Rev. Lett.* **77**, 3865–3868 (1996).
42. Grimme, S. et al. Effect of the damping function in dispersion corrected density functional theory. *J. Comput. Chem.* **32**, 1456–1465 (2011).

Acknowledgements

Z.Zeng thanks the Young Collaborative Research Grant (project no. C1003-23Y) and General Research Fund (GRF) (project no. CityU11308923) support from the Research Grants Council of the Hong Kong Special Administrative Region, China, the Basic Research Project from Shenzhen Science and Technology Innovation Committee in Shenzhen, China (project no. JCYJ20210324134012034), and the Applied Research Grant of City University of Hong Kong (project no. 9667247) and Chow Sang Sang Group Research Fund of City University of Hong Kong (project no. 9229123). Z.Zeng also thanks the funding supported by the Seed Collaborative Research Fund Scheme of State Key Laboratory of Marine Pollution, which receives regular research funding from Innovation and Technology Commission (ITC) of the Hong Kong SAR Government. However, any opinions, findings, conclusions or recommendations expressed in this publication do not reflect the views of the Hong Kong SAR Government or the ITC. X.Y. thanks the support from Research Grants Council of the Hong Kong Special Administrative Region (grant no. RFS2324-1S03) and Shenzhen Science and Technology Innovation Commission (grant no. SGDX20220530111401011). M.G. acknowledges the support from Guangdong Fundamental Research Association (project no. 2022B1515120013), National Natural Science Foundation of China (project no. 52273225) and Guangdong scientific programme (contract no. 2019QN01L057). L.G. thanks the funding support from

National Natural Science Foundation of China (project nos. 52250402, 51991344 and 52025025).

Author contributions

Z. Zeng conceived and guided the project. L.M. designed and performed the synthesis and characterizations of all the materials. Z.G. and X.G.Y. performed the device fabrication and performance test. D.L., T.Y., H.H., J.Z., D.V. and Y.C. helped to analyse the results. Z. Zhang and M.D.G. carried out the cryo-electron microscopy test. M.S., X.L., Y.Z., B.H. and X.C.Z. conducted the DFT calculations. Q.Z. and L.G. performed the HAADF-STEM test of the samples. L.M., Z.G., R.Y., J.L., X.Y. and Z. Zeng drafted the paper. All authors checked the paper and agreed with its content.

Competing interests

The authors declare no conflicts of interest.

Additional information

Supplementary information The online version contains supplementary material available at <https://doi.org/10.1038/s44160-024-00679-2>.

Correspondence and requests for materials should be addressed to M. Danny Gu, Ju Li, Xinge Yu or Zhiyuan Zeng.

Peer review information *Nature Synthesis* thanks Qiaoliang Bao and the other, anonymous, reviewer(s) for their contribution to the peer review of this work. Primary Handling Editor: Alexandra Groves, in collaboration with the *Nature Synthesis* team.

Reprints and permissions information is available at www.nature.com/reprints.

Publisher's note Springer Nature remains neutral with regard to jurisdictional claims in published maps and institutional affiliations.

Springer Nature or its licensor (e.g. a society or other partner) holds exclusive rights to this article under a publishing agreement with the author(s) or other rightsholder(s); author self-archiving of the accepted manuscript version of this article is solely governed by the terms of such publishing agreement and applicable law.

© The Author(s), under exclusive licence to Springer Nature Limited 2024

¹Department of Materials Science and Engineering and State Key Laboratory of Marine Pollution, City University of Hong Kong, Hong Kong, P. R. China. ²Department of Biomedical Engineering, City University of Hong Kong, Hong Kong, P. R. China. ³Department of Applied Biology and Chemical Technology, The Hong Kong Polytechnic University, Hong Kong, P. R. China. ⁴Beijing National Laboratory for Condensed Matter Physics, Institute of Physics, Chinese Academy of Sciences, Beijing, P. R. China. ⁵Eastern Institute for Advanced Study, Eastern Institute of Technology, Ningbo, P. R. China. ⁶Beijing National Center for Electron Microscopy and Laboratory of Advanced Materials, Department of Materials Science and Engineering, Tsinghua University, Beijing, P. R. China. ⁷School of Materials Science and Engineering, Hunan Provincial Key Laboratory of Electronic Packaging and Advanced Functional Materials, Central South University, Changsha, P. R. China. ⁸Institut Européen des Membranes, UMR 5635, ENSCM, CNRS, Université Montpellier, Montpellier, France. ⁹Department of Applied Physics, The Hong Kong Polytechnic University, Hong Kong, P. R. China. ¹⁰Department of Nuclear Science and Engineering and Department of Materials Science and Engineering, Massachusetts Institute of Technology, Cambridge, MA, USA. ¹¹Hong Kong Institute for Clean Energy, City University of Hong Kong, Hong Kong, P. R. China. ¹²Shenzhen Research Institute, City University of Hong Kong, Shenzhen, P. R. China. ¹³These authors contributed equally: Liang Mei, Zhan Gao, Ruijie Yang, Zhen Zhang. ✉e-mail: m.danny.gu@gmail.com; liju@mit.edu; xingeyu@cityu.edu.hk; zhiyuzeng@cityu.edu.hk

Phase-switchable preparation of solution-processable WS₂ mono- or bilayers

In the format provided by the authors and unedited

1 **Contents**

2 **1. Supplementary Figures 1-47**

3 Supplementary Fig. 1 Schematic illustration of 2H-, 1T- and 1T'-WS₂ structures

4 Supplementary Fig. 2 Characterizations of bulk WS₂ powder

5 Supplementary Fig. 3 Galvanostatic discharge curves for the lithium intercalation of
6 WS₂ under different current densities

7 Supplementary Fig. 4 Raman spectra of WS₂ exfoliated under different discharge
8 current densities

9 Supplementary Fig. 5 XPS W4f spectra of WS₂ exfoliated under different discharge
10 current densities

11 Supplementary Fig. 6 Photographs of S-Li_xWS₂ and L-Li_xWS₂ after sonication in DI
12 water

13 Supplementary Fig. 7 XRD pattern of the 2H- and 1T'-WS₂ thin films

14 Supplementary Fig. 8 STEM image of S vacancies in 2H-WS₂ NSs

15 Supplementary Fig. 9 STEM image of S vacancies in 1T'-WS₂ NSs

16 Supplementary Fig. 10 EPR spectrums of exfoliated 2H- and 1T'-WS₂ NSs

17 Supplementary Fig. 11 TEM images of exfoliated 2H- and 1T'-WS₂ NSs

18 Supplementary Fig. 12 SEM images of exfoliated 2H- and 1T'-WS₂ NSs

19 Supplementary Fig. 13 AFM images and thickness distribution of exfoliated 2H- and
20 1T'-WS₂ NSs

21 Supplementary Fig. 14 Discharge curves of Li⁺ intercalation of WSe₂ under different
22 current densities

23 Supplementary Fig. 15 UV-vis spectra of exfoliated WSe₂ NSs solution using different
24 discharge current densities

25 Supplementary Fig. 16 XPS W4f spectra of exfoliated WSe₂ NSs solution using
26 different discharge current densities

27 Supplementary Fig. 17 Discharge curves of Li⁺ intercalation of MoS₂ under different
28 current densities

29 Supplementary Fig. 18 XPS Mo3d and Raman spectra of exfoliated MoS₂ using

30 different discharging current densities

31 Supplementary Fig. 19 EELS spectra of S-Li_xWS₂ electrode

32 Supplementary Fig. 20 XRD pattern of bulk WS₂, S-Li_xWS₂ and L-Li_xWS₂

33 Supplementary Fig. 21 EELS spectra of L-Li_xWS₂ electrode

34 Supplementary Fig. 22 Raman and XPS W4f spectra of S-Li_xWS₂ and L-Li_xWS₂

35 Supplementary Fig. 23 XPS S2p spectra of bulk WS₂, S-Li_xWS₂, L-Li_xWS₂, and the

36 corresponding exfoliated 2H- and 1T'-WS₂ NSs

37 Supplementary Fig. 24 XPS Li 1s spectra of S-Li_xWS₂, L-Li_xWS₂ and Li foil

38 Supplementary Fig. 25 Phase of 2H and 1T' formation energy of different intercalated

39 Li content in Li_xWS₂

40 Supplementary Fig. 26 Atomic models of optimized different Li-intercalated 2H-

41 Li_xWS₂ structures

42 Supplementary Fig. 27 Atomic models of optimized different Li-intercalated 1T'-

43 Li_xWS₂ structures

44 Supplementary Fig. 28 Galvanostatic discharge/charge curves of S-Li_xWS₂ and L-

45 Li_xWS₂

46 Supplementary Fig. 29 EPR spectrums of bulk WS₂, intercalated WS₂ and

47 deintercalated WS₂

48 Supplementary Fig. 30 Theoretical simulations of the formation of the SEI under large

49 and small discharge current densities

50 Supplementary Fig. 31 SEM image of 2H-WS₂ based device

51 Supplementary Fig. 32 Schematic diagram of a home-made setup for humidity sensing

52 performance test

53 Supplementary Fig. 33 Resistance of 2H-WS₂ based humid sensor under different RH

54 Supplementary Fig. 34 schematic of the humidity sensing mechanism under different

55 RH

56 Supplementary Fig. 35 The calculated energy for generating different S vacancies in

57 1T'-WS₂

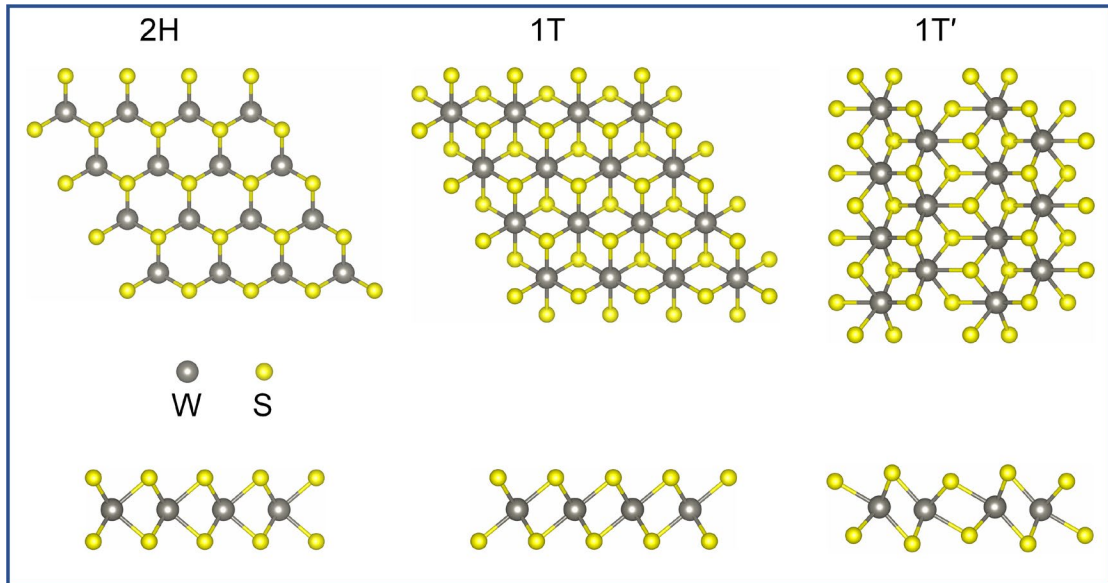
58 Supplementary Fig. 36 Adsorption energy of H₂O molecule on 2H- and 1T'-WS₂

59 Supplementary Fig. 37 Projected density of states for 2H- and 1T'-WS₂ with S
60 vacancies
61 Supplementary Fig. 38 The protection performance of different masks via using 2H-
62 WS₂ based humidity sensor
63 Supplementary Fig. 39 Photograph of humidity sensor set-up for voice recognition
64 Supplementary Fig. 40 Response current of 2H-WS₂ while speaking different words
65 Supplementary Fig. 41 Response current of 2H-WS₂ while speaking different words
66 Supplementary Fig. 42 Response current of 2H-WS₂ while speaking different words
67 Supplementary Fig. 43 Response current of 2H-WS₂ while speaking different words
68 Supplementary Fig. 44 The long-term stability of 2H-WS₂ based humidity sensor
69 performance
70 Supplementary Fig. 45 The flexibility of 2H-WS₂ based humidity sensor device
71 Supplementary Fig. 46 Original current distribution of 5×5 humid sensor array in none-
72 contact finger localization experiments
73 Supplementary Fig. 47 2H-WS₂ based humidity sensor array used for monitoring baby
74 diaper wetness

75 **2. Supplementary Tables 1-2**

76 Supplementary Table 1 DFT calculated phase formation energy and corresponding
77 interlayer spacing for lithium intercalation of WS₂
78 Supplementary Table 2 Comparison of humidity sensing performance of the developed
79 2H- and 1T'-WS₂ NSs with other reported humidity sensors.

80 **3. Supplementary References**

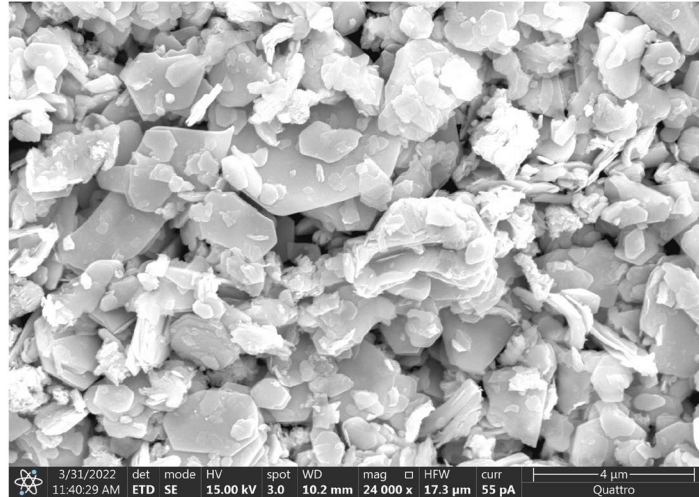
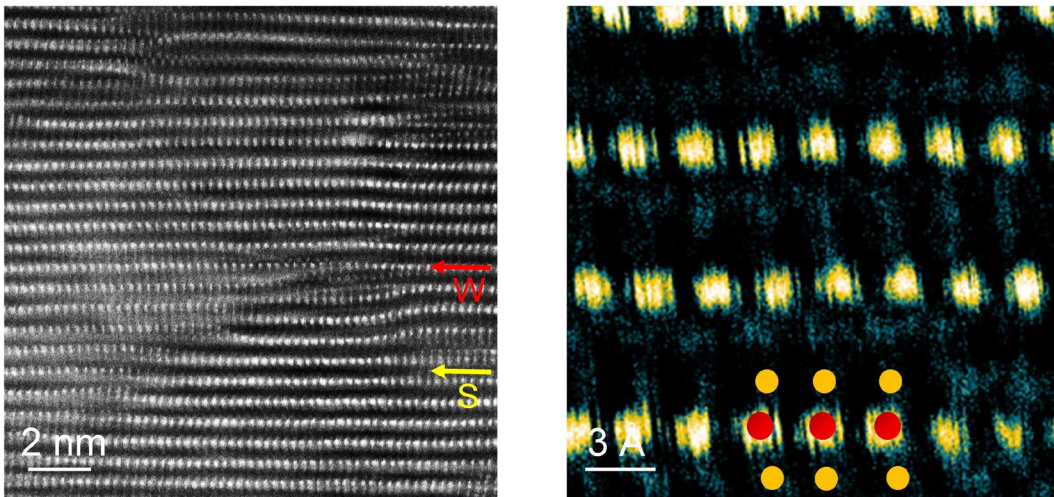


81

82 **Supplementary Fig. 1 | Atomic models of different phases of WS₂.** Schematic

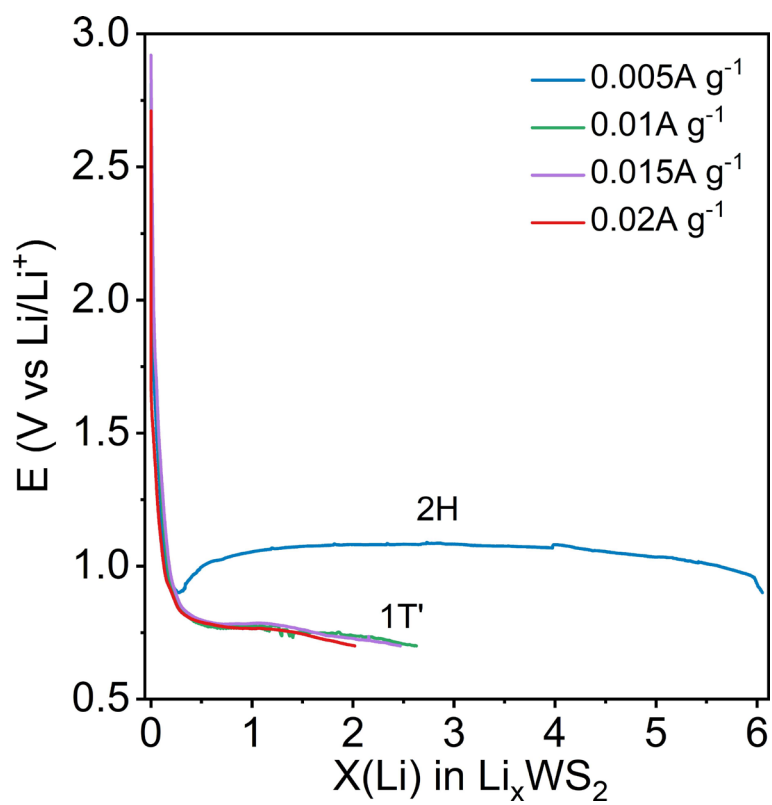
83 illustration of 2H-, 1T- and 1T'-WS₂ structures. Upside: top view of the structures;

84 downside: side view of the structures.

a**b**

85

86 **Supplementary Fig. 2 | Characterizations of bulk WS₂ powder.** **a**, SEM images of
87 WS₂ powder. The layered structures of bulk WS₂ are clearly observed, and the size are
88 in the range of 2-5 μm. **b**, Cross-sectional HAADF-STEM images of bulk WS₂ with
89 different magnifications. The 2H structure is clearly observed from the magnified image
90 of bulk WS₂. Red and yellow circles denote the W and S atoms.

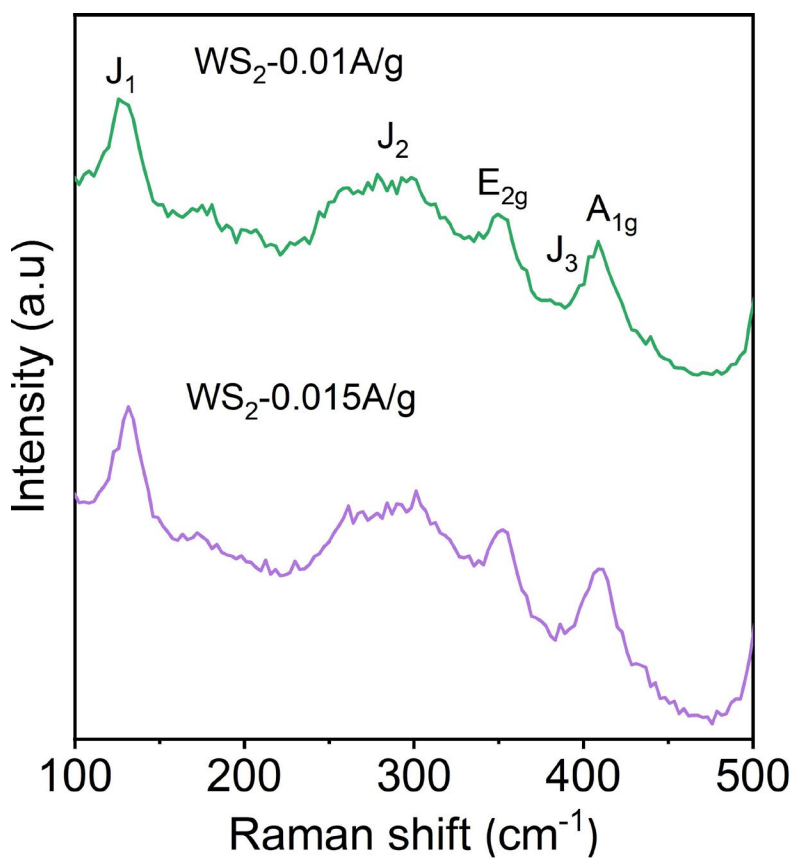


91

92 **Supplementary Fig. 3 | Electrochemical Li^+ intercalation of WS_2 .** Galvanostatic

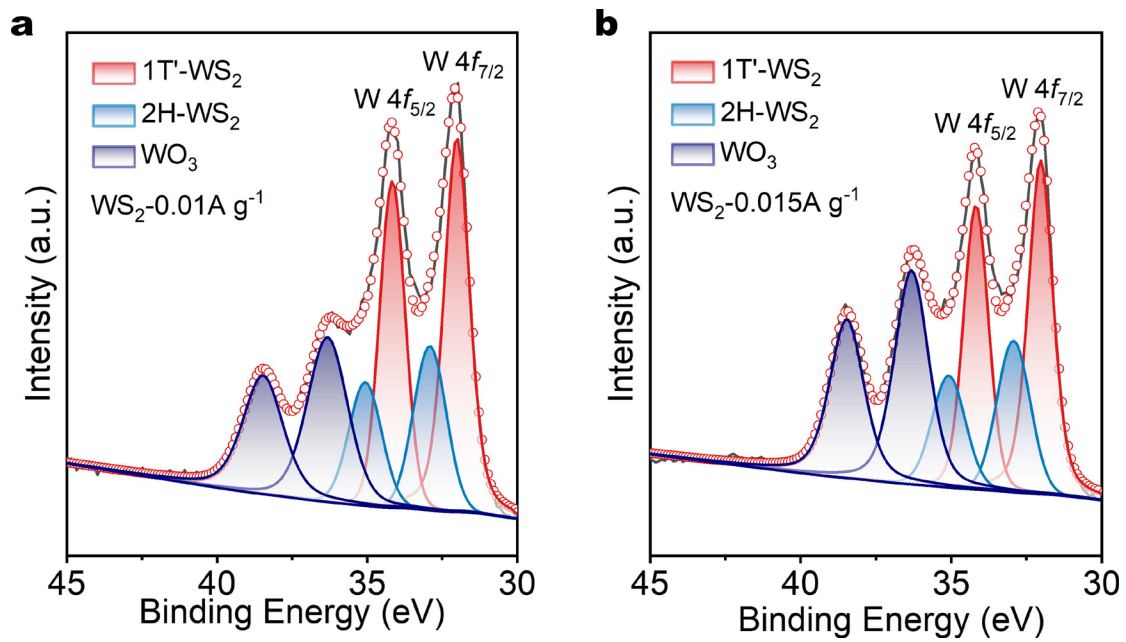
93 discharge curves for the lithium intercalation of WS_2 under different discharge current

94 densities.



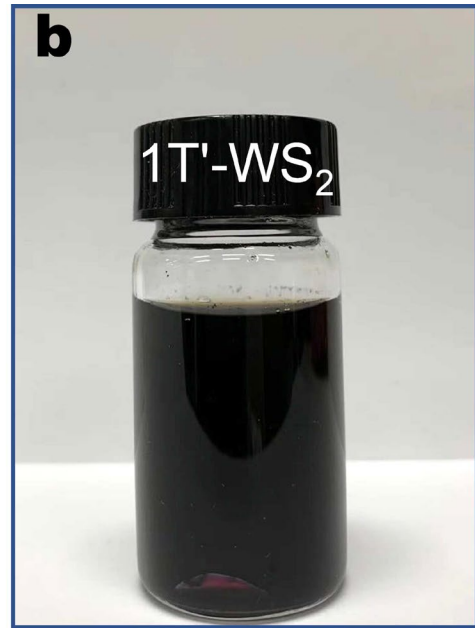
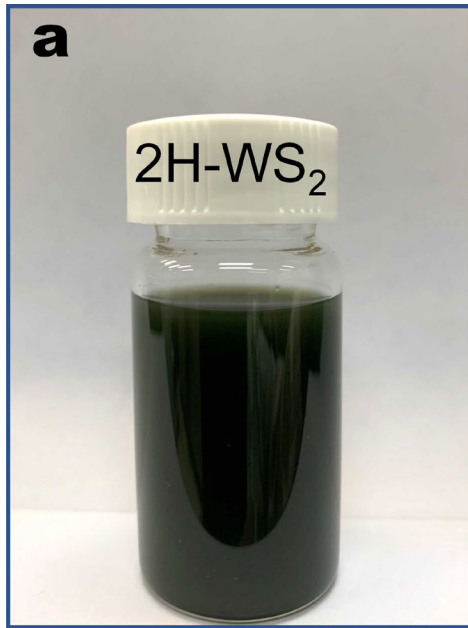
95

96 **Supplementary Fig. 4 | Characterization of exfoliated WS₂.** Raman spectra of WS₂
 97 exfoliated under discharge current densities of 0.01 A g⁻¹ and 0.015 A g⁻¹, right-side
 98 show the corresponding photographs of exfoliated solution.



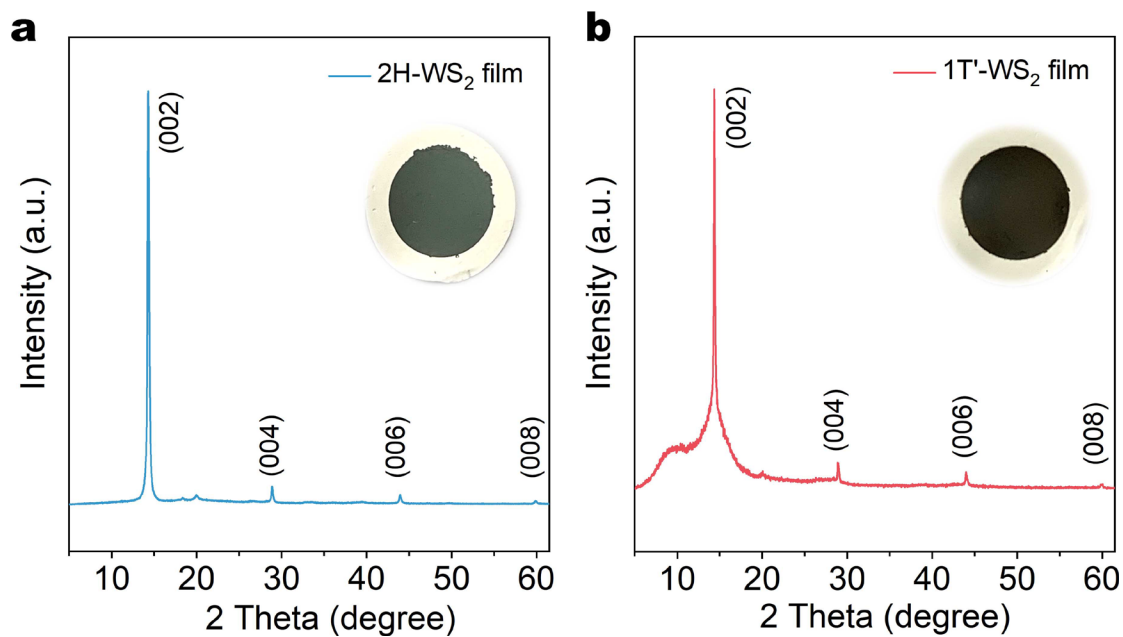
99

100 **Supplementary Fig. 5 | Characterization of exfoliated WS₂.** XPS W4f spectra of WS₂
 101 exfoliated under discharge current densities of **a** 0.01 A g⁻¹ and **b** 0.015 A g⁻¹.



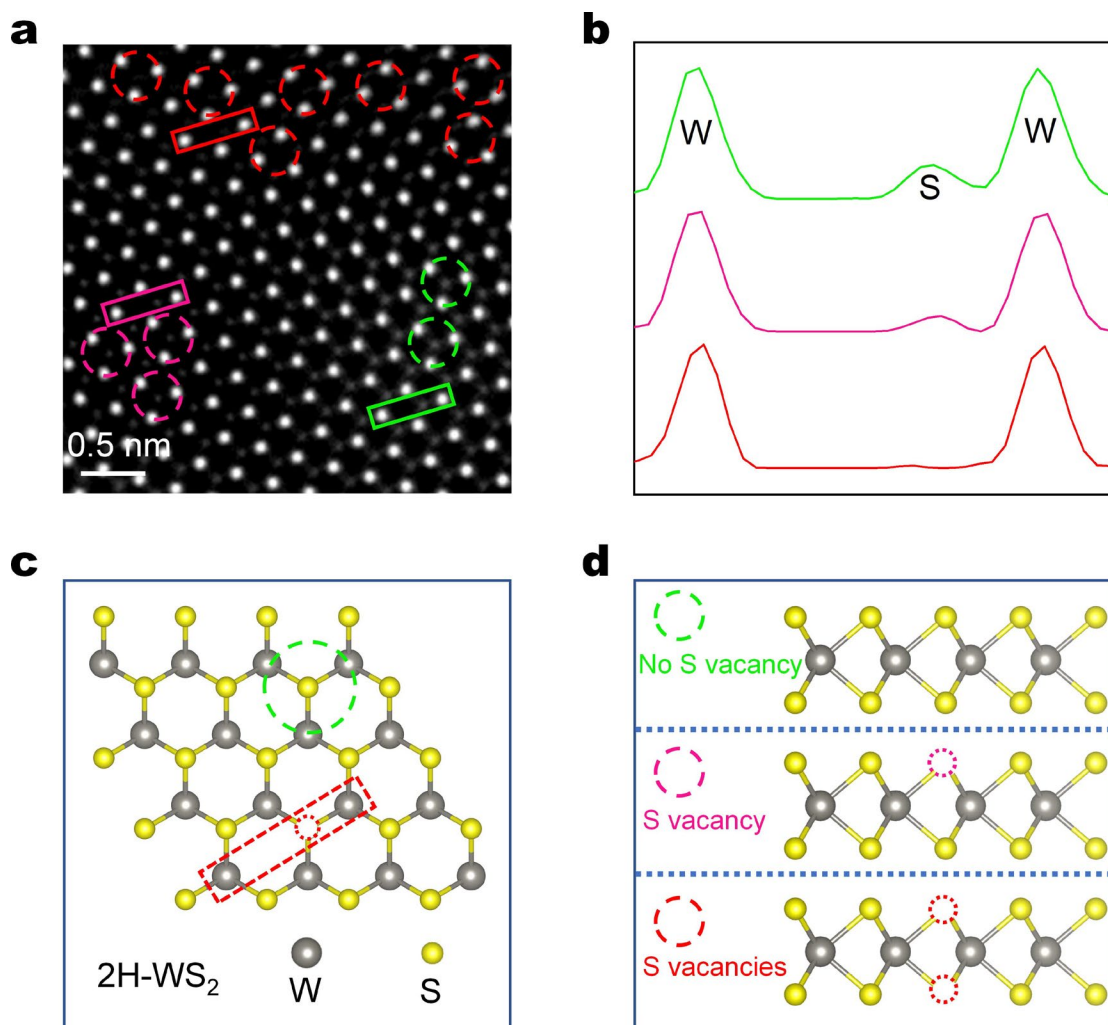
102

103 **Supplementary Fig. 6 | Photographs of exfoliated 2H- and 1T'-WS₂ NSs solution**
104 **before washing steps.** The S-Li_xWS₂ and L-Li_xWS₂ electrodes were well exfoliated in
105 ethanol and DI water, respectively. After 5-10 min, two opaque suspensions exhibited
106 dark green and dark black obtained. S-Li_xWS₂, L-Li_xWS₂ denote as Li⁺ intercalation of
107 WS₂ by small and large discharge current densities, respectively.



108

109 **Supplementary Fig. 7 | a-b, XRD patterns of the 2H- and 1T'-WS₂ thin films.** These
 110 thin films were prepared via vacuum filtration of the corresponding exfoliated WS₂ NSs
 111 onto polyvinylidene difluoride (PVDF) substrate, demonstrating well-controlled
 112 assembly along the (001) direction. Insets show the photographs of the corresponding
 113 films. The 2H-WS₂ film exhibits a green color, whereas 1T'-WS₂ film appears black.



114

115 **Supplementary Fig. 8 | Structure characterization of exfoliated 2H-WS₂ NSs. a,**

116 Atomic-resolution annular dark field (ADF) images showing different types of S

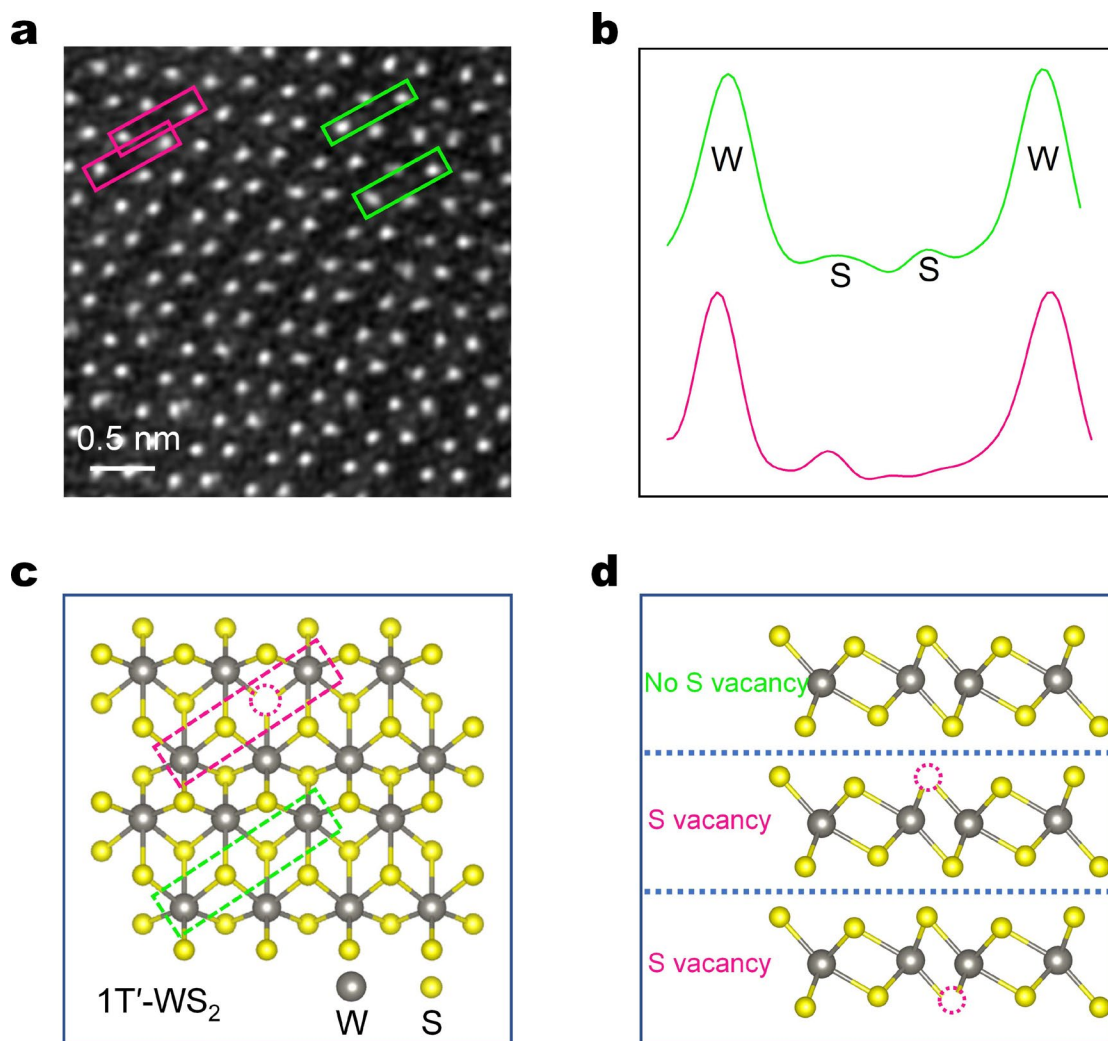
117 vacancies in 2H-WS₂. **b,** Line intensity profile scans along the red, green and magenta

118 boxed atoms in **a**. **c-d,** Schematic of S vacancies in the atomic model of 2H-WS₂ from

119 the top and main view. HAADF-STEM results confirm the existence of S vacancies in

120 exfoliated 2H-WS₂ NSs, which are consistent with electron paramagnetic resonance

121 (EPR) results (**Supplementary Fig. 10**).



122

123

Supplementary Fig. 9 | Structure characterization of exfoliated 1T'-WS₂ NSs. a,

124

Atomic-resolution annular dark field (ADF) images showing different types of S

125

vacancies in 1T'-WS₂. **b,** Line intensity profile scans along the green and magenta

126

boxed atoms in **a**. **c-d,** Schematic of S vacancies in the atomic model of 1T'-WS₂ from

127

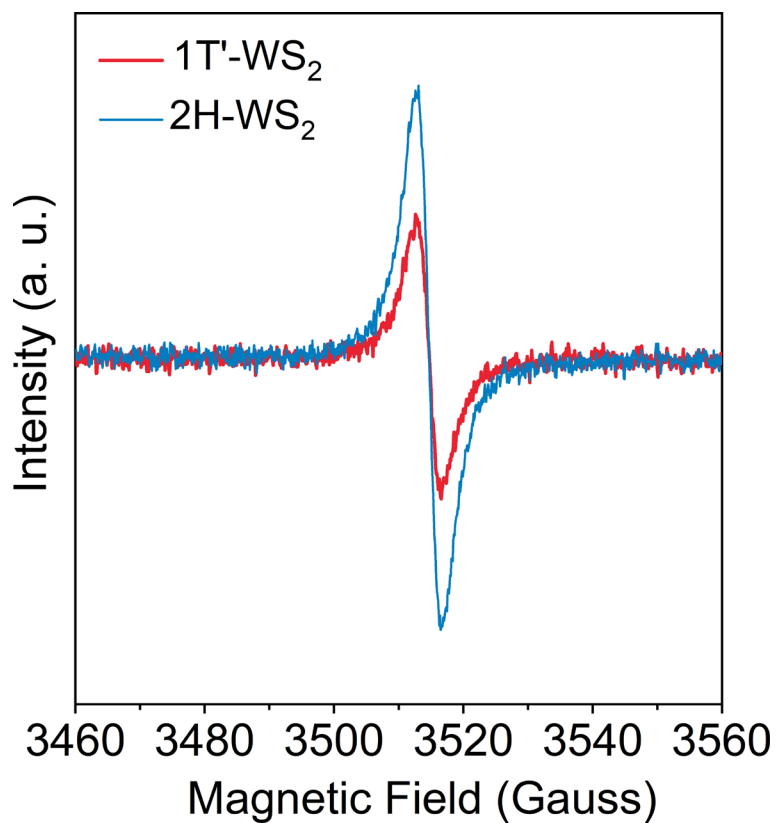
the top and main view. HAADF-STEM results confirm the existence of S vacancies in

128

exfoliated 1T'-WS₂ NSs, which agree well with electron paramagnetic resonance (EPR)

129

results (**Supplementary Fig. 10**).

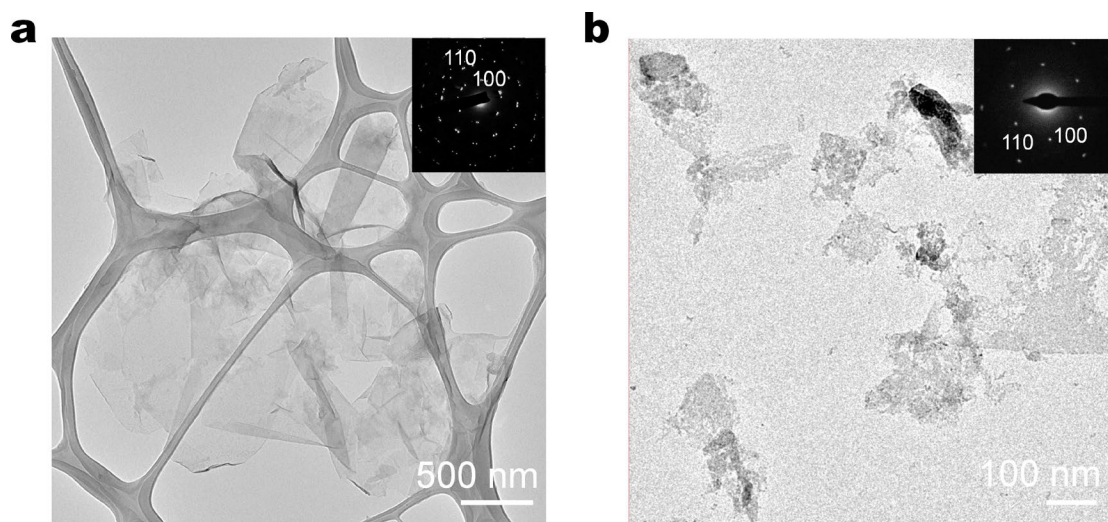


130

131 **Supplementary Fig. 10 | Structure characterization of 2H- and 1T'-WS₂ NSs.** EPR

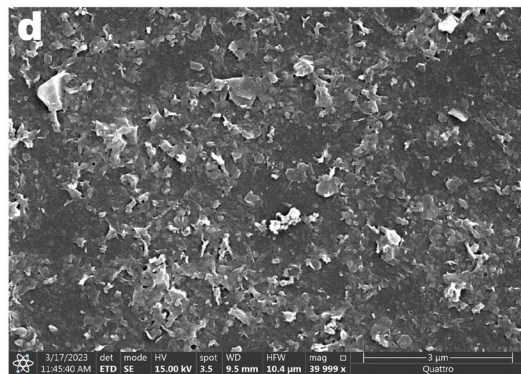
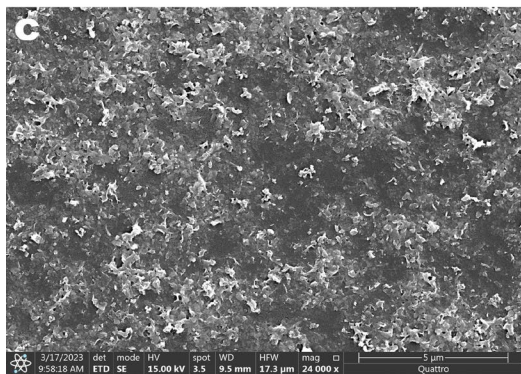
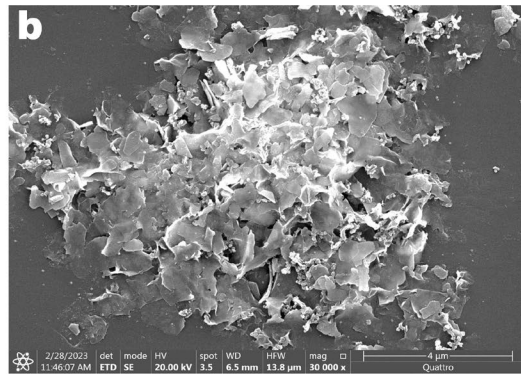
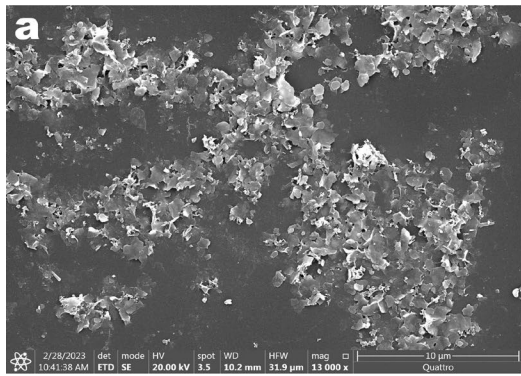
132 spectrums of exfoliated 2H- and 1T'-WS₂ NSs, revealing that there exist more S

133 vacancies in 2H-WS₂ than that in 1T'-WS₂ NSs.



134

135 **Supplementary Fig. 11 | Morphology characterization of exfoliated 2H- and 1T'-**
 136 **WS₂.** TEM images of **a** 2H- and **b** 1T'-WS₂. Both the 2H- and 1T'-WS₂ exhibit the NSs
 137 morphology in TEM images with lateral sizes ranging from 300-600 nm and 100-200
 138 nm, respectively. The variance in size for 2H- and 1T'-WS₂ NSs can be ascribed to a
 139 higher quantity of intercalated lithium within the interlayer of WS₂ for L-Li_xWS₂ in
 140 comparison to S-Li_xWS₂. This disparity leads to a reduction in the NSs size after the
 141 exfoliation process. S-Li_xWS₂, L-Li_xWS₂ denote as Li⁺ intercalation of WS₂ by small
 142 and large discharge current densities, respectively.

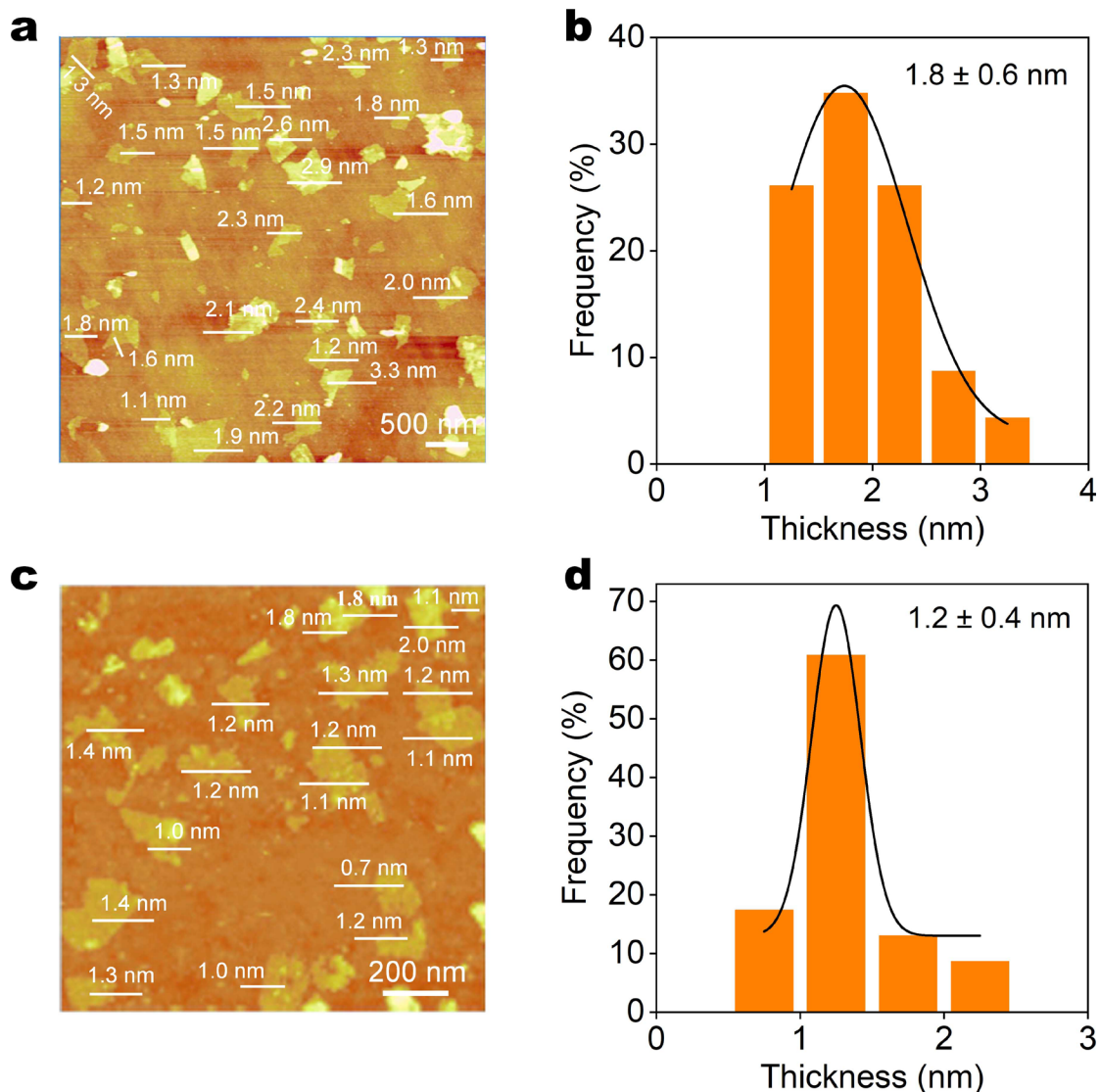


143

144

145

Supplementary Fig. 12 | Morphology characterization of exfoliated 2H- and 1T'-WS₂. SEM images of 2H- (a-b) and 1T'-WS₂ (c-d) NSs with different magnification.



146

147 **Supplementary Fig. 13 | Characterization of 2H- and 1T'-WS₂ NSs.** AFM images

148 of the exfoliated 2H- (a) and 1T'-WS₂ NSs (c). The corresponding thickness distribution

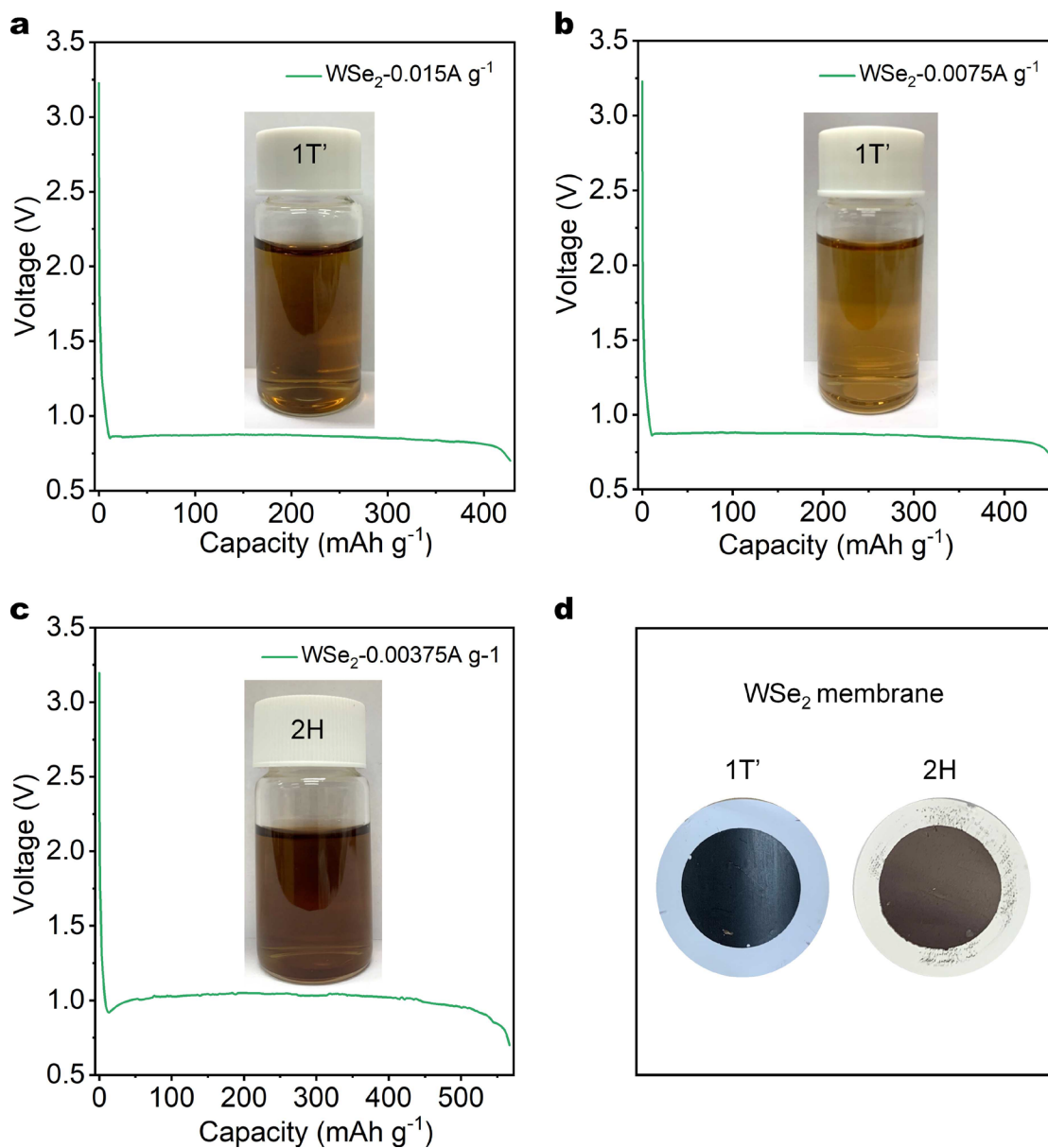
149 histogram are shown in (b) and (d). The mean thickness of the 2H-WS₂ NSs is

150 determined to be 1.8 nm with a standard deviation of 0.6 nm. In contrast, the

151 corresponding values for the 1T'-WS₂ NSs are 1.2 nm and 0.4 nm, respectively. These

152 analyses conclusively demonstrate the fabrication of bilayer 2H-WS₂ and monolayer

153 1T'-WS₂ NSs.



154

155 **Supplementary Fig. 14 | Electrochemical Li^+ intercalation and exfoliation of WSe_2 .**

156 **a-c**, Discharge curves of Li^+ intercalation of WSe_2 under different discharge current

157 densities, inset show the photographs of corresponding exfoliated nanosheets solution.

158 **d**, The photographs of 1T'- and 2H WSe_2 membrane prepared via vacuum filtration of

159 the corresponding exfoliated nanosheets solution onto porous substrate.

160 We can also achieve phase-switchable preparation of WSe_2 by adjusting the discharging

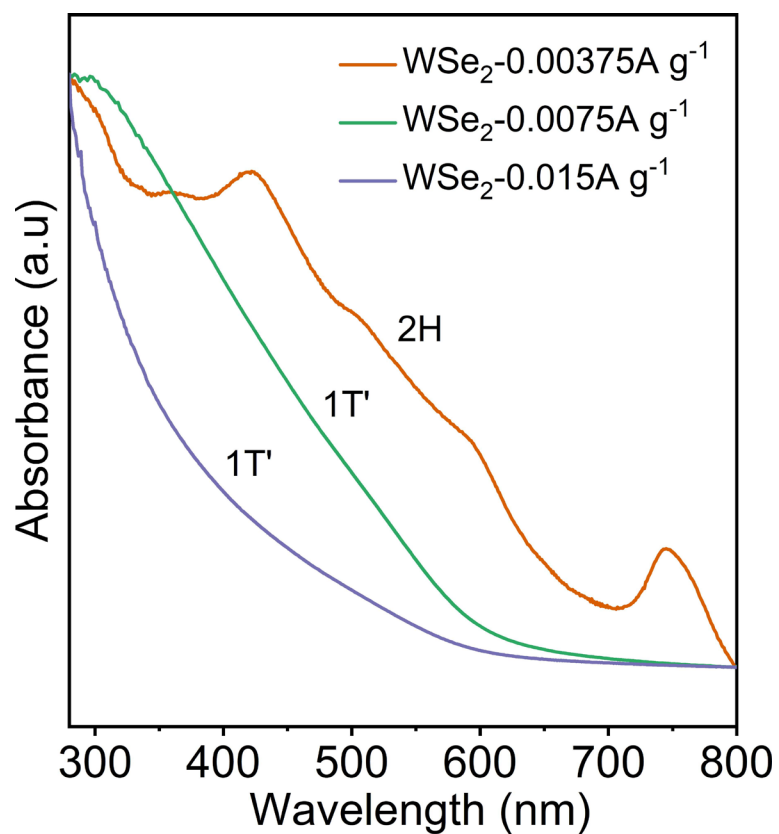
161 current density. As shown in **Supplementary Fig. 14a-c**, decreasing the discharge

162 current density from 0.015 A g^{-1} to 0.00375 A g^{-1} results in a discharge curve similar to

163 that observed in WS_2 . Following exfoliation, the dispersions of WSe_2 NSs exhibits a

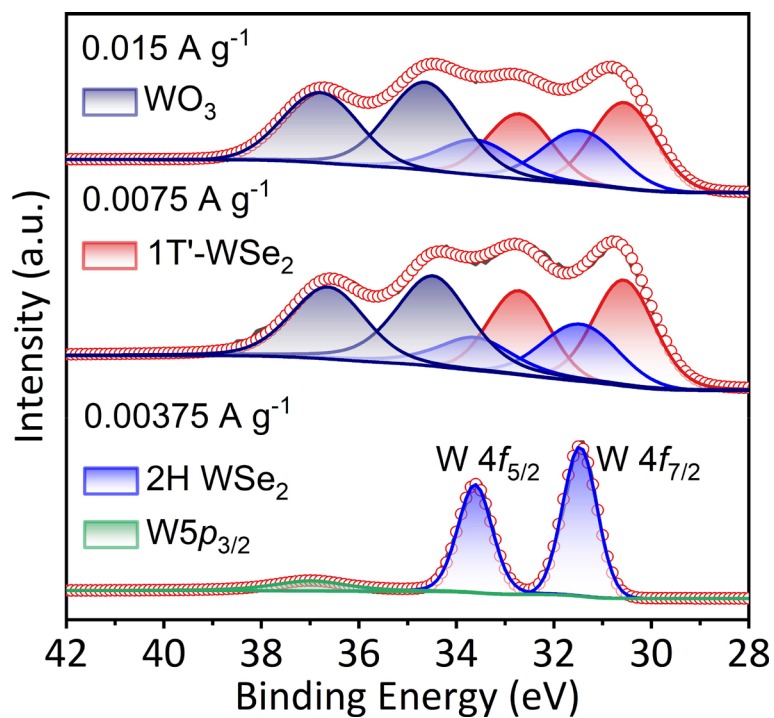
164 brown color (**Supplementary Fig. 14c**), indicating partial absorption in the visible

165 range. This is confirmed by the ultraviolet-visible absorption spectrum
166 (**Supplementary Fig. 15**), which verifies the formation of semiconducting 2H phase
167 WSe₂ NSs under a low discharging current density (0.00375 A g⁻¹). In contrast, the
168 dispersions of WSe₂ NSs exfoliated at high discharge current densities (0.0075 A g⁻¹
169 and 0.015 A g⁻¹) appears light black (**Supplementary Fig. 14a, b, d**), suggesting
170 complete and featureless absorption in the visible range (**Supplementary Fig. 15**). This
171 change indicates a phase transition, resulting in the formation of metallic 1T/1T' phase
172 WSe₂ NSs under high discharge current densities.



173

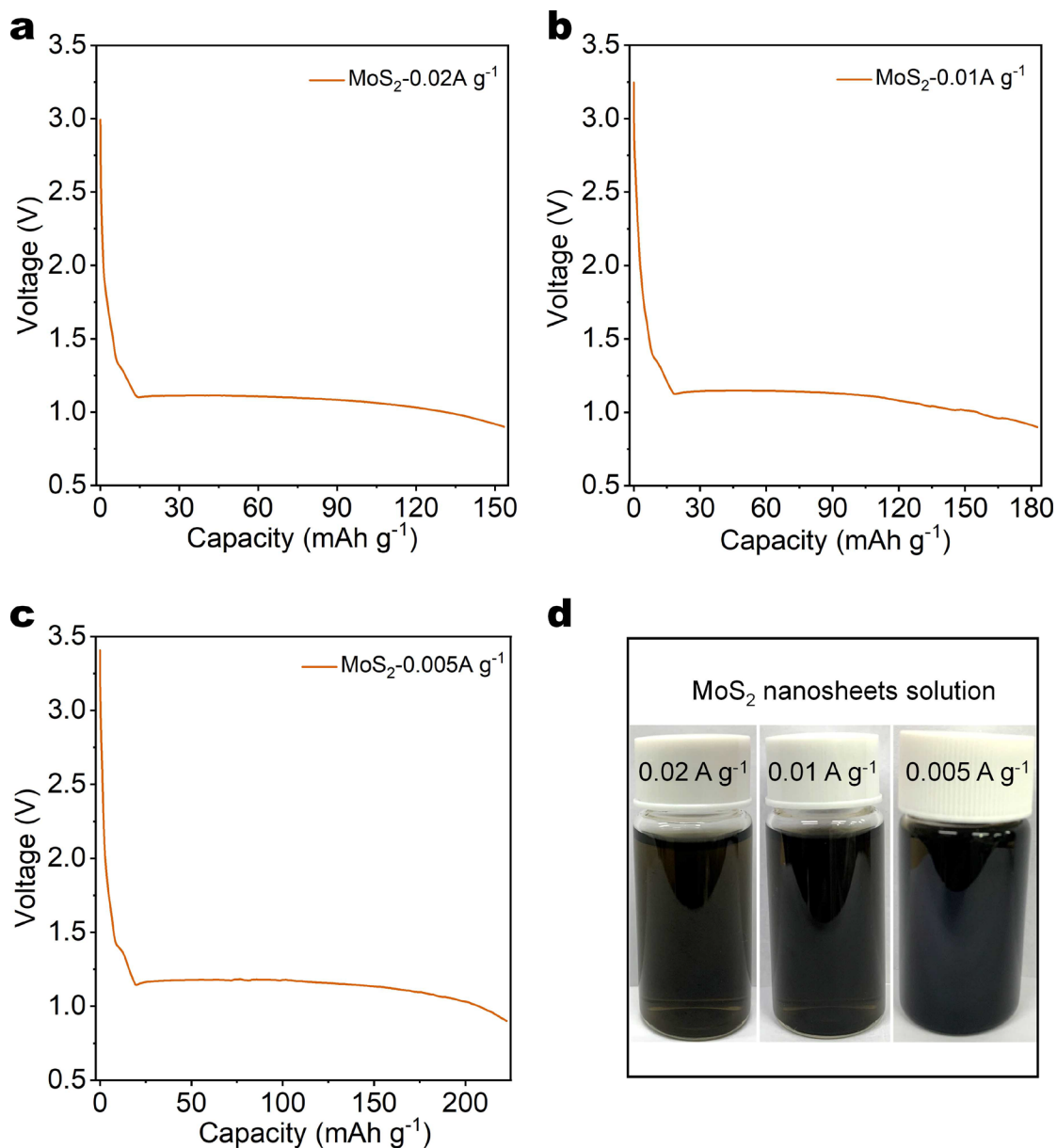
174 **Supplementary Fig. 15 | Characterization of exfoliated WSe₂.** Visible-near infrared
175 absorption spectra of exfoliated WSe₂ NSs solution that fabricated under different
176 discharge current densities.



177

178 **Supplementary Fig. 16 | Characterization of exfoliated WSe₂.** XPS W 4f spectra of
 179 exfoliated WSe₂ prepared by Li⁺ intercalation under different discharge current
 180 densities.

181 Additionally, XPS spectra confirm that a small discharge current density (0.00375 A g⁻¹
 182 ¹) yields pure 2H phase WSe₂ (**Supplementary Fig. 16**), whereas large discharge
 183 current densities (0.0075 A g⁻¹, 0.015 A g⁻¹) induce a phase transition from 2H to 1T',
 184 leading to predominantly 1T' phase WSe₂. Thus, this method enables phase-switchable
 185 preparation of WSe₂ NSs.



186

187 **Supplementary Fig. 17 | Electrochemical Li⁺ intercalation and exfoliation of MoS₂.**

188 **a-c**, Discharge curves of Li⁺ intercalation of MoS₂ under different discharge current

189 densities. **d**, The corresponding photographs of exfoliated MoS₂ NSs solution.

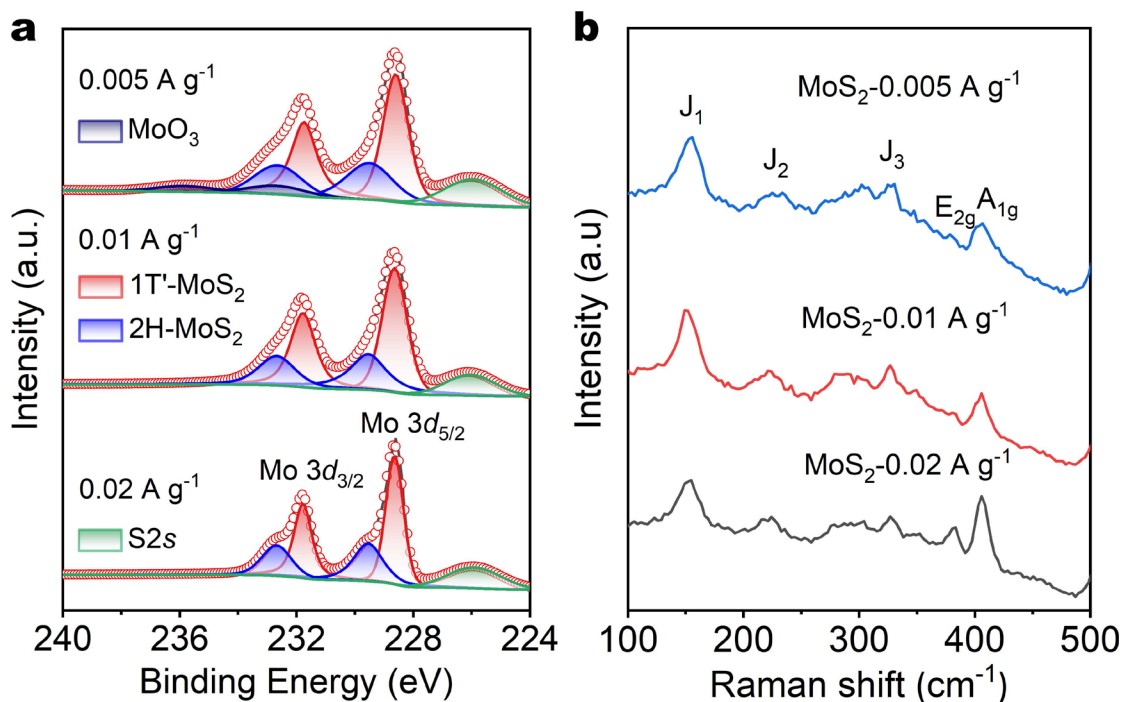
190 As shown in **Supplementary Fig. 17a-c**, applying different discharge current densities

191 for Li⁺ intercalation of MoS₂ slightly increased the intercalated Li⁺ amounts upon

192 decreasing the current density. After exfoliation, all the MoS₂ NSs dispersions showed

193 black color (**Supplementary Fig. 17d**), indicating the formation of metallic 1T' phase

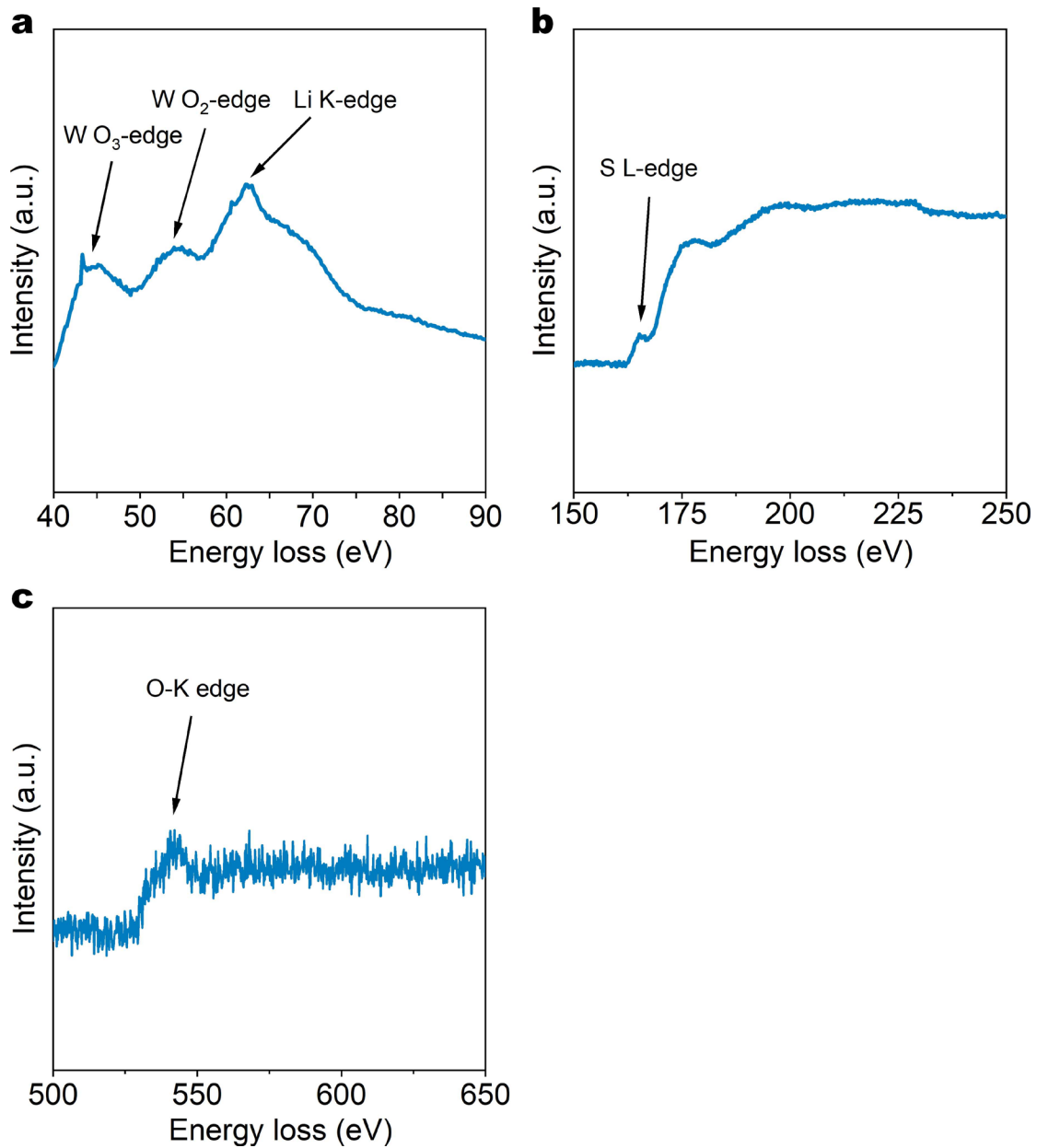
194 MoS₂ NSs under these discharge current densities.¹



195

196 **Supplementary Fig. 18 | Characterization of exfoliated MoS₂.** a, XPS Mo 3d and b,
 197 Raman spectra of exfoliated MoS₂ prepared by Li⁺ intercalation under different
 198 discharge current densities.

199 Furthermore, both XPS (**Supplementary Fig. 18a**) and Raman spectra
 200 (**Supplementary Fig. 18b**) confirmed that these exfoliated MoS₂ samples, prepared
 201 under different discharge current densities, all exhibit a 1T' phase-dominated structure.
 202 No pure 2H MoS₂ was prepared by tuning the discharge current densities. Therefore,
 203 this phase-switchable method is not suitable for MoS₂.

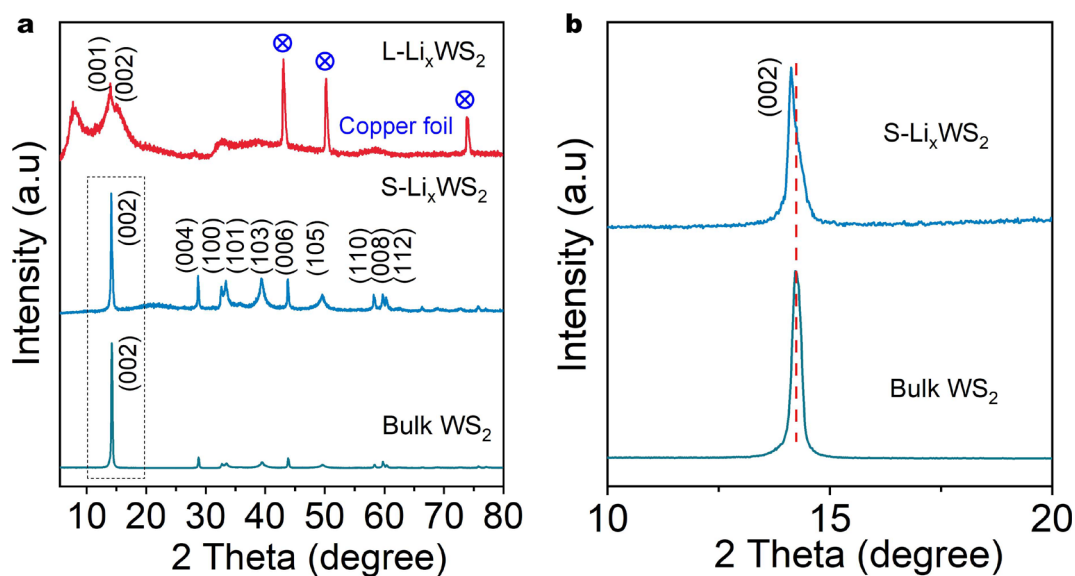


204

205 **Supplementary Fig. 19 | EELS spectra of S-Li_xWS₂ electrode. a, Li K-edge, W O₂-**

206 **edge and W O₃-edge. b, S L-edge. c, O K-edge. S-Li_xWS₂ denotes as Li⁺ intercalation**

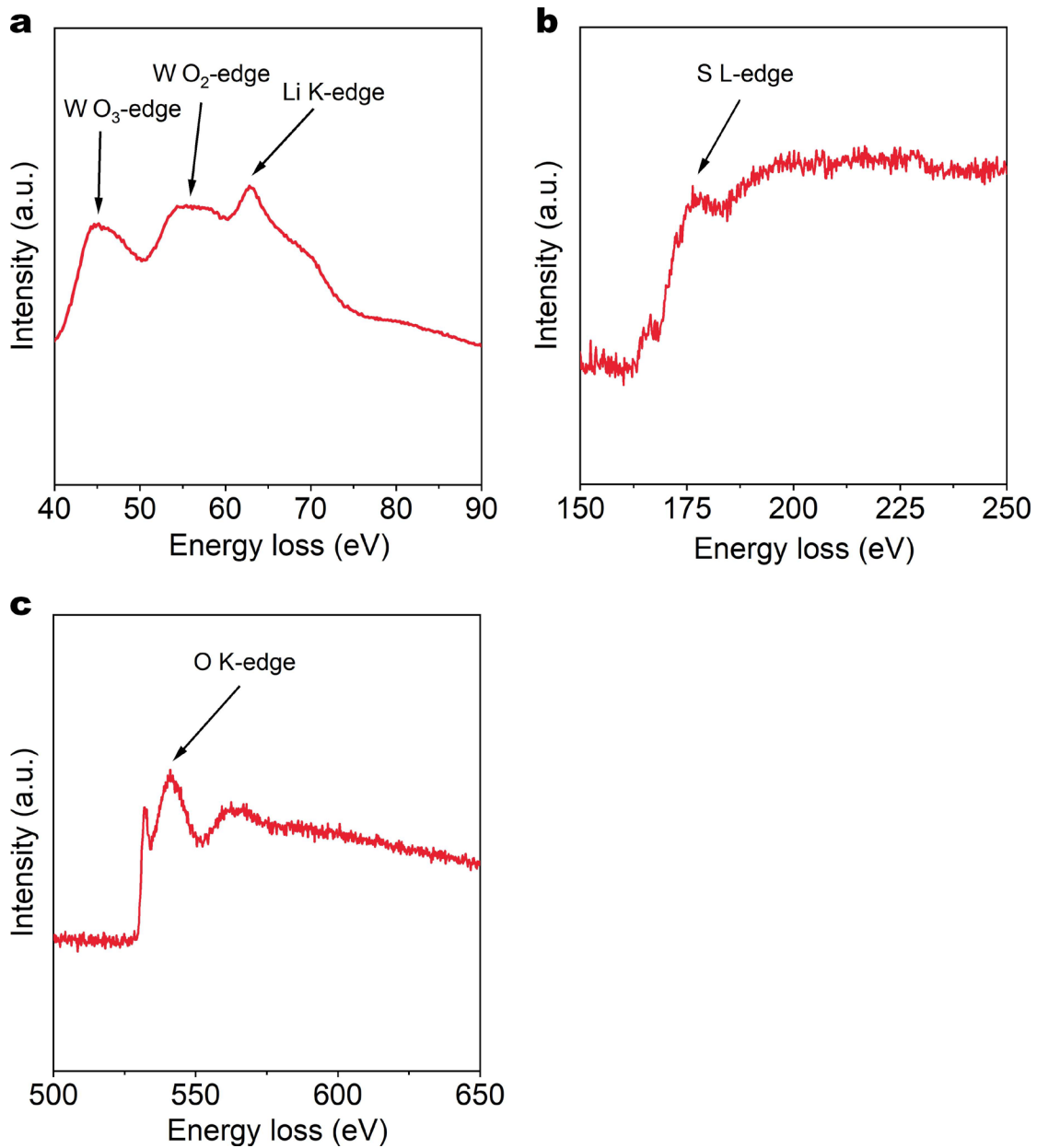
207 **of WS₂ by a small discharge current density.**



208

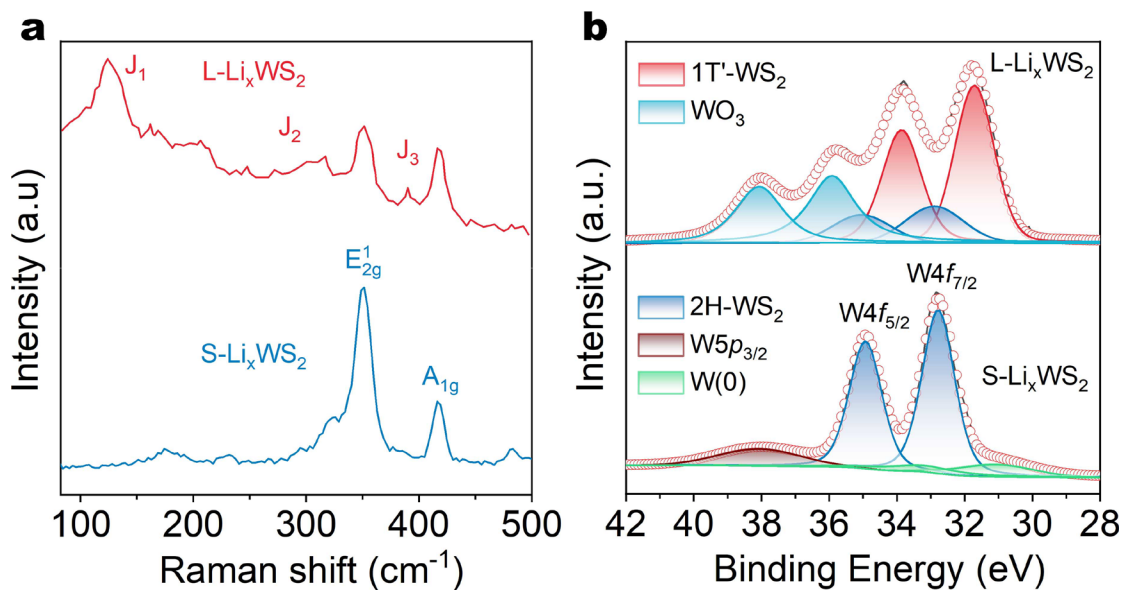
209 **Supplementary Fig. 20 | Characterizations of S-Li_xWS₂ and L-Li_xWS₂.** a, XRD
 210 patterns of bulk WS₂, S-Li_xWS₂ and L-Li_xWS₂. b, Magnified XRD patterns of the (002)
 211 peak of bulk WS₂ (bottom) and S-Li_xWS₂ (top) from the area within the dotted line in
 212 a. S-Li_xWS₂, L-Li_xWS₂ denote as Li⁺ intercalation of WS₂ by small and large discharge
 213 current densities, respectively.

214 X-ray diffraction (XRD) analysis reveals an expansion of the interlayer galleries after
 215 lithiation. The (002) peak shifts from 14.30° in bulk WS₂ to 14.13° in S-Li_xWS₂ and
 216 13.96° in L-Li_xWS₂, indicating an increase in interlayer spacing from 6.19 to 6.26 Å
 217 and 6.34 Å, respectively. Additionally, the peak at 14.17° in L-Li_xWS₂ can be attributed
 218 to the (001) plane of Li-intercalated 1T'-WS₂,^{2,3} providing further confirmation of the
 219 phase transition occurring in this lithium intercalation pathway. Notably, the intensity
 220 of the characteristic peaks of hexagonal 2H-WS₂ decreases significantly in L-Li_xWS₂
 221 due to the loss of long-range order resulting from the formation of both 2H- and 1T'
 222 phases.⁴ Furthermore, the peak at 7.87° in L-Li_xWS₂ is formed by the hydration,⁴ which
 223 may contribute to the oxidation of L-Li_xWS₂, as analyzed in the XPS spectrum
 224 (**Supplementary Fig. 22b**). In contrast, all the peaks in S-Li_xWS₂ can be indexed to
 225 2H-WS₂ (PDF-08-0237), indicating that no phase transition occurs during lithium
 226 intercalation using small discharge current. These results are highly consistent with
 227 Raman (**Supplementary Fig. 22a**), XPS (**Supplementary Fig. 22b**, **Supplementary**
 228 **Fig. 23**) and HAADF-STEM (**Fig. 2d, j**) results.



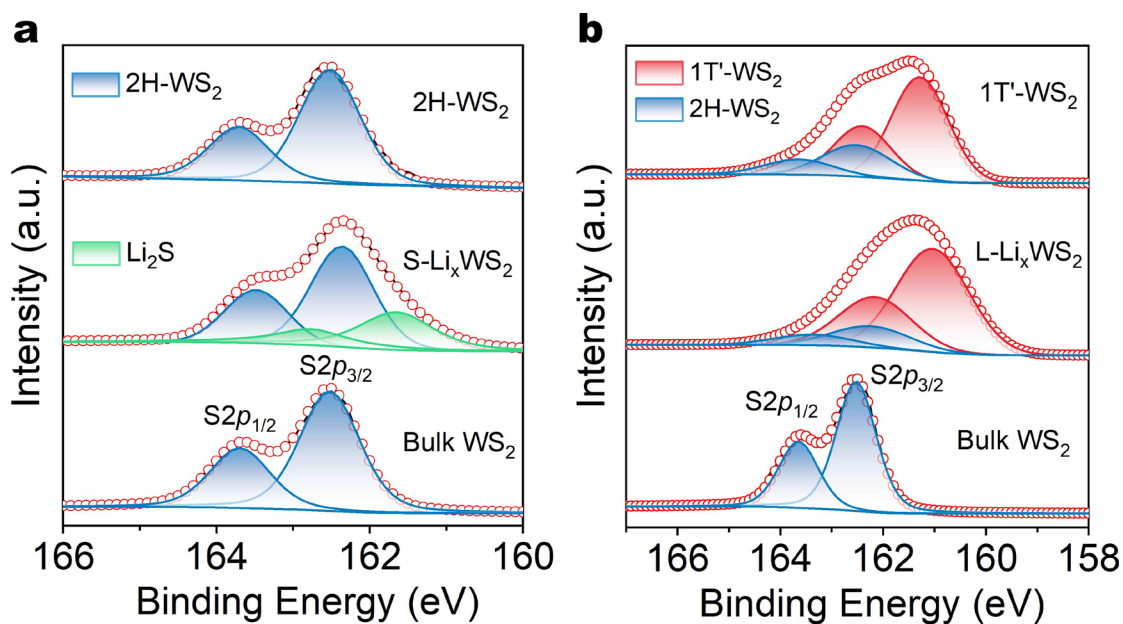
229

230 **Supplementary Fig. 21 | EELS spectra of L-Li_xWS₂ electrode. a,** Li K-edge, W O₂-
 231 edge and W O₃-edge. **b,** S L-edge. **c,** O K-edge. L-Li_xWS₂ denotes as Li⁺ intercalation
 232 of WS₂ by a large discharge current density.



233

234 **Supplementary Fig. 22 | Characterizations of S-Li_xWS₂ and L-Li_xWS₂.** **a**, Raman
 235 spectrum **b**, and W 4f XPS spectrum. S-Li_xWS₂, L-Li_xWS₂ denote as Li⁺ intercalation
 236 of WS₂ by small and large discharge current densities, respectively.



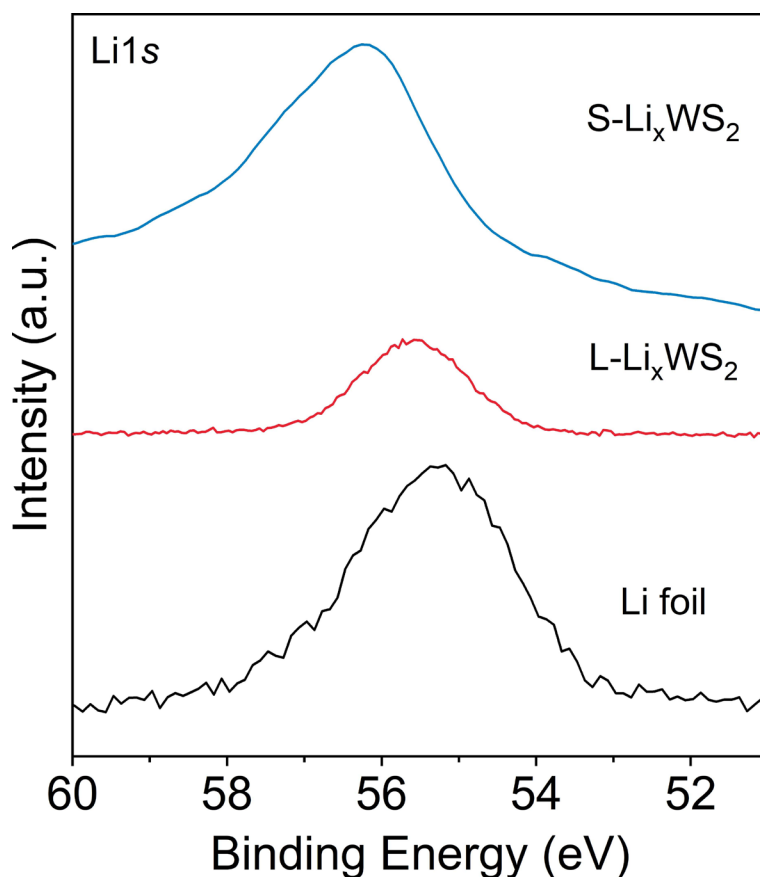
237

238 **Supplementary Fig. 23 | a-b, S 2p XPS spectrum of bulk WS₂, S-Li_xWS₂, L-Li_xWS₂,**
 239 **as well as exfoliated 2H- and 1T'-WS₂.** S-Li_xWS₂, L-Li_xWS₂ denote as Li⁺
 240 intercalation of WS₂ by small and large discharge current densities, respectively.

241 As shown in **Supplementary Fig. 23a**, both bulk WS₂ and the corresponding exfoliated
 242 WS₂ exhibit the same peak positions for S2p_{3/2-1/2} (162.52 and 163.64 eV). However,
 243 these peaks show a slight shift of approximately 0.14 eV toward lower binding energy
 244 for discharged S-Li_xWS₂. This shift can be attributed to electron donation from
 245 intercalated Li to WS₂.⁴ However, the limited electron transfer is insufficient to induce
 246 the phase transition,^{5,6} keeping S-Li_xWS₂ in the 2H phase. Conversely, in addition to
 247 the doublets at 162.52 and 163.64 eV, assigned to the S2p_{3/2-1/2} of 2H-WS₂, two
 248 dominant peaks at lower binding energies of 162.40 and 161.28 eV corresponding to
 249 1T'-WS₂ are also noted (**Supplementary Fig. 23b**). These XPS results confirm the
 250 absence of phase transition for S-Li_xWS₂ and the subsequent exfoliation process, while
 251 a phase transition from 2H to 1T' occurred for L-Li_xWS₂ and the corresponding
 252 exfoliated product. These findings are consistent with the results obtained from Raman
 253 (**Fig. 1d, Supplementary Fig. 22a**) and HAADF-STEM analyses (**Fig. 2d, j**).

254 Notably, the peaks corresponding to W(0) and Li₂S are evident in the W4f
 255 (**Supplementary Fig. 22b**) and S2p (**Supplementary Fig. 23a**) spectra of S-Li_xWS₂,

256 indicating that partial WS_2 decomposed into $\text{W}(0)$ and Li_2S during the lithium
257 intercalation. These results aligned well with the observation of S vacancies in the
258 cross-sectional HAADF-STEM image of $\text{S-Li}_x\text{WS}_2$ (**Fig. 2d**).

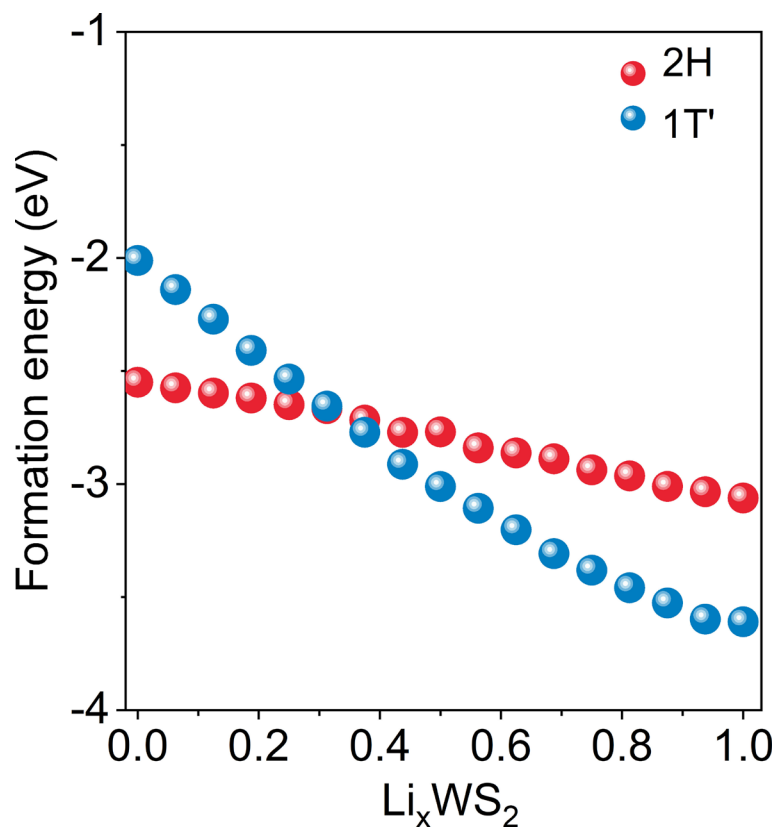


259

260 **Supplementary Fig. 24 | High-resolution XPS Li1s spectra of S-Li_xWS₂, L-Li_xWS₂**
 261 **and Li foil.** Three samples are tested in the same batch. S-Li_xWS₂, L-Li_xWS₂ denote as
 262 Li⁺ intercalation of WS₂ by small and large discharge current densities, respectively.

263 As shown in **Supplementary Fig. 24**, the binding energy of Li in Li foil, L-Li_xWS₂,
 264 and S-Li_xWS₂ is measured at 55.24 eV, 55.57 eV and 56.25 eV, respectively. These
 265 values reveal that the valence of Li in L-Li_xWS₂ is slightly higher than that in Li foil,
 266 which is indicative of electrons transferring from the intercalated Li to WS₂.¹ However,
 267 the valence of Li in L-Li_xWS₂ is significantly lower than that in S-Li_xWS₂, primarily
 268 due to the presence of the solid electrolyte interphase (SEI) and Li₂S in S-Li_xWS₂.
 269 Furthermore, it's worth noting that the peak intensity in L-Li_xWS₂ is notably weaker
 270 compared to S-Li_xWS₂.

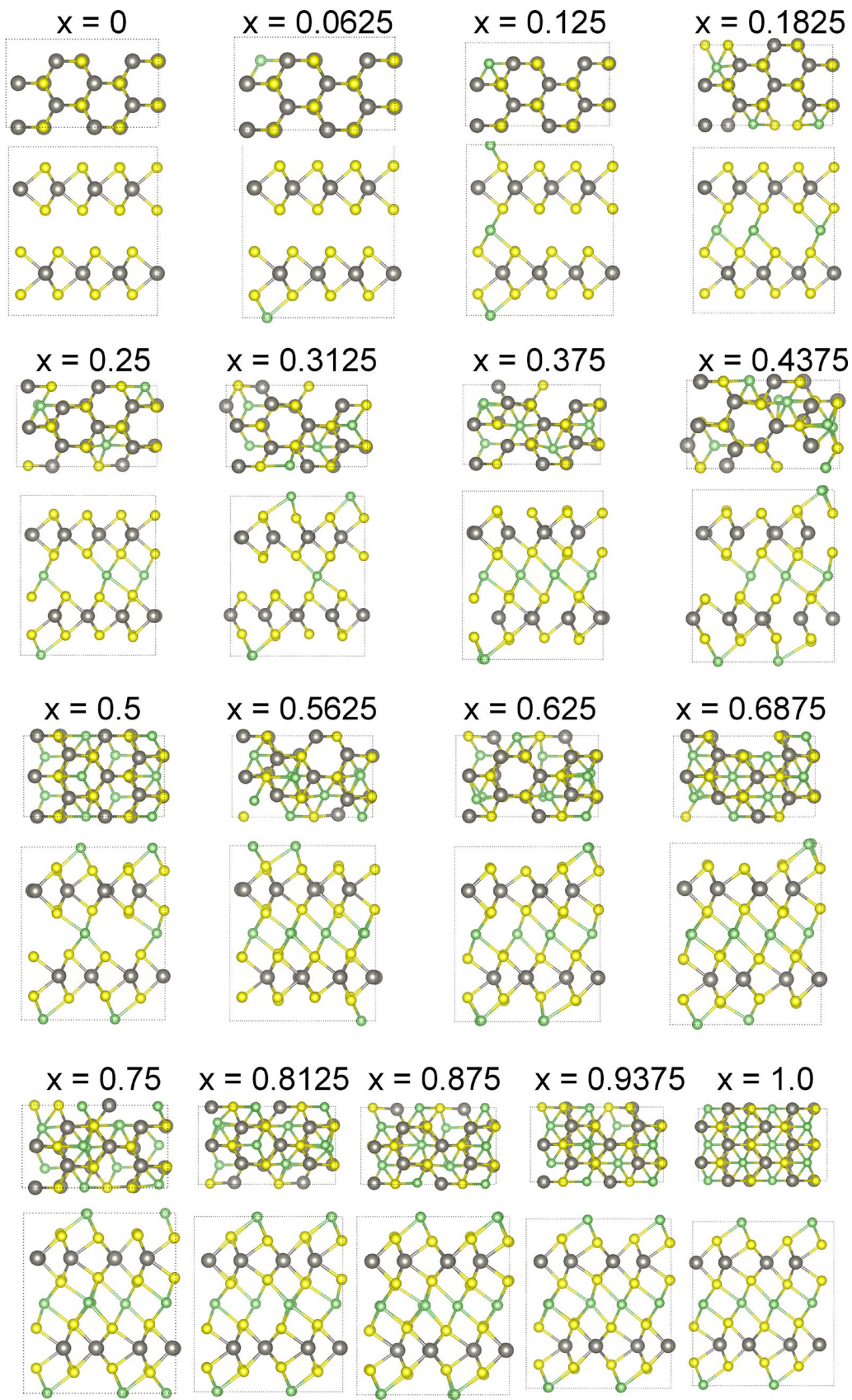
271 This observation likely stems from the increased concentration of intercalated Li within
 272 the surface SEI of S-Li_xWS₂ and the formation of Li₂S (**Fig. 2a-c, f**). Notably, the XPS
 273 technique exactly performs surface measurements.



274

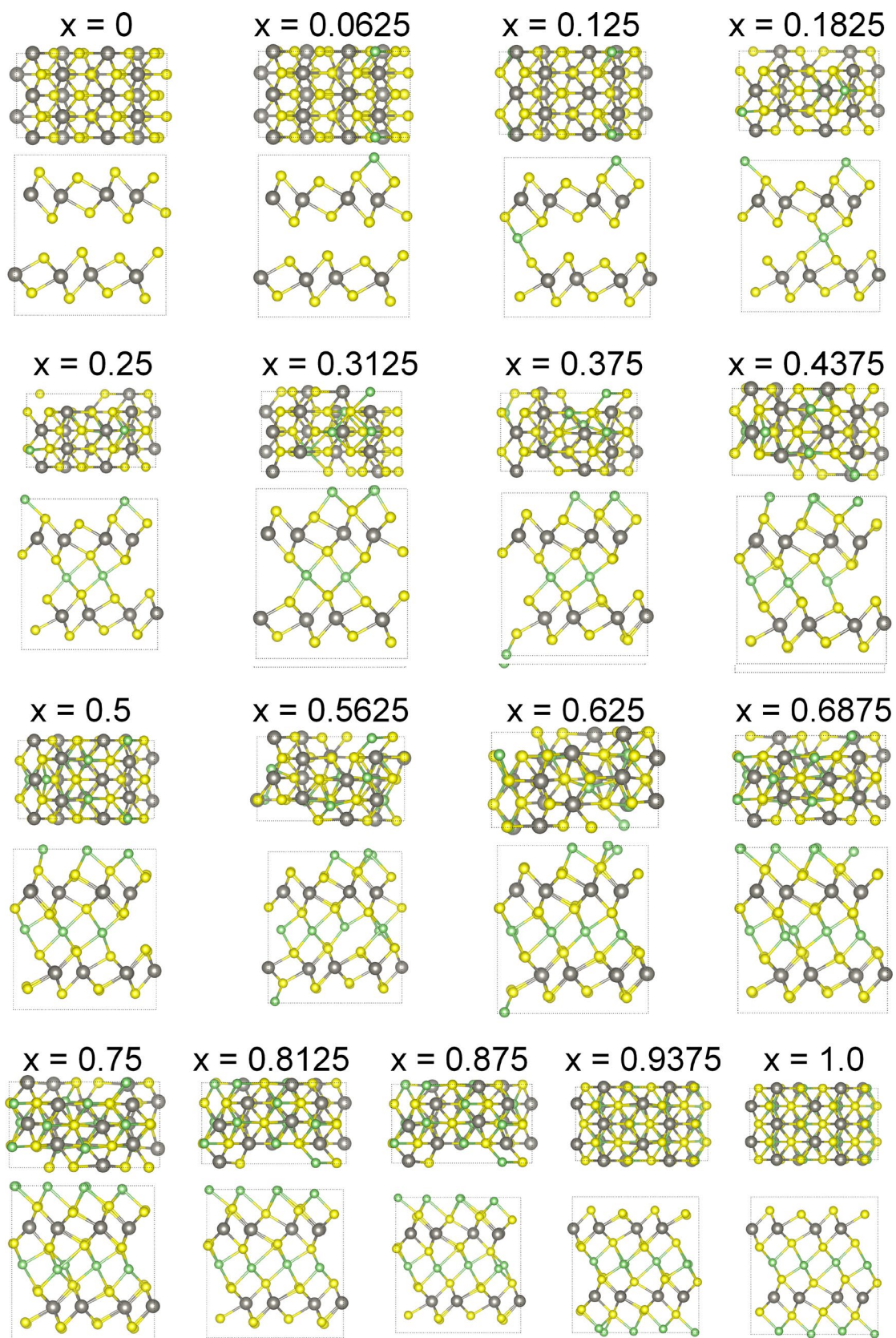
275 **Supplementary Fig. 25 | Phase formation energy of different intercalated Li**
 276 **content in Li_xWS₂.**

277 As illustrated in **Supplementary Fig. 25**, when the intercalated Li content (x) in the
 278 interlayer spacing of WS₂ exceeds 0.3, the formation energy for 1T'-WS₂ becomes more
 279 negative than that for 2H-WS₂. This suggests a phase transition from 2H to 1T' occurs
 280 because the energy is more favorable for the 1T' structure.



281

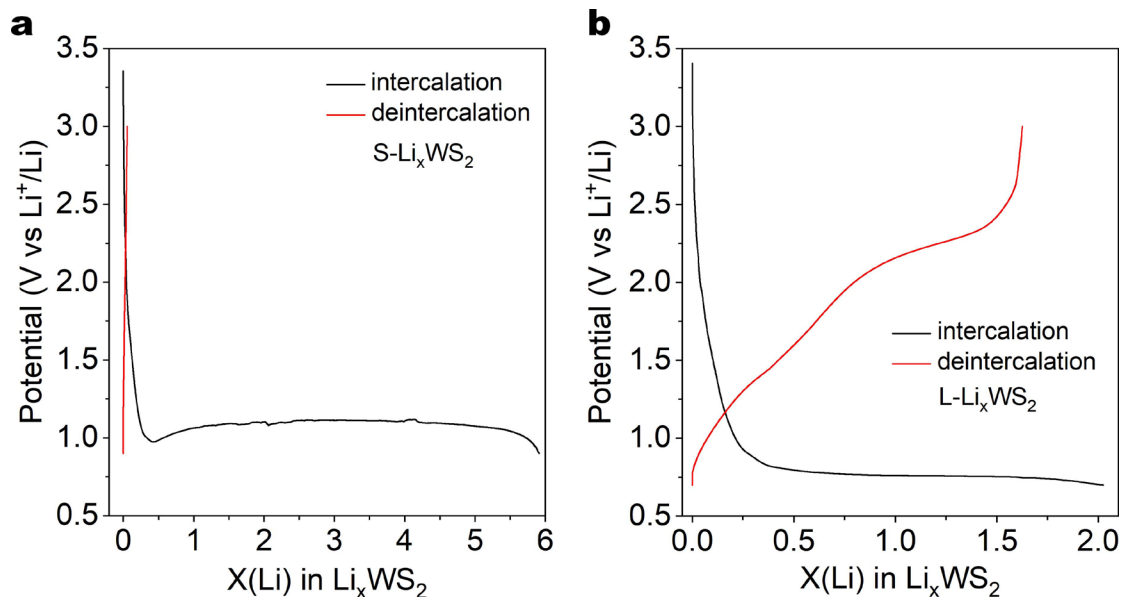
282 **Supplementary Fig. 26 | Top and side views of optimized Li-intercalated 2H-WS₂**
 283 **structures. x denote as the mole ratio of Li versus WS₂ (Li_xWS₂).**



284

285 **Supplementary Fig. 27 | Top and side views of optimized Li-intercalated 1T'-WS₂**

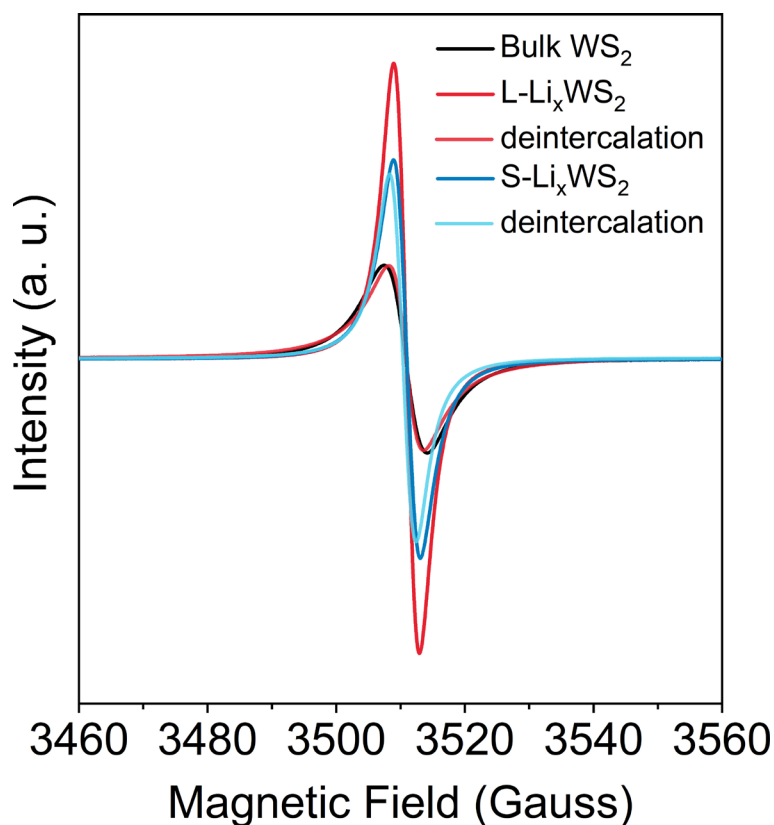
286 **structures.** x denote as the mole ratio of Li versus WS₂ (Li _{x} WS₂).



287

288 **Supplementary Fig. 28 | Galvanostatic charge/discharge profiles of WS₂.** **a**,
 289 discharge /charge current at 0.005 A g⁻¹ and cutoff voltage at 0.9 V. **b**, discharge /charge
 290 current at 0.02 A g⁻¹ and cutoff voltage at 0.7 V. S-Li_xWS₂, L-Li_xWS₂ denote as Li⁺
 291 intercalation of WS₂ by small and large discharge current densities, respectively.

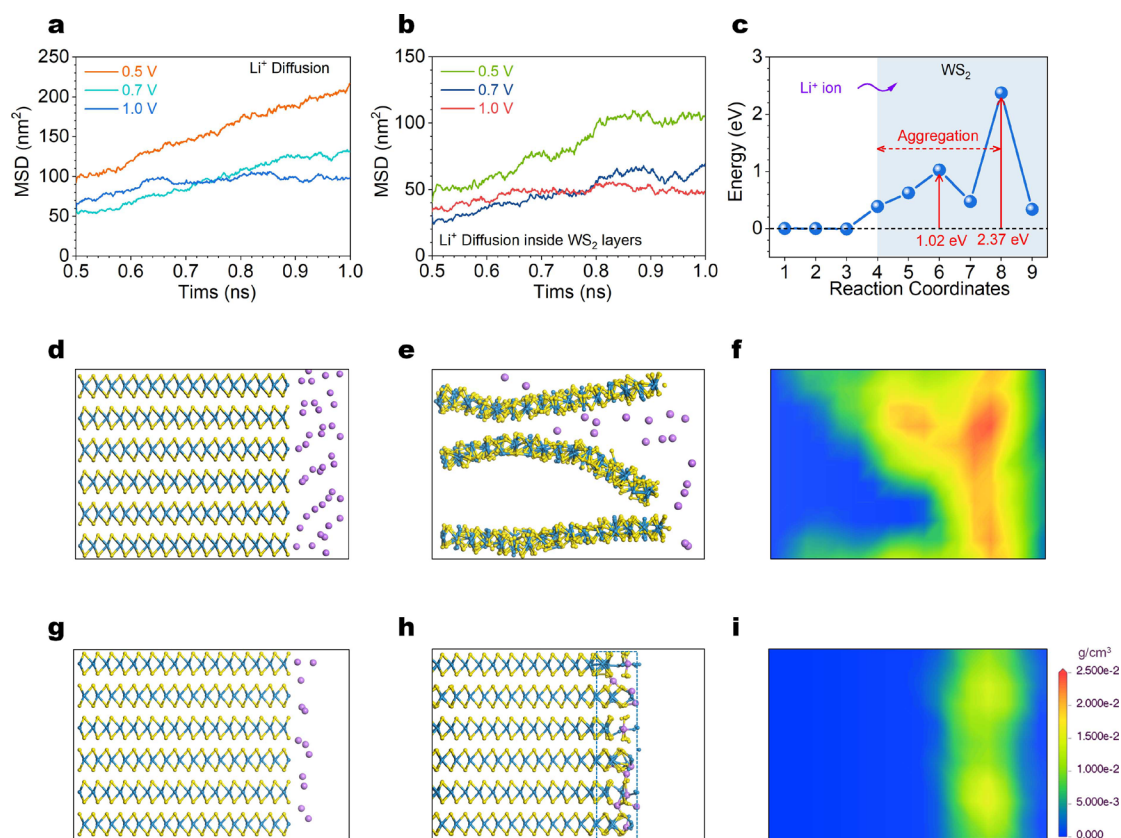
292 As shown in **Supplementary Fig. 28a**, when operating with a smaller current during
 293 the discharge/charge process, a significant portion of the lithium (about 99.06%) cannot
 294 be effectively deintercalated. This leads to a rapid completion of the charge process.
 295 This outcome is a result of a substantial portion of the lithium in S-Li_xWS₂ not
 296 intercalating into the interlayer of WS₂ but rather forming the SEI and Li₂S on the
 297 surface. Consequently, S-Li_xWS₂ maintains its 2H phase. The reactions responsible for
 298 generating the SEI and Li₂S are irreversible, which significantly shortens the duration
 299 of the charge process. Conversely, in the discharge/charge process using a larger current
 300 (**Supplementary Fig. 28b**), about 81.32% of the lithium can be successfully extracted
 301 from the L-Li_xWS₂. This is because lithium can readily penetrate into the interlayer of
 302 WS₂, causing a phase transition, which is a reversible process.



303

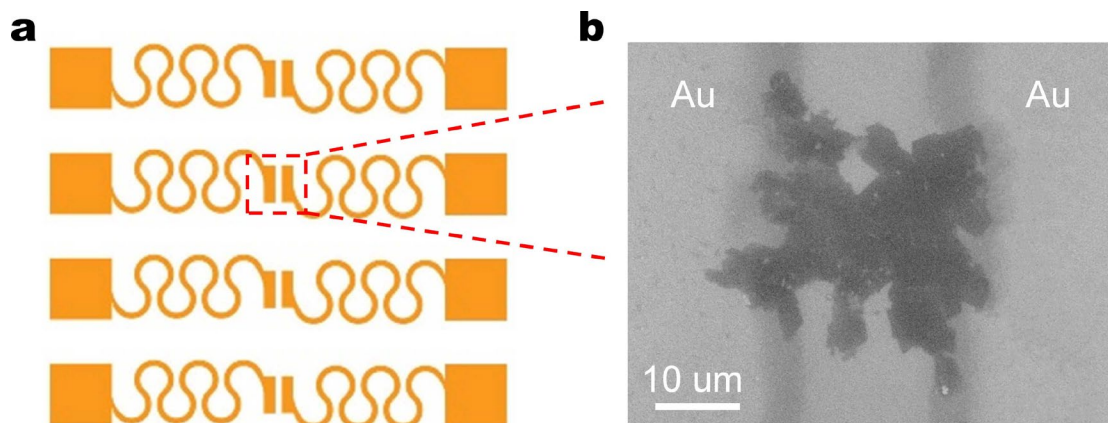
304 **Supplementary Fig. 29 | Structure characterization of bulk WS₂ after discharge**
 305 **and charge process.** EPR spectrums of bulk WS₂, L-Li_xWS₂, L-Li_xWS₂-
 306 deintercalation, S-Li_xWS₂ and S-Li_xWS₂-deintercalation. S-Li_xWS₂, L-Li_xWS₂ denote
 307 as Li⁺ intercalation of WS₂ by small and large discharge current densities, respectively.
 308 Five samples are tested in the same batch.

309 As illustrated in **Supplementary Fig. 29**, following the deintercalation of L-Li_xWS₂
 310 through the charge process under the same current, there is a substantial decrease in S
 311 vacancies, which remains slightly higher than that in bulk WS₂. This decrease in
 312 vacancies can be attributed to the extraction of a significant amount of intercalated
 313 lithium from the interlayer of WS₂. Conversely, after the deintercalation of S-Li_xWS₂,
 314 the reduction in S vacancies is minimal. This minimal decrease can be attributed to the
 315 fact that only a very small amount (0.94%) of lithium is extracted from S-Li_xWS₂. These
 316 EPR results highly aligns with the conclusions drawn from the discharge/charge curves
 317 (**Supplementary Fig. 28**).



318

319 **Supplementary Fig. 30 | Theoretical simulations of the formation of the solid**
 320 **electrolyte interface (SEI) under large and small discharge current densities. a,**
 321 **The mean square displacement (MSD) of Li^+ under different potentials. b, The MSD of**
 322 **Li^+ within the interlayer direction (y-axis) of WS_2 . c, The diffusion energy barriers of**
 323 **Li^+ in the WS_2 layers. The structure models under d large discharge current density and**
 324 **g small discharge current density simulations. The structures of WS_2 for e large**
 325 **discharge current density and h small discharge current density. The Li^+ density**
 326 **distributions in WS_2 under the f large discharge current density and i small discharge**
 327 **current density.**

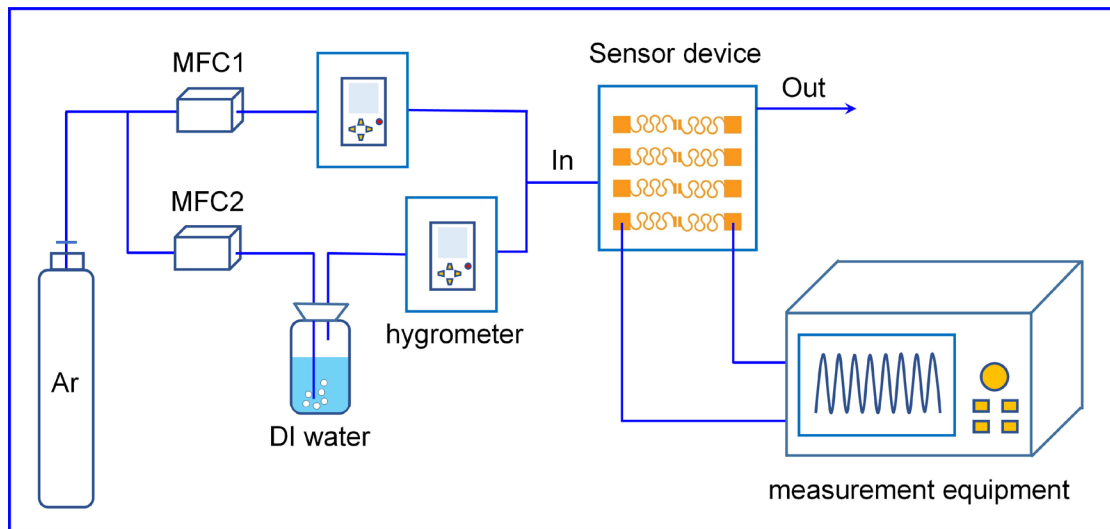


328

329 **Supplementary Fig. 31 | Morphology characterization of 2H-WS₂ NSs based**

330 **humidity sensor device. a, Schematic of the device. b, SEM image of 2H-WS₂ NSs as**

331 **the active channel for device fabrication.**

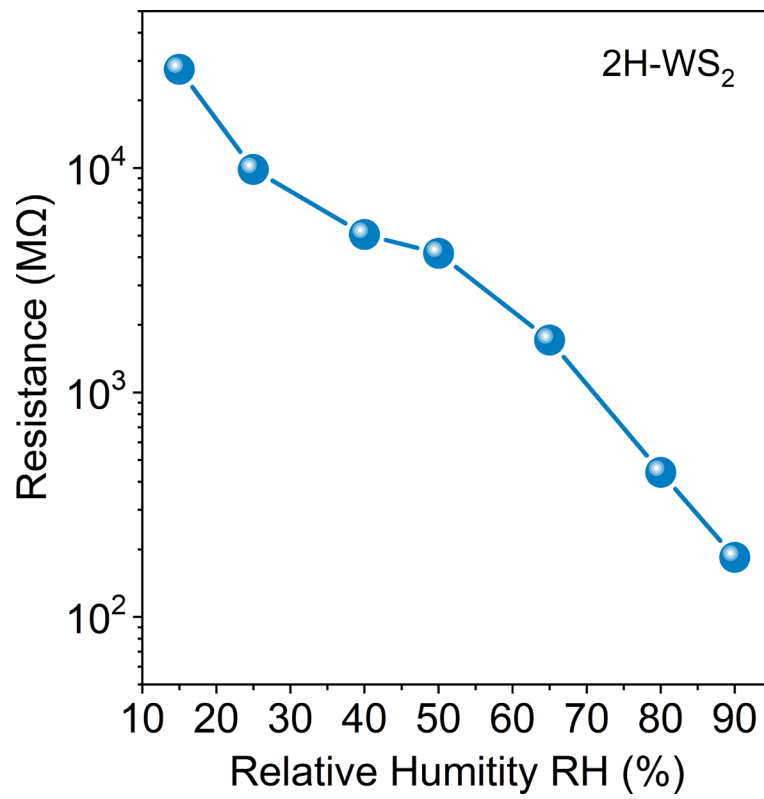


332

333 **Supplementary Fig. 32 | Schematic diagram of home-made equipment for**

334 **humidity sensing performance tests.** MFC denotes as mass flow controller. MFC1

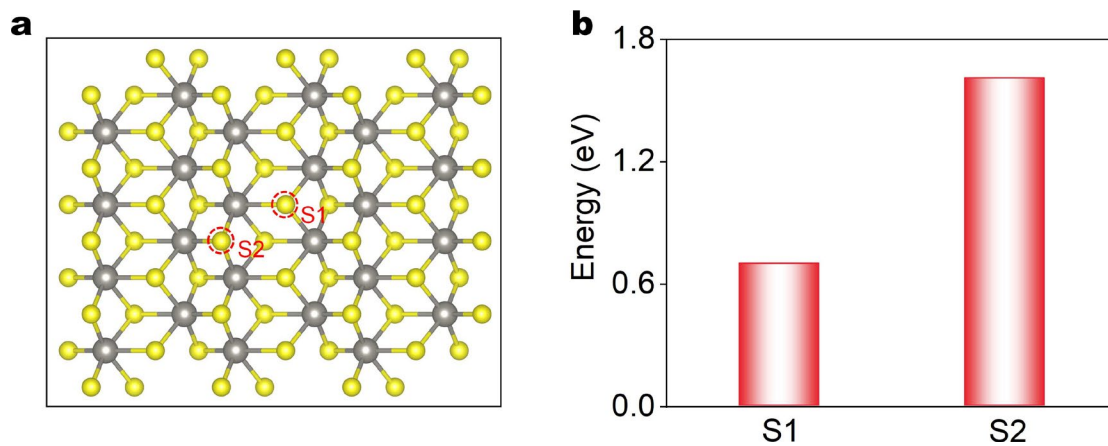
335 and MFC2 are the mass flowmeter.



336

337 **Supplementary Fig. 33 | Resistance variation of the 2H-WS₂ NSs based humid**

338 **sensor under different RH levels.**



355

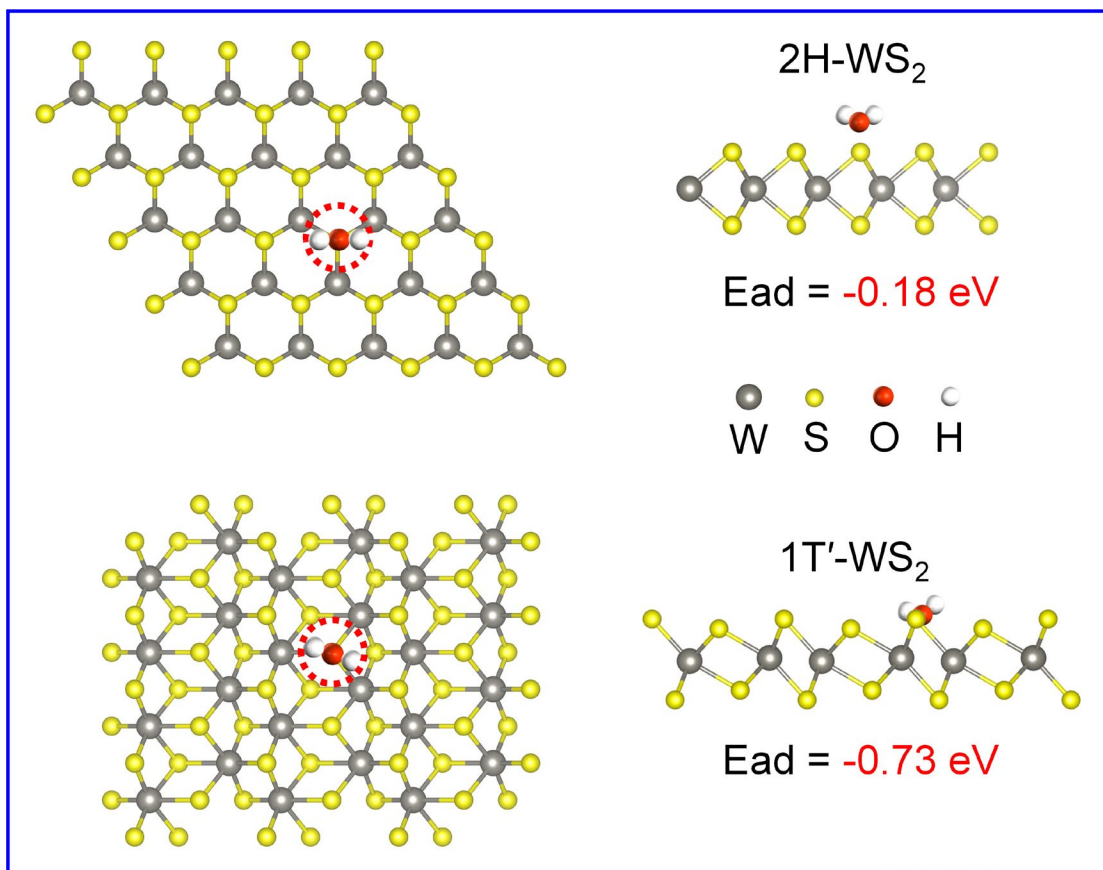
356 **Supplementary Fig. 35 | DFT calculations for sulfur vacancy in 1T'-WS₂.** **a,**

357 Schematic of the possible sulfur vacancy S1 and S2 in 1T'-WS₂. **b,** The energy that

358 need for generating S1 and S2 vacancy in **a**. Note that generation of sulfur vacancy S1

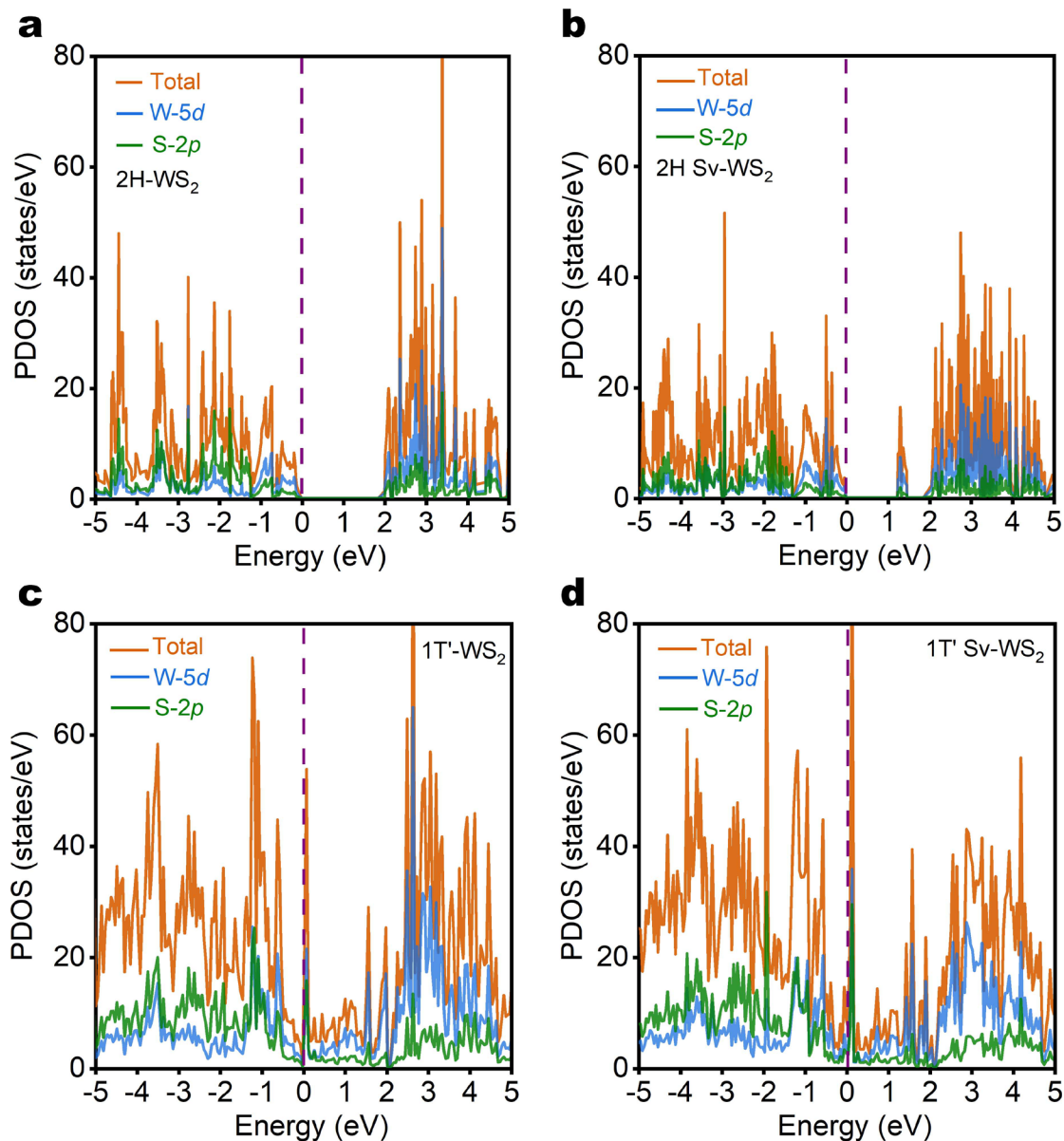
359 is more energy favorable than S2 (0.70 eV vs 1.61 eV), therefore sulfur vacancy S1 is

360 selected to do the DFT calculation for H₂O molecule adsorption on 1T'-WS₂.



361

362 **Supplementary Fig. 36 | Adsorption energy of H₂O molecule on 2H- and 1T'-WS₂.**

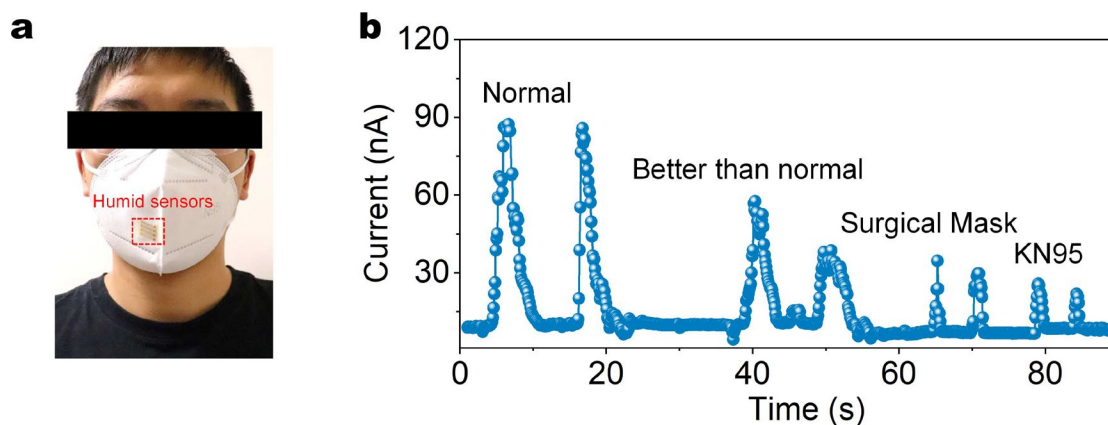


363

364 **Supplementary Fig. 37 | DFT calculation of projected density of states for the 2H-**
 365 **and 1T'-WS₂ with the sulfur vacancy (Sv).** The projected density of states for **a** 2H-
 366 WS₂ and **b** 2H Sv-WS₂, **c** 1T'-WS₂ and **d** 1T' Sv-WS₂. The red dotted line corresponds
 367 to the Fermi level.

368 To gain a deeper understanding of the variation in electronic properties of 2H- and 1T'-
 369 WS₂ caused by the presence of S vacancy, we conducted calculations of the projected
 370 density of states (PDOS) for 2H-WS₂, 2H Sv-WS₂, 1T'-WS₂ and 1T' Sv-WS₂ using
 371 density functional theory. These results are presented in **Supplementary Figure 37**.
 372 **Supplementary Fig. 37a** show the PDOS of pristine 2H-WS₂, which exhibits a wide
 373 bandgap of 1.88 eV, indicative of its semiconductor properties. It is worth mentioning

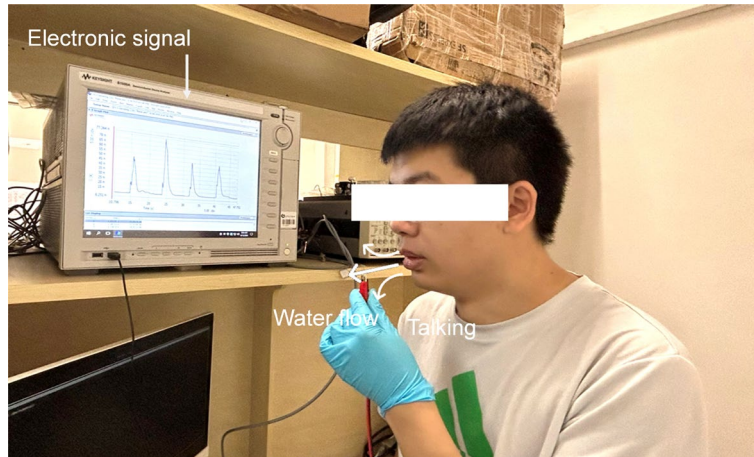
374 that this bandgap value aligns with the primitive cell calculation.⁷ In the case of 2H Sv-
375 WS₂ as shown in **Supplementary Fig. 37b**, the bandgap becomes noticeably narrower,
376 with a value of 1.24 eV after introducing a S vacancy on the WS₂ surface. This
377 narrowing is attributed to the hybridization of the 2p orbital of S atoms and the 5d
378 orbital of W atoms within the forbidden band, generating a new energy level. This shift
379 causes the bottom of the conduction band to move closer to the Fermi energy. The
380 significant reduction in the bandgap of WS₂ after introducing a S vacancy can
381 effectively promote electron transfer and enhance conductivity. For 1T'-WS₂, after the
382 introduction of a S vacancy, the generation of new orbitals around the orbital energy
383 levels, as shown in **Supplementary Fig. 37c-d**, might contribute to the adsorption of
384 H₂O onto WS₂.



385

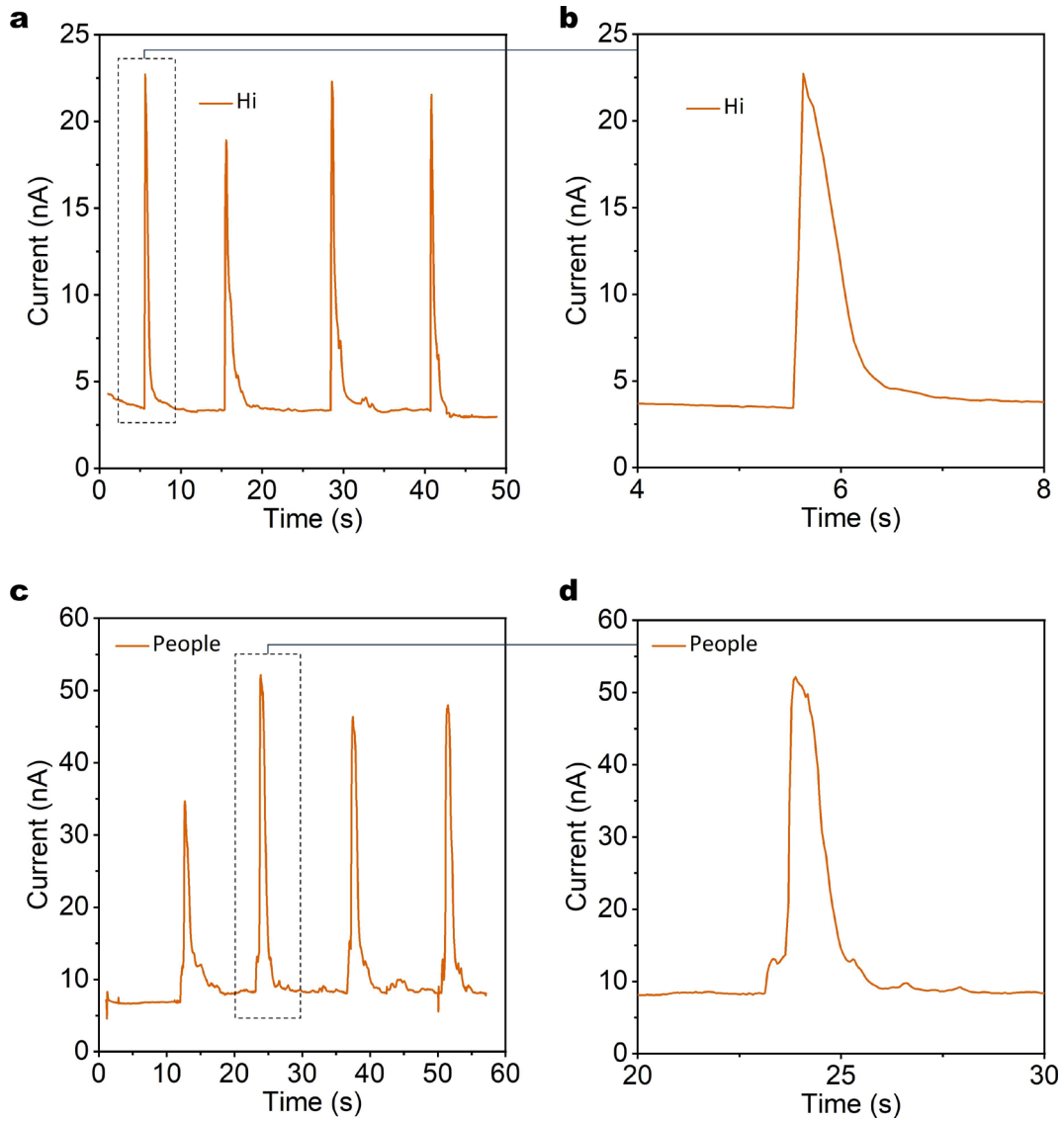
386 **Supplementary Fig. 38 | Test the protection performance of different masks via**
 387 **using 2H-WS₂ based humidity sensor.** **a**, Optical image of the 2H-WS₂ humidity
 388 sensor attached outside the mask. **b**, Dynamic humidity response and recovery
 389 measurement for different levels of masks.

390 As demonstrated in **Supplementary Fig. 38a**, the WS₂ humidity sensor was attached
 391 outside the masks to evaluate their effectiveness in protecting against moisture exhaled
 392 from the mouth under ambient conditions. To simulate a person's cough or sneeze, the
 393 subject exhaled heavily during this measurement. **Supplementary Fig. 38b** presents
 394 the dynamic current of the device in response to moisture passing through different
 395 types of masks. The normal mask without any filter layer exhibited poor protective
 396 performance, with the current response suddenly exceeding 90 nA. In contrast, the
 397 KN95 mask effectively resisted the exhaled moisture, with the current only slightly
 398 increasing to approximately 25 nA. These results highlight that our WS₂ humidity
 399 sensor can serve as a sensitive and convenient method for assessing the quality of masks.



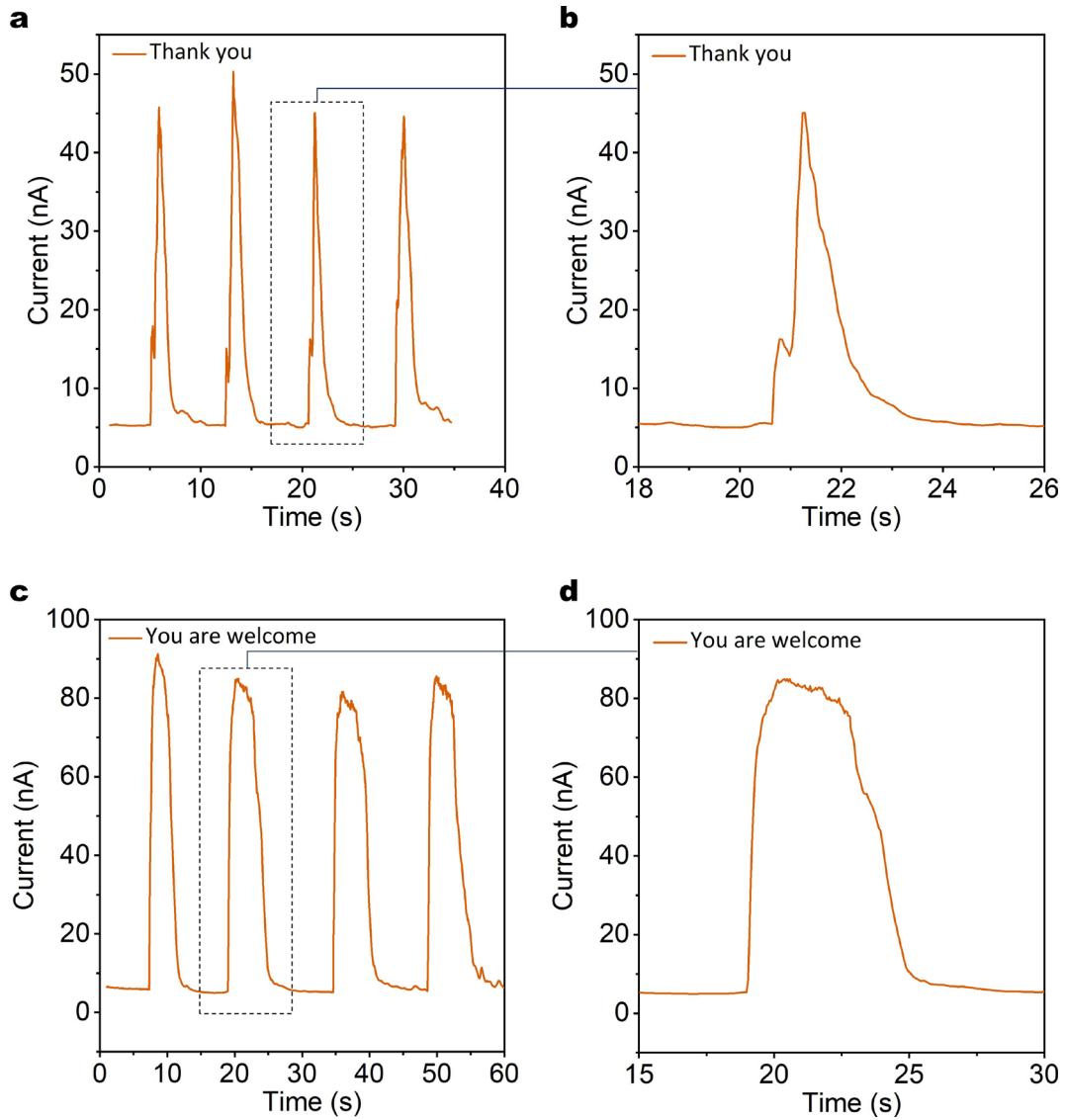
400

401 **Supplementary Fig. 39 | Photograph of humidity sensor set-up for voice**
402 **recognition.**



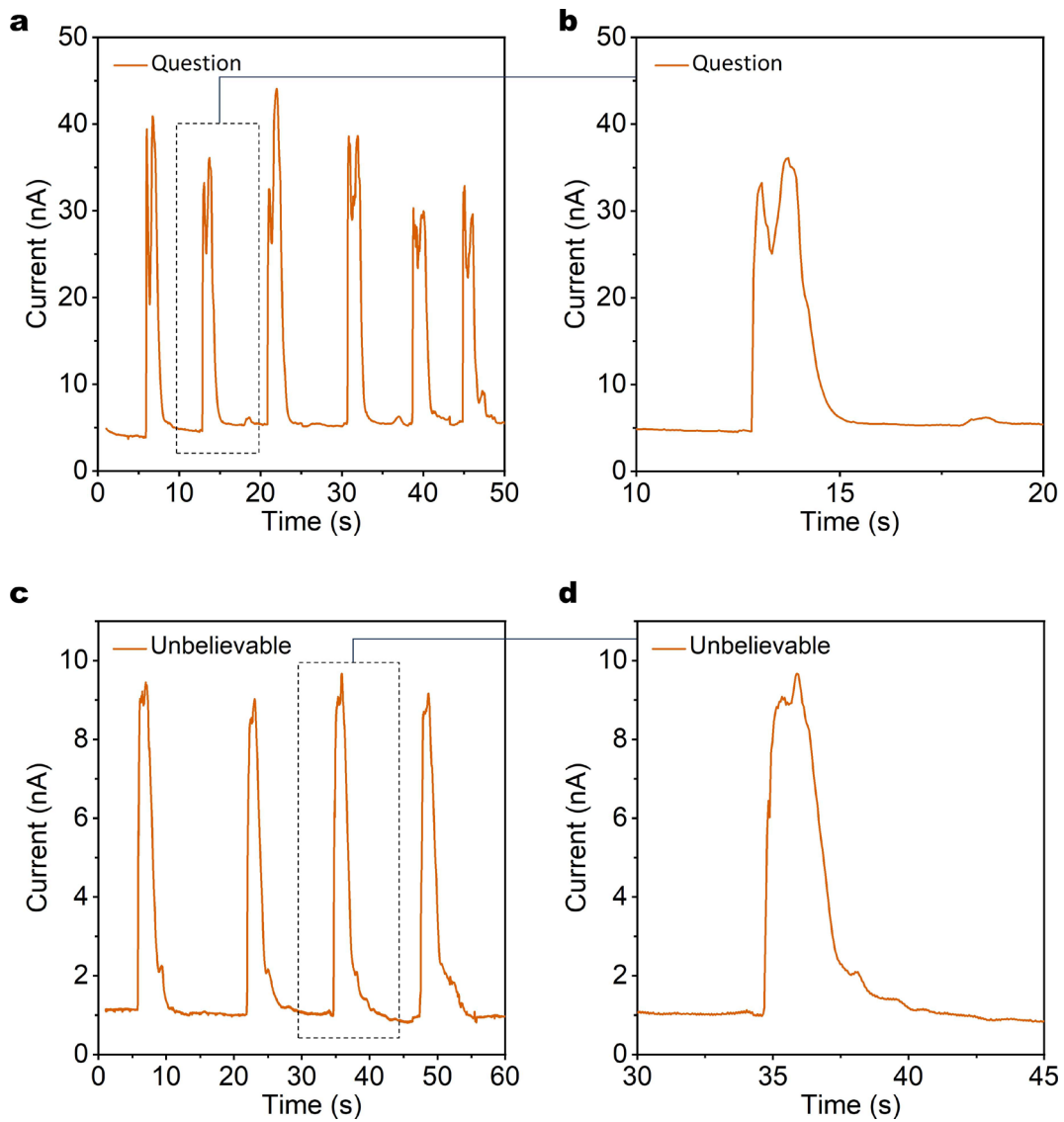
403

404 **Supplementary Fig. 40 | Voice recognition of speaking different words. a-b,**
 405 Response current of 2H-WS₂ while speaking "Hi", and the corresponding amplified
 406 curve. **c-d,** Response current of 2H-WS₂ while speaking "People", and the
 407 corresponding amplified curve.



408

409 **Supplementary Fig. 41 | Voice recognition of speaking different words. a-b,**
 410 Response current of 2H-WS₂ while speaking “Thank you”, and the corresponding
 411 amplified curve. **c-d,** Response current of 2H-WS₂ while speaking “You are welcome”,
 412 and the corresponding amplified curve.



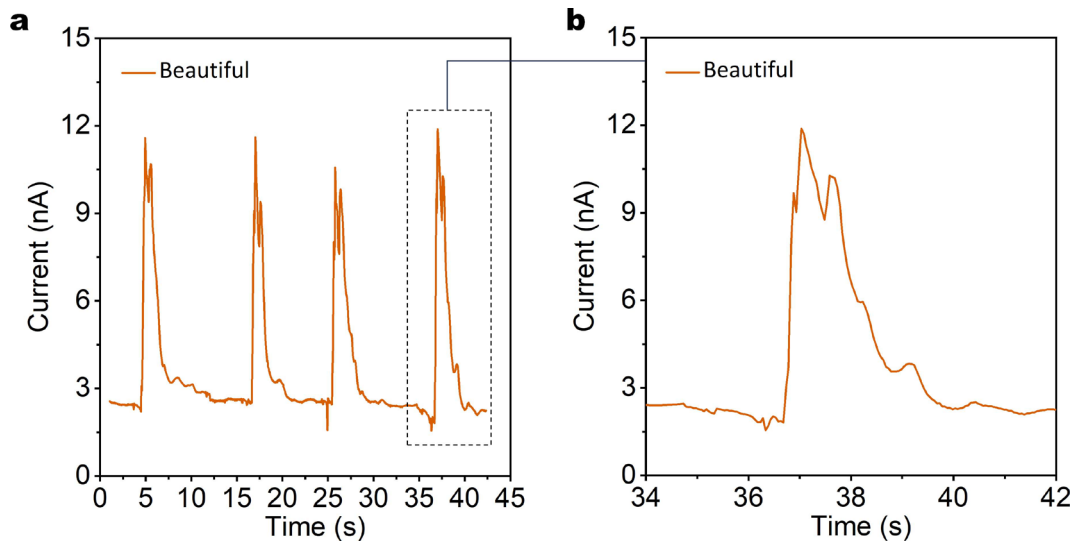
413

414 **Supplementary Fig. 42 | Voice recognition of speaking different words. a-b,**

415 Response current of 2H-WS₂ while speaking “Question”, and the corresponding

416 amplified curve. **c-d,** Response current of 2H-WS₂ while speaking “Unbelievable”, and

417 the corresponding amplified curve.

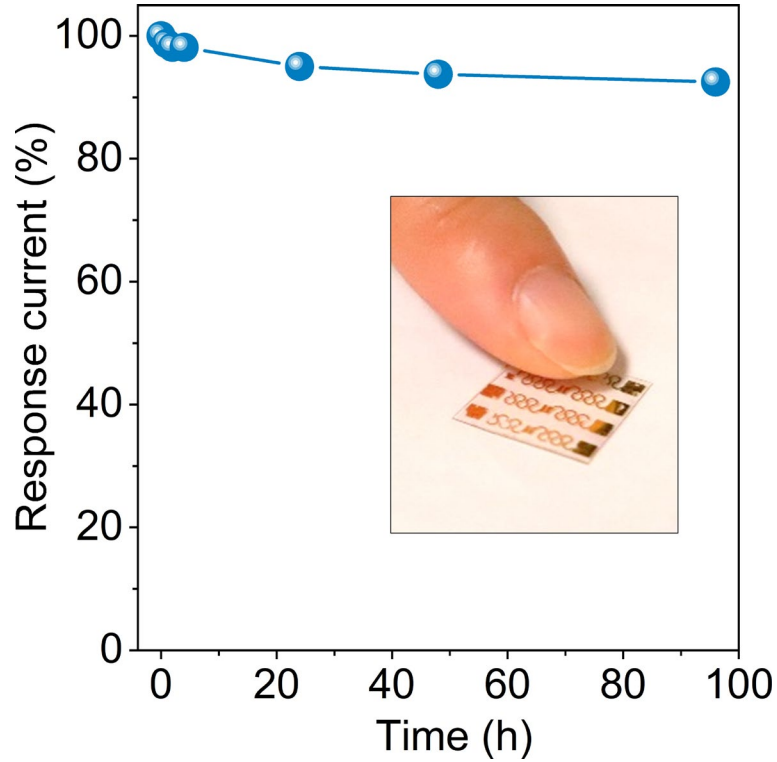


418

419 **Supplementary Fig. 43 | Voice recognition of speaking different words. a-b,**

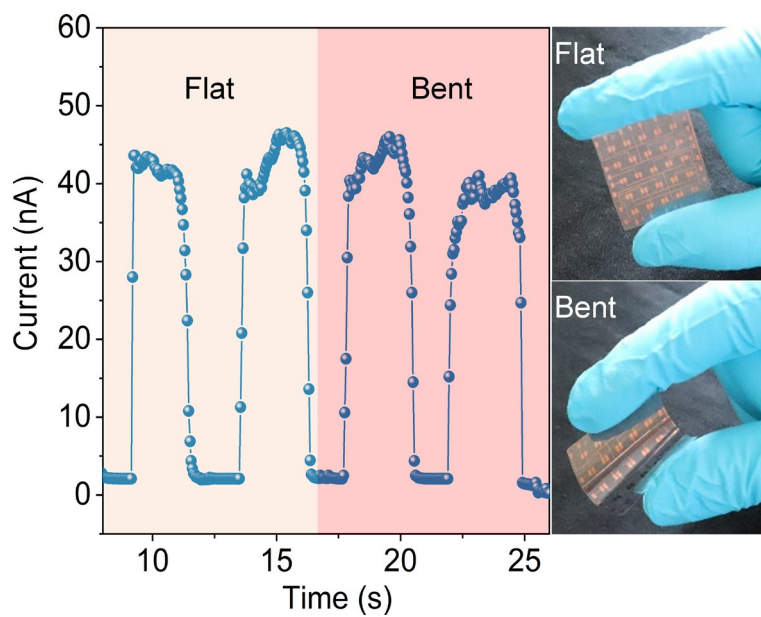
420 Response current of 2H-WS₂ while speaking "Beautiful", and the corresponding

421 amplified curve.



422

423 **Supplementary Fig. 44 | The performance stability of 2H-WS₂ based humidity**
424 **sensor device.** Long-term stability test of the humidity sensor after exposing to the
425 indoor environment (65% RH, R.T.) for different times. Inset photo shows the distance
426 between the finger with device is 3 mm. Even after exposing for 96 h, the response
427 current still maintains 93% of its original value, demonstrating its superior stability in
428 indoor environment.



429

430 **Supplementary Fig. 45 | The flexibility of 2H-WS₂ based sensor device.** Dynamic
 431 humidity response and recovery measurement of the 2H-WS₂ humidity sensor array
 432 under flat and bending condition. The bend state of the device doesn't affect the sensing
 433 properties of 2H-WS₂.

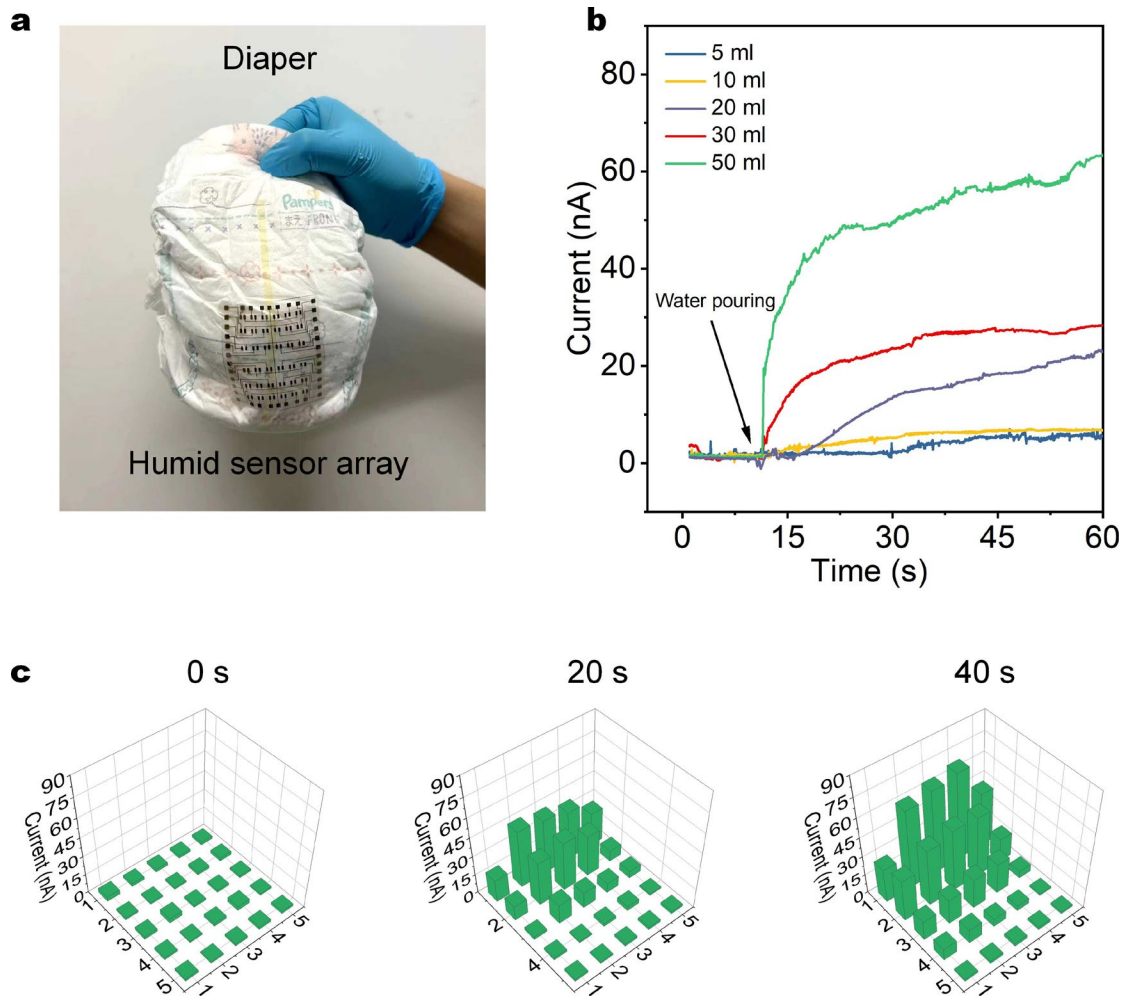


434

435 **Supplementary Fig. 46 | Raw data for current distribution of humidity sensor**

436 **array.** Original current distribution of 5×5 humid sensor array in none-contact finger

437 localization experiments.



438

439 **Supplementary Fig. 47 | Humidity sensor array for monitoring baby diaper**
 440 **wetness.** **a**, Photograph of a baby diaper with humidity sensor array. **b**, Response
 441 current of humidity sensor array with pouring different volume of water. **c**, Current
 442 distribution of humid sensor array at different time intervals after pouring the water.

443 To highlight the reconfigurability and advantages of our humidity sensor array, we
 444 showcase its potential application in monitoring baby diaper wetness. Prolonged
 445 exposure to a wet diaper can lead to discomfort and potential health issues such as
 446 diaper rash or urinary tract infections. Caregivers may occasionally overlook or lack
 447 the time to manually check their baby's diaper status throughout the day. Leveraging
 448 the high sensitivity and spatial humidity resolution of our humidity sensor array, it can
 449 effectively monitor diaper moisture levels. When a baby urinates, the diaper promptly
 450 absorbs the urine into its absorbent core, causing a change in the relative humidity on
 451 the diaper's surface. By utilizing the humidity sensor array to detect these humidity

452 changes, we can ascertain whether the baby has urinated.

453 As shown in **Supplementary Fig. 47a**, the softness of the humidity sensor array enables
454 direct and secure attachment to the outside of the baby's diaper. To test the single
455 humidity sensor response behavior, we poured different volumes of water into the
456 diaper (**Supplementary Fig. 47b**). When pouring 5ml or 10ml of water, due to the
457 limited water permeation caused by the diaper's inherent absorbent capacity, the device
458 exhibits only a weak humidity response. Upon pouring 20ml of water, there is a
459 noticeable change in the surface humidity of the diaper, resulting in a significant
460 increase in device current, albeit not immediately after pouring. However, pouring more
461 than 30ml of water leads to an immediate and pronounced detection of humidity change
462 by the device, accompanied by a clear increase in current, indicating the accumulation
463 of a significant amount of moisture inside the diaper. This demonstrates the feasibility
464 of individual devices for monitoring diaper wetness.

465 Furthermore, we measured the array current distribution at different time intervals (0s,
466 20s, 40s) after pouring 50ml of water. As shown in **Supplementary Fig. 47c**, as water
467 permeates and spreads, the humidity sensor array can detect humidity gradients across
468 large surface areas ($\sim 5 \times 5 \text{ cm}^2$, enough to cover the core position) of the diaper, which
469 are reflected in changes in the array current distribution. Higher sensor currents
470 represent higher surface humidity. This can eliminate erroneous judgments caused by
471 measurement errors resulting from the varying positions of individual devices. This
472 data also provide potential aids in establishing the alarm threshold within the
473 operational circuit system.

474 **Supplementary Table 1 | DFT calculated phase formation energy and**
 475 **corresponding interlayer spacing for lithium intercalation of WS₂.**

Li x	2H Li _x WS ₂		1T' Li _x WS ₂	
	interlayer spacing	Formation energy	interlayer spacing	Formation energy
	(Å)	(eV)	(Å)	(eV)
0	6.214	-2.549	6.034	-2.011
0.0625	6.281	-2.574	6.116	-2.140
0.125	6.361	-2.597	6.217	-2.270
0.1875	6.411	-2.619	6.244	-2.409
0.25	6.506	-2.649	6.303	-2.536
0.3125	6.546	-2.666	6.362	-2.655
0.375	6.592	-2.717	6.350	-2.771
0.4375	6.677	-2.771	6.389	-2.912
0.5	6.645	-2.769	6.405	-3.011
0.5625	6.653	-2.840	6.456	-3.107
0.625	6.704	-2.862	6.396	-3.202
0.6875	6.696	-2.888	6.386	-3.307
0.75	6.647	-2.937	6.379	-3.381
0.8125	6.635	-2.964	6.327	-3.459
0.875	6.598	-3.010	6.323	-3.526
0.9375	6.616	-3.034	6.308	-3.597
1	6.614	-3.062	6.339	-3.609

476

477 **Supplementary Table 2 | Comparison of humidity sensing performance of the**
 478 **developed 2H and 1T' WS₂ NSs with other reported humidity sensors.**

Materials	Response time (s)	Recover time (s)	Reference
VS ₂	35	31	<i>Adv. Mater.</i> 24 , 1969-1974 (2012) ⁸
2H MoS ₂	10	60	<i>Adv. Mater.</i> 29 , 1702076 (2017) ⁹
2H MoS ₂	300	600	<i>ACS Nano</i> 7 , 4879-4891 (2013) ¹⁰
Graphene/Silk	3	6	<i>Adv. Funct. Mater.</i> 29 , 1808695 (2019) ¹¹
Graphene Oxide	1.4	10	<i>Adv. Mater.</i> 27 , 1370-1375 (2015) ¹²
Graphene Fiber	180	125	<i>Small</i> 14 , 1703934 (2018) ¹³
Paper	600	1500	<i>Angew. Chem. Int. Ed.</i> 55 , 5727-5732 (2016) ¹⁴
MXene	1	201	<i>ACS Sens.</i> 4 , 1261-1269 (2019) ¹⁵
MXene/Ag	5	80	<i>Adv. Funct. Mater.</i> 29 , 1905197 (2019). ¹⁶
MXene	1000	2000	<i>Adv. Mater.</i> 33 , 2104878 (2021) ¹⁷
Graphene	40	20	<i>Adv. Mater.</i> 33 , 2100218 (2021) ¹⁸
PEDOT:PSS	1	4	<i>Sci. Adv.</i> 6 , eaba0931 (2020) ¹⁹
Graphene Oxide	170	190	<i>Adv. Mater.</i> 28 , 2601-2608 (2016). ²⁰
Al/PI	1.5	50.6	<i>Nat. Commun.</i> 9 , 244 (2018) ²¹
Perovskite	5	5	<i>Adv. Funct. Mater.</i> 30 , 1907449 (2020) ²²
Cleancool/Cu fiber	3.5	4	<i>Adv. Funct. Mater.</i> 29 , 1904549 (2019) ²³
Graphene Oxide	4.5	5.5	<i>Adv. Mater.</i> 28 , 3549-3556 (2016) ²⁴
TiO ₂	45	200	<i>Adv. Mater.</i> 30 , 1705925 (2018) ²⁵
SnS ₂ /rGO	6	15	<i>Nano Energy</i> 67 , 104251 (2020) ²⁶
MXene/Cellulose	20	70	<i>ACS Nano</i> 15 , 16811-16818 (2021) ²⁷
GO/SF	1.05	0.8	<i>Nat. Commun.</i> 13 , 5416 (2022) ²⁸
1T'-WS₂	0.30	1.20	This work
2H-WS₂	0.48	0.32	This work

479

480 **Supplementary References**

- 481 1 Lin, Z. Y. *et al.* Solution-processable 2D semiconductors for high-performance
482 large-area electronics. *Nature* **562**, 254-258, doi:10.1038/s41586-018-0574-4
483 (2018).
- 484 2 Leng, K. *et al.* Phase Restructuring in Transition Metal Dichalcogenides for
485 Highly Stable Energy Storage. *ACS Nano* **10**, 9208-9215,
486 doi:10.1021/acsnano.6b05746 (2016).
- 487 3 Zhu, K. X. *et al.* Solution-Phase Synthesis of Vanadium Intercalated 1T'-WS₂
488 with Tunable Electronic Properties. *Nano Lett.* **23**, 4471-4478,
489 doi:10.1021/acs.nanolett.3c00826 (2023).
- 490 4 Fan, X. B. *et al.* Controlled Exfoliation of MoS₂ Crystals into Trilayer
491 Nanosheets. *J. Am. Chem. Soc.* **138**, 5143-5149, doi:10.1021/jacs.6b01502
492 (2016).
- 493 5 Wang, Y. *et al.* Structural phase transition in monolayer MoTe₂ driven by
494 electrostatic doping. *Nature* **550**, 487-491, doi:10.1038/nature24043 (2017).
- 495 6 Li, Y. *et al.* Structural semiconductor-to-semimetal phase transition in two-
496 dimensional materials induced by electrostatic gating. *Nat. Commun.* **7**, 10671,
497 doi:10.1038/ncomms10671 (2016).
- 498 7 Wang, Q. H. *et al.* Electronics and optoelectronics of two-dimensional transition
499 metal dichalcogenides. *Nat. Nanotechnol.* **7**, 699-712,
500 doi:10.1038/nnano.2012.193 (2012).
- 501 8 Feng, J. *et al.* Giant Moisture Responsiveness of VS₂ Ultrathin Nanosheets for
502 Novel Touchless Positioning Interface. *Adv. Mater.* **24**, 1969-1974,
503 doi:10.1002/adma.201104681 (2012).
- 504 9 Zhao, J. *et al.* Highly Sensitive MoS₂ Humidity Sensors Array for Noncontact
505 Sensation. *Adv. Mater.* **29**, 1702076. doi:10.1002/adma.201702076 (2017).
- 506 10 Late, D. J. *et al.* Sensing Behavior of Atomically Thin-Layered MoS₂
507 Transistors. *ACS Nano* **7**, 4879-4891, doi:10.1021/nn400026u (2013).
- 508 11 Wang, Q. *et al.* Self-Healable Multifunctional Electronic Tattoos Based on Silk

509 and Graphene. *Adv. Funct. Mater.* **29**, 1808695, doi:10.1002/adfm.201808695
510 (2019).

511 12 Wang, X. W. *et al.* Exfoliation at the Liquid/Air Interface to Assemble Reduced
512 Graphene Oxide Ultrathin Films for a Flexible Noncontact Sensing Device. *Adv.*
513 *Mater.* **27**, 1370-1375, doi:10.1002/adma.201404069 (2015).

514 13 Choi, S. J. *et al.* Nitrogen-Doped Single Graphene Fiber with Platinum Water
515 Dissociation Catalyst for Wearable Humidity Sensor. *Small* **14**, 1703934,
516 doi:10.1002/sml.201703934 (2018).

517 14 Guder, F. *et al.* Paper-Based Electrical Respiration Sensor. *Angew. Chem. Int.*
518 *Ed.* **55**, 5727-5732, doi:10.1002/anie.201511805 (2016).

519 15 Yang, Z. J. *et al.* Improvement of Gas and Humidity Sensing Properties of
520 Organ-like MXene by Alkaline Treatment. *ACS Sens.* **4**, 1261-1269,
521 doi:10.1021/acssensors.9b00127 (2019).

522 16 Liu, L. X. *et al.* Flexible and Multifunctional Silk Textiles with Biomimetic
523 Leaf-Like MXene/Silver Nanowire Nanostructures for Electromagnetic
524 Interference Shielding, Humidity Monitoring, and Self-Derived Hydrophobicity.
525 *Adv. Funct. Mater.* **29**, 1905197, doi:10.1002/adfm.201905197 (2019).

526 17 Pazniak, H. *et al.* 2D Molybdenum Carbide MXenes for Enhanced Selective
527 Detection of Humidity in Air. *Adv. Mater.* **33**, 2104878,
528 doi:10.1002/adma.202104878 (2021).

529 18 Lu, L. J. *et al.* Flexible Noncontact Sensing for Human-Machine Interaction.
530 *Adv. Mater.* **33**, 2100218, doi:10.1002/adma.202100218 (2021).

531 19 Wang, W. Y. *et al.* Inflight fiber printing toward array and 3D optoelectronic and
532 sensing architectures. *Sci. Adv.* **6**, eaba0931, doi:10.1126/sciadv.aba0931 (2020).

533 20 Ho, D. H. *et al.* Stretchable and Multimodal All Graphene Electronic Skin. *Adv.*
534 *Mater.* **28**, 2601-2608, doi:10.1002/adma.201505739 (2016).

535 21 Hua, Q. L. *et al.* Skin-inspired highly stretchable and conformable matrix
536 networks for multifunctional sensing. *Nat. Commun.* **9**, 244,
537 doi:10.1038/s41467-017-02685-9 (2018).

- 538 22 Cho, M. Y. *et al.* Perovskite-Induced Ultrasensitive and Highly Stable Humidity
539 Sensor Systems Prepared by Aerosol Deposition at Room Temperature. *Adv.*
540 *Funct. Mater.* **30**, 1907449, doi:10.1002/adfm.201907449 (2020).
- 541 23 Ma, L. Y. *et al.* Full-Textile Wireless Flexible Humidity Sensor for Human
542 Physiological Monitoring. *Adv. Funct. Mater.* **29**, 1904549,
543 doi:10.1002/adfm.201904549 (2019).
- 544 24 Hu, K. S. *et al.* Self-Powered Electronic Skin with Biotactile Selectivity. *Adv.*
545 *Mater.* **28**, 3549-3556, doi:10.1002/adma.201506187 (2016).
- 546 25 Shen, D. Z. *et al.* Self-Powered Wearable Electronics Based on Moisture
547 Enabled Electricity Generation. *Adv. Mater.* **30**, 1705925,
548 doi:10.1002/adma.201705925 (2018).
- 549 26 Zhang, D. Z. *et al.* High-performance flexible self-powered tin disulfide
550 nanoflowers/reduced graphene oxide nanohybrid-based humidity sensor driven
551 by triboelectric nanogenerator. *Nano Energy* **67**, 104251,
552 doi:10.1016/j.nanoen.2019.104251 (2020).
- 553 27 Li, P. D. *et al.* A $Ti_3C_2T_x$ MXene-Based Energy-Harvesting Soft Actuator with
554 Self-Powered Humidity Sensing and Real-Time Motion Tracking Capability.
555 *ACS Nano* **15**, 16811-16818, doi:10.1021/acsnano.1c07186 (2021).
- 556 28 Li, S. *et al.* Humidity-sensitive chemoelectric flexible sensors based on metalair
557 redox reaction for health management. *Nat. Commun.* **13**, 5416,
558 doi:10.1038/s41467-022-33133-y (2022).
- 559